

Active Helicopter Rotor Control Using Blade-Mounted Actuators

by

James Christopher Garcia

B.S.M.E. Virginia Polytechnic Institute and State University (1991)

Submitted to the Department of Mechanical Engineering
in partial fulfillment of the requirements
for the degree of

Master of Science

at the

Massachusetts Institute of Technology

February 1994

© Massachusetts Institute of Technology 1994. All rights reserved.

Author _____

Department of Mechanical Engineering

December 8, 1993

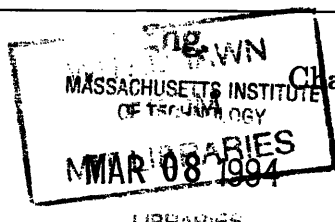
Certified by _____

Professor Steven R. Hall
Department of Aeronautics and Astronautics
Thesis Supervisor

Accepted by _____

Professor Ain A. Sonin

Chairman, Departmental Graduate Committee



LIBRARIES

Active Helicopter Rotor Control Using Blade-Mounted Actuators

by

James Christopher Garcia

Submitted to the Department of Mechanical Engineering
on December 8, 1993, in partial fulfillment of the
requirements for the degree of
Master of Science

Abstract

An aeroelastic model of a smart rotor system (which incorporates blade-mounted trailing-edge flap actuators and conventional root pitch actuation) is presented in linear time invariant state space form. The servo-flap deflections are modeled as producing incremental lift and moment variations, so that any linear aerodynamic actuator can be evaluated. This smart rotor model is used to conduct parametric studies involving rotor blade torsional stiffness, center-of-gravity offset, additional actuator mass, and actuator placement. Results on the effects of collective root pitch and servo-flap actuation on rotor thrust response are presented. Active rotor vibration reduction is demonstrated by applying higher harmonic control algorithms to the state space rotor model. Using reasonable servo-flap deflections, a rotor equipped with trailing-edge flaps can provide enough authority to cancel higher harmonic vibration.

Thesis Supervisor: Steven R. Hall, Sc.D.
Title: Associate Professor of Aeronautics and Astronautics

Acknowledgements

I would like to thank my advisor, Professor Steven Hall, for his guidance and support. I also wish to thank Mr. Frank Tarzanin and Ms. Joyce Peranteau of Boeing Helicopters for supporting the C60 rotor analysis program used in this research. In addition, I want to thank my office mates, Matthew Fox, Paul van Deventer, Eric Prechtl, and Kyle Yang for their friendship, advice, and endless coffee breaks. Lastly, I'd like to thank my parents for their love and support.

This material is based on work supported by a National Science Foundation Graduate Research Fellowship. Additional financial support was provided by Boeing Helicopters under Contract Nos. ABQ024, ACP853, and ADM651.

Contents

1	Introduction	19
1.1	Conventional Helicopter Rotor Control	19
1.2	Alternative Rotor Control Methods	23
1.2.1	Circulation Control	23
1.2.2	Mechanical Servo-Flaps	25
1.2.3	Piezoelectric Actuation	27
1.3	Thesis Objective and Overview	30
2	State Space Rotor Model	33
2.1	Rotor Coordinates	33
2.2	Multi-Blade Coordinates	35
2.3	<i>In Vacuo</i> Blade Dynamics	41
2.3.1	Torsional Modal Analysis	41
2.3.2	<i>In Vacuo</i> Equations of Motion	44
2.4	Aerodynamic Model	49
2.5	Inflow Dynamics	55
2.6	Hub Reactions	56
2.7	State Space Model	59
3	State Space Model Results	65
3.1	Model validation using C60	67
3.2	Parametric Studies	70
3.2.1	Torsional Stiffness Study	71

3.2.2	C.G. Offset and Additional Mass Study	74
3.2.3	Actuator Placement Study	79
3.2.4	Aileron Reversal Study	81
4	Servo-Flap Actuation for Higher Harmonic Control	89
4.1	Higher Harmonic Control Loads	90
4.2	HHC Algorithms	92
4.3	Implementing HHC	94
4.4	Multivariable HHC	100
5	Conclusions	107
5.1	Summary of Parametric Studies	107
5.2	Feasibility of Servo-flap Actuation for HHC	108
5.3	Further Research	109
A	Rotor Blade Integrals	111
A.1	Aerodynamic Integrals	111
A.2	Structural Integrals	112
B	Matrices for Rotor Dynamics	113
B.1	Structural Dynamics, Δ and Ψ Matrices	113
B.2	Aerodynamics, Λ Matrices	115
B.3	Hub Reactions, Γ and Φ Matrices	116
B.4	Coupled Dynamics Matrices	118
C	Inflow Dynamics	119
D	Listing of Matlab Code	123
References		163

List of Figures

2-1	Block diagram of coupled rotor and inflow dynamics. Adapted from Pitt and Peters [35].	34
2-2	Helicopter rotor coordinates.	35
2-3	Sectional rotor blade coordinates.	36
2-4	MBC transformation from rigid flapping angle to rotor disk modes. .	38
2-5	Lumped torsional approximation of rotor blade.	43
2-6	Velocity components of differential chordwise element of mass: (a) sectional view and (b) top view.	46
2-7	Non-dimensional velocity components: (a) sectional view, (b) top view.	51
3-1	Continuous frequency response from state space model and C60 validation points at $\bar{\omega} = 0, 4$, and 8 . Rigid flapping only case.	67
3-2	Continuous frequency response from state space model and C60 validation points at $\bar{\omega} = 0, 4$, and 8 . Elastic torsion only case.	68
3-3	Continuous frequency response from state space model and C60 validation points at $\bar{\omega} = 0, 4$, and 8 . Rigid flapping and elastic torsion coupled by c.g. offset.	69
3-4	The effect of blade torsional stiffness on $G_{\theta,0}(j\bar{\omega})$ for H-34 rotor in hover.	72
3-5	The effect of blade torsional stiffness on $G_{\eta,0}(j\bar{\omega})$ for H-34 rotor in hover.	73
3-6	The effect of blade torsional stiffness on thrust $G_{\theta,0}(j\bar{\omega})$ for H-34 rotor in edgewise flight ($\mu = .25$).	74
3-7	The effect of blade torsional stiffness on $G_{\eta,0}(j\bar{\omega})$ for H-34 rotor in edgewise flight ($\mu = 0.25$).	75

3-8	The effect of c.g. offset on $G_{\theta_{r0}}(j\bar{\omega})$ for H-34 rotor in hover. Note that $\bar{x}_{cg} = 0.2$ case is unstable.	76
3-9	The effect of c.g. offset on $G_{\eta_0}(j\bar{\omega})$ for H-34 rotor in hover. Note that $\bar{x}_{cg} = 0.2$ case is unstable.	77
3-10	The effect of c.g. offset on $G_{\theta_{r0}}(j\bar{\omega})$ of H-34 rotor in edgewise flight ($\mu = 0.25$). Note that $\bar{x}_{cg} = 0.2$ case is unstable.	78
3-11	The effect of c.g. offset $G_{\eta_0}(j\bar{\omega})$ for H-34 rotor in edgewise flight ($\mu = 0.25$). Note that $\bar{x}_{cg} = 0.2$ case is unstable.	79
3-12	The effect of additional actuator mass on $G_{\theta_{r0}}(j\bar{\omega})$ for H-34 rotor. . .	80
3-13	The effect of additional actuator mass on $G_{\eta_0}(j\bar{\omega})$ for H-34 rotor in hover.	81
3-14	The effect of actuator placement on $G_{\eta_0}(j\bar{\omega})$ for H-34 rotor in hover..	82
3-15	The effect of actuator placement on $G_{\eta_0}(j\bar{\omega})$ for H-34 rotor in edgewise flight ($\mu = 0.25$).	83
3-16	Aileron reversal study for the H-34 rotor in hover. Based on state space model analysis.	84
3-17	Aileron reversal curves for typical rotor parameters and the H-34 rotor in hover. Based on simplified analysis.	87
4-1	HHC loop and sensitivity transfer functions: root pitch actuation. . .	96
4-2	HHC loop and sensitivity transfer functions: servo-flap actuation. . .	97
4-3	Nichols plot of HHC loop transfer function: root pitch actuation. . . .	98
4-4	Nichols plot of HHC loop transfer function: servo-flap actuation. . . .	99
4-5	Open- and closed-loop poles for various $G_{\theta_{r0}}(\bar{s})$ HHC systems: o = open-loop pole, * = closed-loop pole.	100
4-6	Open- and closed-loop poles for various $G_{\eta_0}(\bar{s})$ HHC systems: o = open-loop pole, * = closed-loop pole.	101
4-7	Block diagram of LQR/FSCF closed loop system.	104
4-8	Singular value plot of sensitivity transfer function matrix. LQR/FSCF compensator applied to H-34 rotor plant in moderate forward flight. .	105

List of Tables

2.1	State space equation for rotor system dynamics.	62
2.2	State space equation for the hub loads.	63
3.1	Baseline parameters of generic and H-34 rotors.	66
3.2	Typical rotor parameters.	86
4.1	Thrust response data for H-34 rotor at 4Ω	91
4.2	Required non-dimensional control loads for H-34 rotor at 4Ω	92

Notation

An attempt was made to use notation as consistent as possible with that of Johnson [19] and of Fox [12]. Dimensionless quantities are normalized by the rotor radius R , the rotation rate Ω , and/or the air density ρ , where possible.

a	blade section lift-curve slope c_{l_a}
A	rotor area, πR^2
\mathbf{A}	state matrix
A^n	rotor integral, see Appendix A
\mathbf{B}	state control matrix
B^n	rotor integral, see Appendix A
c	blade chord
\bar{c}	normalized blade chord, c/R
\mathbf{C}	output matrix
C_L	roll moment coefficient, $M_x/\rho AR(\Omega R)^2$
C_M	pitch moment coefficient, $M_y/\rho AR(\Omega R)^2$
C_T	thrust coefficient, $T/\rho A(\Omega R)^2$
C_T/σ	blade loading
C_k^n	rotor integral, see Appendix A
\mathbf{D}	output control matrix
D^n	rotor integral, see Appendix A
e	flap hinge offset
E^n	rotor integral, see Appendix A
\mathbf{F}	optimal feedback gain matrix
F_r	section radial aerodynamic force
F_x	section aerodynamic force parallel to disk plane
F_z	section aerodynamic force normal to disk plane
F^n	rotor integral, see Appendix A
$G(s)$	plant transfer function
GJ	torsional stiffness
G_k^n	rotor integral, see Appendix A
$H(s)$	compensator transfer function
H_k^n	rotor integral, see Appendix A
\mathbf{I}	identity matrix
I_b	characteristic inertia of the rotor blade, $\int_e^R mr^2 dr$

I_β	blade moment of inertia about the flapping hinge, $\int_e^R m \xi_\beta^2(r) dr$
I_β^*	normalized flapping inertia, I_β/I_b
I_θ	sectional pitch inertia of blade
I_{θ_k}	pitch inertia of k th torsion mode
$I_{\theta_k}^*$	normalized pitch inertia of k th torsion mode, I_{θ_k}/I_b
J^*	optimal cost
J^n	rotor integral, see Appendix A
K_β	flapping hinge spring constant
K_{θ_k}	generalized stiffness of k th torsion mode
K^n	rotor integral, see Appendix A
\mathcal{K}	stiffness matrix for lumped torsional system
L	Lagrangian
L^n	rotor integral, see Appendix A
m	blade sectional mass
M_F	flapping moment of blade, positive upward
\bar{M}_F	normalized flapping moment, $M_F/I_b\Omega^2$
M_x	rotor hub roll moment, positive toward retreating blade
M_y	rotor hub pitch moment, positive rearward
M_k^n	rotor integral, see Appendix A
\mathcal{M}	mass matrix for lumped torsional system
n	lift coefficient of servoflap c_{l_n}
\bar{n}	normalized lift coefficient of servoflap, c_{l_n}/a
N	number of blades
N	blade torsion
\bar{N}	normalized blade torsion $N/I_b\Omega^2$
N_{aero}	blade torsion due to aerodynamics
N_k	blade torsion of the k th mode
p	moment coefficient of servoflap, c_{m_n}
\bar{p}	normalized moment coefficient of servoflap, c_{m_n}/a
q	blade index
\mathbf{Q}	state weighting matrix
r	rotor disk radial coordinate
\bar{r}	normalized radial coordinate, r/R
r_1	inboard servoflap location

r_2	outboard servoflap location
r_c	root cutout
R	rotor radius
\mathbf{R}	control weighting matrix
s	Laplace variable
\bar{s}	normalized Laplace variable, \bar{s}/Ω
$S(s)$	sensitivity transfer function
t	time
\bar{t}	nondimensional time, $\bar{t} = \Omega t$
T	rotor thrust, positive upward
T^*	kinetic coenergy of the rotor blade
\mathbf{u}	control input vector
u_P	velocity ratio of blade section, normal to disk plane
u_R	velocity ratio of blade section, in radial direction
u_T	velocity ratio of blade section, parallel to disk plane
U	section resultant velocity ratio, $\sqrt{u_T^2 + u_P^2}$
V	potential energy of the rotor blade
x	rotating blade chordwise coordinate
\tilde{x}	non-rotating coordinate positive aft
\bar{x}	normalized chordwise coordinate, x/c
x_{cg}	center of gravity offset, positive aft of quarter chord
\mathbf{x}	state vector
\tilde{y}	non-rotating coordinate positive to the right
\mathbf{y}	output vector
z	blade coordinate, positive upward
\tilde{z}	rotor coordinate, positive upward
α	blade section angle of attack
α_d	rotor disk angle with respect to helicopter velocity
β	flapping angle, positive upward
γ	Lock number, $\rho acR^4/I_b$
Γ	aerodynamic hub reaction matrices, see Appendix B
Δ	dynamic matrices, see Appendix B
η	servoflap angle
θ	blade sectional pitch angle

θ_r	blade root pitch angle
θ_k	modal coordinate for the k th torsion mode
λ	rotor inflow ratio, $\lambda_f + \lambda_i$
λ_c	vertical climb inflow ratio
λ_f	free stream inflow ratio, $(V \sin \alpha_d + v)/\Omega R$
λ_i	induced inflow ratio, $v/\Omega R$
Λ	aerodynamic matrices, see Appendix B
μ	rotor advance ratio, $V \cos \alpha_d / \Omega R$
ν_β	blade flapping frequency
$\bar{\nu}_\beta$	normalized blade flapping frequency, ν_β / Ω
$\xi_\beta(r)$	blade flapping fundamental mode shape, $(r - e)$
$\xi_{\theta_k}(r)$	k th torsional mode shape
ξ_{θ_k}	k th torsional mode shape vector
ρ	air density
σ	rotor solidity $Nc/\pi R$
ϕ	section inflow angle, $\tan^{-1}(u_P/u_T)$
Φ	inertial hub reaction matrices, see Appendix B
ψ	azimuth angle of rotor blade
ψ_q	azimuth angle of q th rotor blade
Ψ	root pitch actuation matrices, see Appendix B
ω_β	free-flapping frequency, $\sqrt{K_\beta/I_\beta}$
$\bar{\omega}_\beta$	normalized free-flapping frequency, ω_β / Ω
ω	frequency [rad/s]
$\bar{\omega}$	nondimensional frequency ω / Ω
ω_k	natural frequency of k th torsion mode
$\bar{\omega}_k$	normalized natural frequency of k th torsion mode, ω_k / Ω
Ω	rotor speed [rad/s]

Subscripts

0	collective
c	longitudinal cyclic
f	free stream
i	induced flow
k	torsional mode number

r	blade root
s	lateral cyclic

Superscripts

*	normalized by I_b
'	derivative with respect to \bar{r}
n	exponent on r , see Appendix A
T	transpose

Chapter 1

Introduction

Conventional helicopter rotors are controlled through a swashplate, a mechanism which transmits commands from the fixed frame to blade root pitch angles in the rotating frame. An alternative method to helicopter rotor control involves the use of blade-mounted trailing edge flaps to twist the rotor blades. One possible method to actuate trailing edge flaps is the use of piezoelectric materials [43].

Before proceeding with full-scale testing, an analytical tool to evaluate servo-flap performance for various rotor control applications would be useful. This thesis will present the refinement of a helicopter rotor model equipped with blade-mounted aerodynamic actuators, as well as conventional root pitch actuation. Specifically, a linear time invariant (LTI) state space model is developed, which allows the servo-flap rotor system to be evaluated using classical and multivariable control techniques. Using the state space model, parametric studies are performed and control techniques for vibration suppression are investigated.

1.1 Conventional Helicopter Rotor Control

In a conventional helicopter, rotor control is achieved through full-blade feathering. Various root pitch actuators which operate in the rotating or fixed frame have been developed. Traditionally, full-blade feathering is accomplished with a swashplate controlled by linear hydraulic actuators in the fixed frame. Collective control refers to

the vertical movement of the swashplate. Collective swashplate commands simultaneously increases the pitch of all the blades to provide thrust control. Tilting the swashplate generates cyclic commands which vary the blade pitch angle sinusoidally with a period of one rotor revolution. This effectively tilts the rotor disk in the desired direction, providing maneuvering control. To a lesser extent, electro-hydraulic actuators in the rotating frame have been used to provide root pitch control. The development of such an actuator is described in Reference 21.

Much research effort has been directed at the use of swashplate actuation for higher harmonic control (HHC), in which most of the control effort is centered at the $N\Omega$ frequency, where N is the number of blades and Ω is the angular velocity of the rotor. A survey by Hooper of wind tunnel and flight test data concluded that blade-vortex interaction (BVI) is the primary source of $N\Omega$ rotor vibration [18]. Work on HHC conducted by Boeing, Hughes, Sikorsky, NASA, and many other organizations has led to successful wind tunnel and full scale flight testing [49], [30], [39], [40]. In general, electrohydraulic actuators drive the swashplate at $N\Omega$ on top of the standard collective and cyclic controls commanded by the pilot. The $N\Omega$ swashplate commands in the fixed frame are modulated to $(N - 1)\Omega$, $N\Omega$, and $(N + 1)\Omega$ pitch variations in the rotating frame. There are a number HHC algorithms used to provide closed loop vibration control. Some of these techniques will be discussed further in Chapter 4. For now, a brief overview of HHC research based on root pitch actuation is presented.

Reference 49 describes the development of an HHC system for a 4-bladed OH-6A helicopter and subsequent flight testing. This work was conducted by Hughes under contract with NASA and the U.S. Army. Flight tests were conducted with open- and closed-loop HHC at speeds up to 100 knots. Three hydraulic actuators provide 4Ω swashplate commands on top of the standard collective and cyclic commands. These devices were capable of producing harmonic root pitch amplitudes of 1 deg at up to 90 Hz. All three actuators could provide 2 deg of collective authority. Accelerometers mounted beneath the pilot seat measured vertical, lateral, and longitudinal forces. Open-loop or manual testing involved varying the phasing of the 4Ω commands to reduce RMS levels of vibration. An adaptive controller based on a Kalman filtering

scheme to estimate plant parameters was used to close the loop. Both open- and closed-loop testing demonstrated significant reduction in vibration levels, with the open-loop testing showing better overall reduction. Vibration attenuation varied with forward speed. In all flight cases, increases in blade bending and pitch link loads were noted.

Sikorsky implemented HHC on a 4-bladed S-76 helicopter to determine the extent of open-loop vibration reduction [30]. Flight tests at speeds up to 150 knots were conducted including climb/descent and turn maneuvers. Electro-hydraulic driver actuators were placed at the input sides of the main rotor swashplate servos. These actuators provided ± 1 deg pitch amplitudes at up to 20 Hz. Flight tests showed good vibration reduction which was nearly constant with airspeed. A theoretical analysis predicted an optimum pitch amplitude of 2 deg for vibration reduction at 150 knots, but the available actuators were limited by the hydraulic fluid flow capacity. These tests also noted a load increase on the pitch links used for main rotor control.

An extensive program of HHC analysis, design, and testing was conducted by Boeing Helicopters over several years. Reference 39 traces the development of a 4-bladed HHC model rotor from analytical study to wind tunnel testing in the late 70's. 90% suppression of 4Ω vertical force, pitching moment, and rolling moment was demonstrated on a scaled, 4-bladed, 3.05 m diameter hingeless rotor. The swashplate was controlled by extremely accurate electro-hydraulic servos that could provide 1.5 deg pitch commands at 90 Hz. This HHC system also incurred an increase in control loads, blade fatigue loads, and required power. Specifically, a maximum 65% increase in pitch link loads was noted at an advance ratio of 0.3, and overall power requirements increased 1.7%.

Wind tunnel HHC testing of a dynamically scaled 3-bladed CH-47D Chinook rotor was conducted by Boeing Helicopters in 1985 [40]. This rotor was flown through a wide test envelope at speeds up to 188 knots. Specially designed hydraulic actuators featuring long seal life could provide 3 deg of pitch variations at 69 Hz, which corresponds to the 3Ω frequency. The servo-loop design enabled very precise control of amplitude and phase (within 5%). Four equally spaced actuators were connected

to the swashplate as opposed to the typical three actuator configuration. Using a strain gage balance to measure rotating hub loads, various HHC control laws were evaluated. These included adaptive, scheduled gain, and fixed gain algorithms with the fixed gain controller providing the best vibration reduction. A control loop response bandwidth of 1 Hz was deemed sufficient for maintaining HHC performance during maneuvers and gusts. The resulting HHC system was able to continuously and simultaneously suppress three vibratory components over a wide range of changing operating conditions. The fixed gain system provided a 90% reduction in 3Ω vertical force and 2Ω and 4Ω inplane shears throughout the test envelope.

Individual blade control (IBC) is a concept in which blade-mounted actuators and sensors provide appropriate control in the rotating frame. The application of IBC towards gust alleviation, attitude stabilization, vibration reduction, lag damping augmentation, and stall flutter suppression is described by Ham [17]. An effective IBC system is defined by several subsystems, each of which controls a specific blade mode, *i.e.*, first flapwise bending, first torsional, etc. Most IBC work to date utilizes root pitch as the control input. Wind tunnel tests incorporated electrohydraulic servos in the rotating frame and blade mounted accelerometers as sensors. For a 3-bladed rotor, IBC can be accomplished using swashplate actuation, since the swashplate has three degrees of freedom (collective, lateral tilt, and longitudinal tilt).

Using the root pitch actuation, significant progress has been made in helicopter rotor control, particularly in the area of vibration alleviation. However, the swashplate mechanism is limited by its three degrees of freedom and by increased control loads and blade stresses associated with feathering the entire rotor blade. Placing root pitch actuators in the rotating frame provides more degrees of freedom, but increases the complexity of the rotor hub design. The additional electrohydraulic equipment increases the operating cost of the aircraft and imposes a weight penalty. A more elegant method of rotor control which uses a minimum of control effort is desired.

1.2 Alternative Rotor Control Methods

In addition to the swashplate, blade-mounted methods which provide aeroelastic actuation in the rotating frame have been developed. Motivation for these blade-mounted alternatives include performance enhancement [16], improved vibration control [27], and individual blade control (IBC) [17]. Blade-mounted actuation methods include circulation control [28], [20], and mechanical servo-flaps [7],[23]. More recently, piezoelectric materials have been used for aeroelastic control [22], [4], [43]. In addition, passive blade-mounted devices which include tuned flaps and free tips have also been investigated [5], [45].

1.2.1 Circulation Control

Circulation or jet flap control of airfoils is based on the Coanda effect, in which tangential air flow along a rounded airfoil delays boundary layer separation, providing a relatively high sectional lift. Jet flap rotors utilize fairly conventional airfoil shapes with trailing edge slots for air flow, which are sometimes used for propulsion. In general, circulation control rotors (CCR's) utilize elliptical airfoil blades equipped with blowing slots on the trailing and/or leading edges. Air flow is supplied in the hub fixed frame and conducted to the rotating blades through some type of duct system. Research effort has been directed at using this actuation method for trim and vibration control of rotor systems for the past two decades.

The Giravions Dorand Jet-flap rotor was tested in the NASA-Ames 40×80 wind tunnel in the early 70's [28]. This 12 m diameter, two-bladed teetering rotor was equipped with jet flaps which provided rotor propulsion, as well as higher harmonic control. A conventional swashplate provided collective and monocyclic root pitch commands. HHC jet flap control at 2Ω , 3Ω , and 4Ω was controlled by a cam mounted in the fixed hub frame. This rotor demonstrated a simultaneous 50% reduction in blade bending and vertical hub loads for advance ratios in the range $\mu = 0.4\text{--}0.6$.

A non-propulsive jet flap rotor was investigated in Reference 36. The rotor was modelled after the Bell UH-1A with jet flaps along the outer half span. The objective

of this study was to eliminate root shear forces while monitoring blade bending loads and power. Conventional root pitch was used for trim control with the jet flaps providing $2\text{--}11\Omega$ control. It was found that the elimination of root shear loads was due to the elastic twisting caused by the jet-flaps.

A notable CCR project which led to actual flight testing is the XH-2 flight demonstrator program. Reference 20 traces the development and evolution of this CCR program. Initial analytical work predicted substantial vibration reduction using higher harmonic inputs. The XH-2/CCR was first tested on the whirl stand and in the wind tunnel. Airflow to the rotating blades was regulated using a flex ring valve (FRV) system. Inlets to the blades pointed downward facing a flexible swashplate-like ring. By pushing this ring up against the inlets, airflow is restricted. Collective control is achieved by moving the ring vertically, cyclic control by tilting the ring, and higher harmonic control by warping the ring. Collective control was augmented by a conventional swashplate. Flight testing of the XH-2 indicated the heavy lift capability of CCR's. Defined benefits included a reduction of profile drag due to boundary layer control, a corresponding 20–25% reduction in required rotor torque, higher efficiency at higher blade loadings compared to conventional rotors, and a pneumatic control system with smaller control loads.

The X-wing is a V/STOL concept in which the aircraft operates as a conventional rotor at hover and low flight speeds and converts to a fixed wing craft at higher speeds. Four X-wing programs were conducted at the David Taylor Naval Ship Research and Development Center (DTNSRDC) [1], the Lockheed California Company (LCC) [2], Boeing Vertol [37], and Sikorsky [47]. All of these rotors incorporated an elliptical airfoil shape with chord thickness tapered toward the tip. Air flow was provided to the blades by an azimuthally spaced valve system at the hub. The DTNSRDC X-wing project was dubbed the RBCCR (Reverse Blowing Circulation Control Rotor). The RBCCR was a 6.7 ft diameter rotor with very rigid blades and a valve-type control system consisting of eight azimuthally spaced valves. A number of wind tunnel test were conducted from 1975 to 1979 to prove the aerodynamic feasibility of the circulation control concept. A 25 ft diameter X-wing was developed by Lockheed as a

demonstrator model and was tested in the NASA-Ames 40×80 ft wind tunnel and the LCC whirl tower. This model demonstrated conversion from rotating to fixed wing flight at flight speeds up to 180 knots. The Boeing 10 ft. X-wing model incorporated 16 trailing edge valves and 9 leading edge valves to maintain lift on the retreating side of the rotor. Circulation control could be provided from the first through fifth harmonics. In addition, the Boeing X-wing featured mechanical collective pitch control from 8 to -12 deg. The Boeing CCR also demonstrated HHC control techniques to reduce flapwise bending loads. The X-wing model tested at the Sikorsky/United Technologies Research Center was a 1/6 scale, 10 ft diameter 4-bladed rotor which was equipped with two rings of 24 azimuthally spaced valves. The upper ring supplied trailing edge blowing while the lower one fed leading edge slots. Using man-in-the-loop HHC, 70–95% vibration reductions were achieved.

1.2.2 Mechanical Servo-Flaps

The use of blade-mounted servo-flaps for rotor control was demonstrated as early as 1950 [7]. This “aerodynamic servo-controlled helicopter rotor system” featured an outboard flap mounted on a spar at the 75% radial station. The flap was essentially an external airfoil whose lift, acting at moment arm about the pitch axis, provided a torsional moment to twist the rotor blade. The servo-flap was actuated through a mechanical linkage system of bell cranks and push-pull rods and could be deflected up to 15 deg. Using only flap actuation, the rotor system could produce up to 1500 lbs of thrust and ± 7 deg of rotor tilt, more than sufficient for trim and maneuvering control. One drawback to the system was a 6.5% increase in required power attributed to profile drag of the flap servomechanism. An analytical model of this rotor system was presented by Payne in 1959 [33].

While not strictly a servo-flap system, a rotor system with an independently movable inboard blade panel was presented in Reference 11. The motivation for this system was to improve propulsive capability at higher advance ratios which was accomplished by prescribing a non-harmonic pitch schedule for the inboard panel. This system could provide 9 times the maximum thrust of a comparable conventional rotor

and maintain an advance ratio μ as high as 0.60. A recommendation for further work on this system included the use of a large chord trailing edge flap to obtain similar results.

The use of blade-mounted trailing edge servo-flaps has been continuously developed by Kaman Corporation, and has been implemented in current helicopters, including the SH-2 Seasprite and the K-1200 Synchropter. The Seasprite utilizes torsionally rigid blades with soft torsional springs at the root so that the entire blade “follows” the servo-flap command. The K-1200 has dual two-blade intermeshing rotors with a teetering root configuration. The K-1200 servo-flaps utilize elastic blade twist for rotor control. In these designs, servo-flap deflections are commanded by a swashplate. Both of these rotors exhibit significantly lower control loads compared to conventional root pitch actuation.

As with the system presented in Reference 7, the Kaman CTR (Controllable Twist Rotor) actuates the rotor by providing an aerodynamic moment to twist the blade producing a favorable spanwise pitch angle distribution. References 3 and 48 discuss the importance of blade pitch angle distribution to rotor operation. It was concluded in Reference 48 that a high negative twist provides lower power requirements at low flight speeds while a lower negative twist can minimize vibratory loads at higher speeds. Reference 3 concluded that a “torsionally flexible blade with dual control inputs at the blade root and blade tip can provide significant improvements over existing rotor systems.” This work and others provided motivation for the CTR.

A number of reports document the development of the Kaman CTR from analysis to experimental wind tunnel testing [23], [24], [26], [29]. The baseline CTR was based on the 4-bladed H-34 rotor system. The flaps were actuated through a system of rods and cranks controlled by a secondary swashplate. This swashplate was in addition to the primary one for root pitch control. Reference 38 outlines the development of the CTR from preliminary analytical work to pre-wind tunnel testing design work and provides a thorough description of the CTR hardware design and rotor parameters. Reference 24 presents a broad parametric evaluation of the CTR system to find an optimum configuration. The variable parameters were built-in twist, torsional stiff-

ness, faired vs. external flap, flap size, and flap placement. These design parameters were chosen to minimize rotor power, blade bending loads, and maximum local angle of attack. Based on this analytical work, the benefits of the CTR included a 30% decrease in rotor solidity compared to a conventional rotor producing 1 g of thrust, a 15% reduction in required power, and a 30% decrease in blade bending loads.

In addition, the use of higher harmonic or multi-cyclic control on the CTR led to development of the multi-cyclic controllable twist rotor (MCTR). The analysis presented in [26] predicted the virtual elimination of vibratory loads, as well as a 50% reduction in blade bending moments using a combination of 1 through 4Ω control inputs. Reference 46 outlines the development of a feedback control system for the MCTR. Results from MCTR testing in the 40×80 ft NASA-Ames wind tunnel are presented in [29]. A significant reduction in blade bending moments and blade-root actuator control loads was achieved. For the MCTR, special electro-hydraulic actuators were placed in the rotating frame to provide higher harmonic servo-flap control. These actuators could provide flap deflections of up to 6 deg at 2Ω , 3Ω , and 4Ω . An additional feature of the CTR system was automatic blade tracking. This was accomplished with small electric motors in the rotating frame which would provide the appropriate offset to the individual servo-flap control rods.

1.2.3 Piezoelectric Actuation

Recently, the use of so called *smart* materials for aeroelastic control has been the focus of research. Feasibility studies for smart material actuation have been presented in a number of previous works [32], [44], [41]. Specifically, the use of piezoceramic materials has received much attention, due their high strain and high bandwidth capabilities. Direct structural control using piezoelectric materials has been proposed by Lazarus and Crawley [8], [22], Barrett [4], and Nitzsche [31]. Research done by Spangler and Hall [43] investigated piezoelectric actuation of trailing edge servo-flaps.

Lazarus and Crawley demonstrated the use of piezoceramic material to induce strain in isotropic and anisotropic plates [8]. Using composite plates with bending/twist and extension/twist coupling, Lazarus was able to perform closed-loop con-

trol of a plate-like lifting surface in the wind tunnel [22]. While applicable to smaller lifting surfaces such as missile fins, this type of actuation scheme may not have enough authority for rotor blade control. A drawback is the structural bending and twist coupling that is required. This may not be feasible for a typical rotor blade which has a high aspect ratio compared to fixed wings.

In the area of helicopter rotor control, Barrett developed the concept of directionally attached piezos (DAP's) in an attempt to uncouple torsional and bending actuation [4]. Using partial attachment and shear lag effects, a piezoelectric actuator with essentially isotropic properties could be incorporated into the rotor blade structure. Barrett applied DAP's to a 1/8 scale rotor model from the ITR program and managed to produce ± 2 deg of pitch deflection at resonance. At DC, the pitch response was only ± 0.1 deg. Using the DAP system, active flapping vibration control using tip accelerometer feedback provided a 96% reduction in tip deflection amplitudes.

One proposed method of rotor blade structural control utilizes embedded piezoelectric polymer film sensors and piezoceramic actuators [31]. These devices would be specially shaped to sense and actuate specific blade modes. A perfectly collocated sensing/actuation scheme is highly desirable from a control systems standpoint. Part of the motivation for this concept is the development of a simple IBC modal control system as described by Ham [17]. A drawback to this approach, as is the case with many smart material methods, is the limitation of available material properties. Most materials cannot produce enough strain or have limited bandwidth to implement certain smart structure concepts. Shape memory alloys have high force capability, but have very low bandwidth, making them useful for only quasi-static applications. Piezoceramics are high bandwidth actuators, but cannot exert enough strain for high authority structural control of specific blade modes.

A novel approach to incorporate these smart materials into rotor control is the use of piezoceramic actuators to drive an aerodynamic surface, *i.e.*, a trailing edge flap. Instead of high authority control of the rotor blade structure, these piezo servo-flaps would redirect aerodynamic energy to twist the rotor. One approach is a piezo-bender

configuration developed by Spangler and Hall [41], [42], which is also the subject of ongoing research at MIT. Piezoceramics are essentially large force, small displacement actuators. The trick is to amplify the small displacements to relatively larger ones needed for servo-flap deflection.

Spangler and Hall [43] used a cantilever bender element which translates the bender's tip deflection to servo-flap deflection through a hinge mechanism. This device utilized impedance matching arguments to define an optimal flap hinge geometry. This optimal geometry insures that the strain energy created by the piezoceramic bender is efficiently transmitted to flap hinge moment. In the wind tunnel, peak-to-peak flap amplitudes of 14.5 deg at 4 Hz and an air speed of 11.2 m/s were demonstrated [41]. Extrapolating to full scale, a peak-to-peak amplitude of 10.4 deg at 11.25 Hz and an air speed of 148 m/s is achievable. This corresponds to a servo-flap at the 70% span of a Boeing Chinook rotor in hover, providing 3Ω actuation. This actuation method has been proven in typical section testing and is currently being refined. By using a flexure assembly instead of mechanical hinges and constructing a more efficient piezoelectric bender element, performance improvements over the original design are anticipated. Benefits of piezoelectric servo-flap include high bandwidth capability and a relatively simple design. Instead of a mechanical linkage system from the fixed to rotating frame, these solid state devices can be controlled by simple electrical sliprings. Their modular design also allows for a spanwise segmented flap configuration.

Servo-flap actuation is chosen as the focus of this thesis because of its extensive development and implementation in current helicopter designs. Before proceeding with rotating frame testing, an analytical tool to evaluate the performance of a servo-flap rotor system is desirable. A fundamental issue is the amount of servo-flap deflection and associated control loads required for various rotor applications. Servo-flap actuator dynamics are neglected so that any actuation method, not specifically piezoelectric, can be evaluated separately.

1.3 Thesis Objective and Overview

Due to the complexity of the helicopter rotor's operating environment, even in ideal conditions, a comprehensive aeroelastic computer simulation is required to predict the rotor's behavior with some degree of accuracy. In general, rotor analysis routines are based on a time marching, iterative solution technique, and incorporate, to some degree, non-linear aerodynamic and structural effects. These tools are an important developmental step before proceeding with actual hardware construction but are ill-suited for certain tasks. A simpler and faster analysis would be useful for parametric studies and as a preliminary design tool. The objective of this thesis is to present a refined state space model of a helicopter rotor which incorporates blade-mounted flaps and root pitch control. This model will be used to demonstrate the effectiveness of these two actuation methods for various *smart rotor* applications.

Chapter 2 outlines the derivation of the LTI state space rotor model. Important simplifying assumptions include time invariant dynamics and linear aerodynamics. The LTI approximation is accomplished by using multi-blade coordinates (MBC) to transform dynamics from the rotating to the fixed frame. This work is an extension of initial research done at M.I.T. by Fox [12]. Portions of the model derivation chapter are taken from [12, Chapter 4]. New additions to this rotor model include span-varying rotor blade parameters, a chordwise center-of-gravity offset which couples rigid flapping and elastic pitch, a δ_3 hinge which couples rigid flapping and rigid pitch, an arbitrary number of torsional modes, and separate aerodynamic and structural rotor integrals.

Chapter 3 presents validation results and a number of parametric studies using the state space rotor model. The aeroelastic rotor program C60 developed by Boeing Helicopters is used to validate the state space model at discrete frequency points, 0Ω , $N\Omega$, and $2N\Omega$. Using continuous frequency responses, the effect of parameter variations on the open loop helicopter rotor plant is investigated. Of primary interest is the thrust response due to collective root pitch and servo-flap control inputs. Important parameters are the rotor blade's torsional stiffness and servo-flap placement.

In addition, the effect of center-of-gravity offset from the pitch axis and additional mass due to the actuator is investigated.

In Chapter 4, higher harmonic control (HHC) techniques are applied to the open loop helicopter plant derived in Chapter 2. Based on previous work on HHC algorithms [15], a continuous time compensator will be applied to individual transfer functions to compare the closed loop performance of root pitch and servo-flap actuation. A frequency weighted linear quadratic regulator (LQR) approach will be applied to the state space rotor model to demonstrate multivariable vibration reduction. In addition, the required control effort of root pitch and servo-flap actuators for HHC will be compared. Finally, a summary of the important conclusions and some suggestions for further development of the state space rotor model will be presented in Chapter 5.

Chapter 2

State Space Rotor Model

In this chapter, a state space model of an actively controlled helicopter rotor is derived. A semi-articulated rotor model with rigid blade flapping and elastic torsion is assumed. The inputs to this system are root pitch angle and servo-flap deflection. The outputs of interest are the hub loads: vertical force, pitching moment, and rolling moment. The model is derived by first finding the equations of motion governing the structural blade dynamics *in vacuo* or in the absence of aerodynamic effects. The aerodynamic loads which force the system are then derived. The dynamics and forcing terms will be derived in the rotating frame and then transformed to the fixed frame using multi-blade coordinates. In addition, a dynamic inflow model developed by Pitt and Peters [35] will be presented. Finally, the three major elements of the model (structural dynamics, aerodynamic loads, and dynamic inflow) are coupled together as shown in Figure 2-1. Before proceeding with the derivation, the notation and coordinates used in describing the helicopter rotor system will be explained.

2.1 Rotor Coordinates

The coordinates of the rotor disk may be described by the polar coordinates r , the radial position, and ψ , the azimuthal angle. In general, American helicopter rotors rotate counter-clockwise (looking down on the rotor disk) with a constant rotational frequency denoted by Ω . The azimuthal and radial coordinates are illustrated in

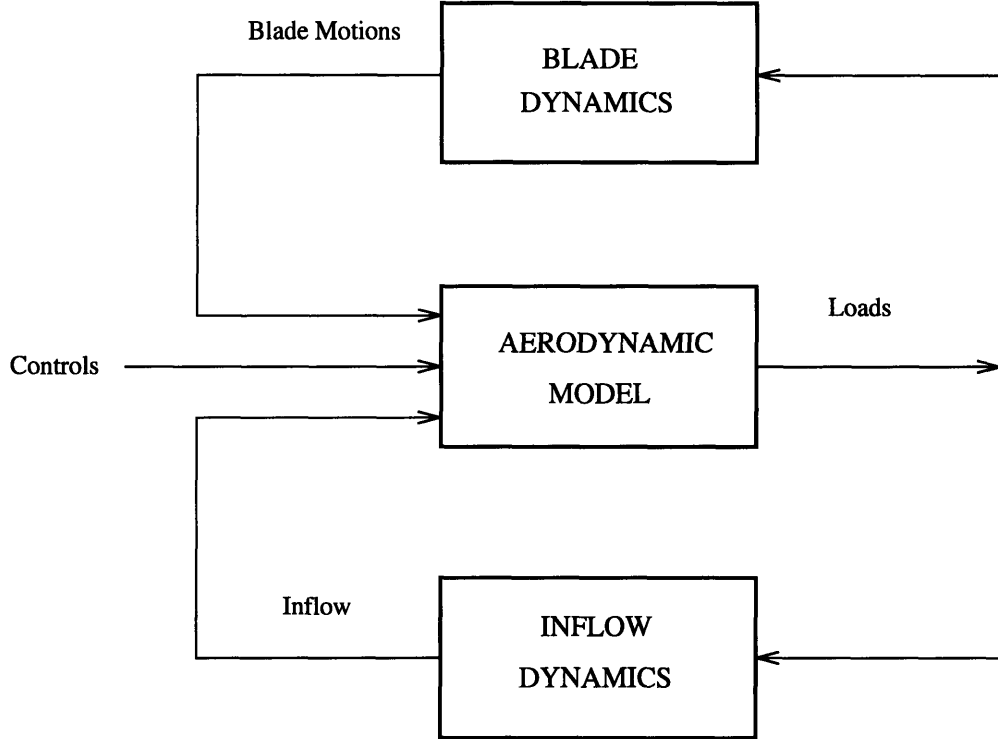


Figure 2-1: Block diagram of coupled rotor and inflow dynamics. Adapted from Pitt and Peters [35].

Figure 2-2. Often, the right and left halves of the rotor disk are referred to as the advancing and retreating sides, respectively. The servo-flap spans the rotor blades from r_1 to r_2 and deflects an angle η defined positive downward. For this model, each rotor blade is allowed to pitch rigidly and elastically with an angle θ , defined positive nose up, and rotate rigidly about a flapping hinge at $r = e$ with an angle β , defined positive up. The rotor blade airfoil spans from $r = r_c$ to R . The sectional coordinate frame of the rotating blade is illustrated in Figure 2-3. For this model, the pitch axis coincides with the elastic axis and aerodynamic center at the quarter chord. The center-of-gravity or c.g. offset is denoted by x_{cg} , defined positive aft of the quarter chord. A nonrotating cartesian coordinate frame is attached at the hub center with \tilde{x} pointing aft ($\psi = 0$ deg), \tilde{y} to the right ($\psi = 90$ deg), and \tilde{z} pointing upward. The rotor hub loads are evaluated relative to this nonrotating frame. In addition, a coordinate frame rotates with the rotor blade with the x axis pointing toward the trailing edge, the r axis pointing toward the tip along the quarter chord,

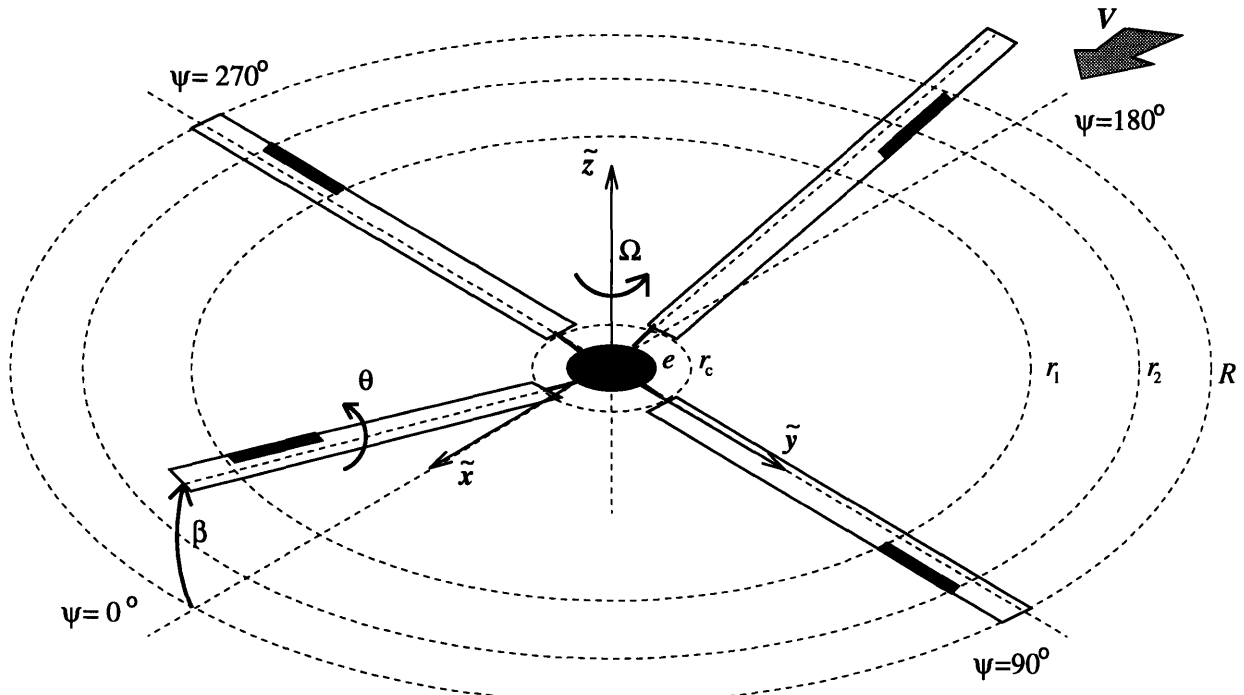


Figure 2-2: Helicopter rotor coordinates.

and the z axis pointing upward. The rotor blade's dynamics and sectional properties are evaluated using this rotating coordinate frame. For convenience, the normalized radial position is $\bar{r} = r/R$, and the normalized chordwise position is $\bar{x} = x/c$.

2.2 Multi-Blade Coordinates

In general, the dynamics of a rotor system are periodic, but the evaluation of continuous frequency response functions requires a linear time-invariant (LTI) assumption. Using multi-blade coordinates (MBC), an LTI approximation of the rotor dynamics will be derived. The mathematics involved in transforming the blade's degrees of freedom in the rotating frame to the rotor disk modes in the non-rotating frame are presented in this section. A more formal treatment of multi-blade coordinates is given in Johnson [19, Chapter 8].

Using the discrete Fourier series, one can fit a periodic function at several discrete points. In the case of a helicopter rotor, these points are the azimuthal blade locations.

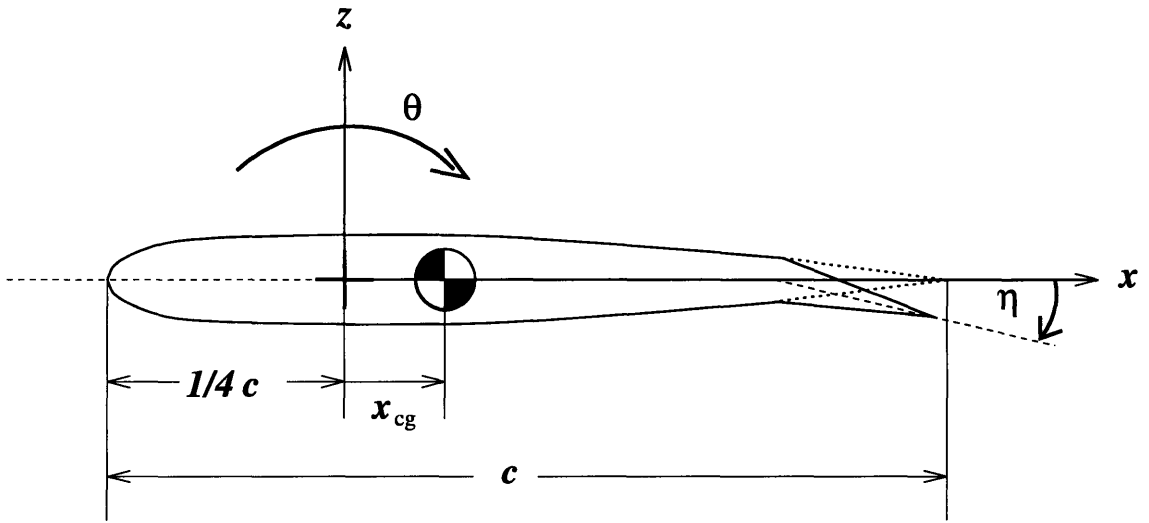


Figure 2-3: Sectional rotor blade coordinates.

Multi-blade coordinates use the N lowest Fourier coefficients to transform from rotor blade degrees of freedom in the rotating frame to rotor disk modes in the fixed frame. The total number of degrees of freedom are maintained, because there is a degree of freedom for each of the N blades. For example, the flap angles of the rotor blades are $\beta_1, \beta_2, \dots, \beta_N$. The blade angles are transformed by the discrete Fourier series to the fixed frame coefficients $\beta_0, \beta_{1c}, \beta_{1s}, \dots, \beta_d$, which represent flapping modes of the rotor disk. The fixed frame coefficients are

$$\beta_0 = \frac{1}{N} \sum_{q=1}^N \beta(\psi_q), \quad (2.1)$$

$$\beta_{nc} = \frac{2}{N} \sum_{q=1}^N \beta(\psi_q) \cos(n\psi_q), \quad (n < N/2) \quad (2.2)$$

$$\beta_{ns} = \frac{2}{N} \sum_{q=1}^N \beta(\psi_q) \sin(n\psi_q), \quad (n < N/2) \quad (2.3)$$

$$\beta_d = \frac{1}{N} \sum_{q=1}^N \beta(\psi_q) (-1)^q, \quad (N \text{ even}). \quad (2.4)$$

The coefficients $\beta_0, \beta_{nc}, \beta_{ns}$, and β_d are the multi-blade coordinates, and ψ_q is the azimuthal position of the qth blade ($1 \leq q \leq N$). The differential term β_d exists only when there are an even number of blades. For the purpose of this research, we will

retain only the first three multiblade coordinates. The remaining differential terms represent reactionless modes which cause no net hub force or moment. Therefore, the MBC expansion of the flapping angle will be given by

$$\beta(\psi) = \beta_0 + \beta_c \cos \psi + \beta_s \sin \psi . \quad (2.5)$$

It is also assumed that all of the rotor blades behave identically. Figure 2-4 illustrates the transformation from the rotating frame flapping angle, β , to the rotor disk modes, β_0 , β_c , and β_s . The *coning* mode is represented by the collective coordinate β_0 . The *longitudinal* and *lateral tilt* modes are represented by the cyclic coordinates β_c and β_s , respectively. Two methods for performing the MBC transformation include the substitution method and the summation operator method, which are discussed below.

The substitution method will be used to transform differential equations in the rotating frame to MBC. In this work, the governing equations of motion in the rotating frame will have constant coefficients. The MBC expansion for the degree of freedom is substituted into the rotating frame equation. As an example, an equation of the form

$$m\ddot{x} + kx = f \quad (2.6)$$

will represent the dynamics of x in the rotating frame. Taking derivatives with respect to non-dimensional time ($\psi = \Omega t$), the degree of freedom x is expanded as

$$x = x_0 + x_c \cos \psi + x_s \sin \psi , \quad (2.7)$$

$$\dot{x} = \dot{x}_0 + \dot{x}_c \cos \psi + \dot{x}_s \sin \psi - x_c \sin \psi + x_s \cos \psi , \quad (2.8)$$

$$\ddot{x} = \ddot{x}_0 + \ddot{x}_c \cos \psi + \ddot{x}_s \sin \psi - 2\dot{x}_c \sin \psi + 2\dot{x}_s \cos \psi - x_c \cos \psi - x_s \sin \psi . \quad (2.9)$$

Inserting these into Equation (2.6) and collecting coefficients of similar terms, the

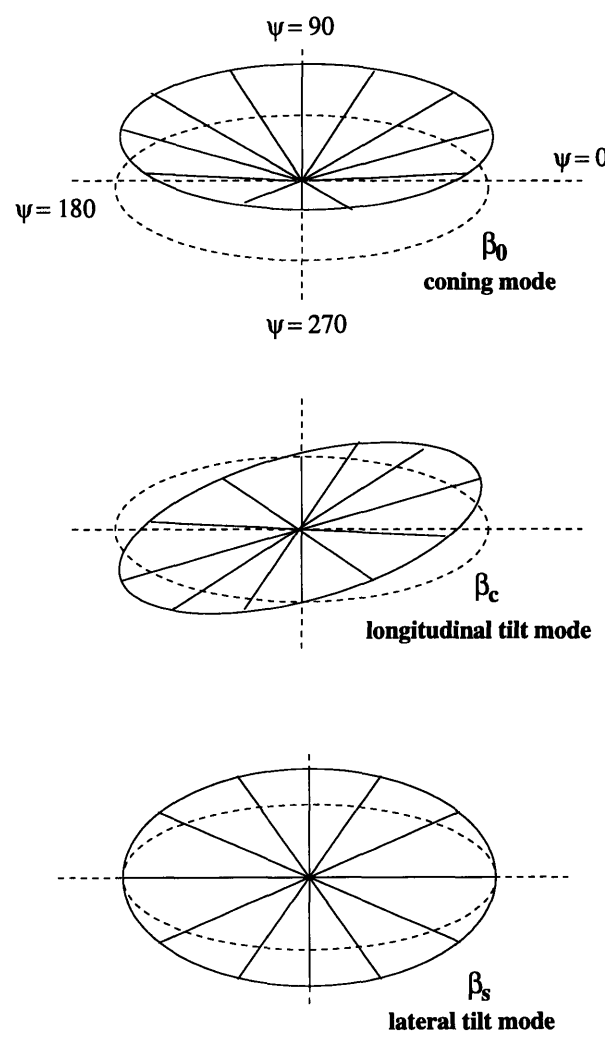


Figure 2-4: MBC transformation from rigid flapping angle to rotor disk modes.

resulting equations of motion in MBC matrix form are

$$\begin{aligned} & \left[\begin{array}{ccc} m & 0 & 0 \\ 0 & m & 0 \\ 0 & 0 & m \end{array} \right] \left\{ \begin{array}{c} \ddot{x}_0 \\ \ddot{x}_c \\ \ddot{x}_s \end{array} \right\} + \left[\begin{array}{ccc} 0 & 0 & 0 \\ 0 & 0 & 2m \\ 0 & -2m & 0 \end{array} \right] \left\{ \begin{array}{c} \dot{x}_0 \\ \dot{x}_c \\ \dot{x}_s \end{array} \right\} + \\ & \left[\begin{array}{ccc} k & 0 & 0 \\ 0 & k-m & 0 \\ 0 & 0 & k-m \end{array} \right] \left\{ \begin{array}{c} x_0 \\ x_c \\ x_s \end{array} \right\} = \left\{ \begin{array}{c} f_0 \\ f_c \\ f_s \end{array} \right\}. \end{aligned} \quad (2.10)$$

In addition to the substitution method, summation operators will be used to transform generalized forces on the blades to forces on the rotor disk modes. The operators are

$$(\cdot)_0 = \frac{1}{N} \sum_{q=1}^N (\cdot), \quad (2.11)$$

$$(\cdot)_c = \frac{2}{N} \sum_{q=1}^N (\cdot) \cos(\psi_q), \quad (2.12)$$

$$(\cdot)_s = \frac{2}{N} \sum_{q=1}^N (\cdot) \sin(\psi_q). \quad (2.13)$$

In general, the rotating frame forces on the blades are periodic aerodynamic loads due to the azimuthally varying velocity field. As an example, the summation operators will be applied to a forcing term of the form

$$f = (1 + \mu \sin \psi)^2 x. \quad (2.14)$$

Using trigonometric identities and inserting the MBC expansion for x , Equation (2.14) is rewritten as

$$\begin{aligned} f = & \left(1 + \frac{1}{2}\mu^2 + 2\mu \sin \psi - \frac{1}{2}\mu^2 \cos 2\psi \right) x_0 + \\ & \left((1 + \frac{1}{4}\mu^2) \cos \psi + \mu \sin 2\psi - \frac{1}{4}\mu^2 \cos 3\psi \right) x_c + \\ & \left(\mu + (1 + \frac{3}{4}\mu^2) \sin \psi - \mu \cos 2\psi - \frac{1}{4}\mu^2 \sin 3\psi \right) x_s. \end{aligned} \quad (2.15)$$

Assuming a three-bladed rotor ($N = 3$), the summation operators yield

$$f_0 = (1 + \frac{1}{2}\mu^2)x_0 - (\frac{1}{2}\mu^2 \cos 3\psi)x_c + (\mu - \frac{1}{4}\mu^2 \sin 3\psi)x_s, \quad (2.16)$$

$$f_c = (-\frac{1}{2}\mu^2 \cos 3\psi)x_0 + (1 + \frac{1}{4}\mu^2)x_c - (\mu \cos 3\psi)x_s, \quad (2.17)$$

$$f_s = (2\mu - \frac{1}{2}\mu^2 \sin 3\psi)x_0 - (\mu \cos 3\psi)x_c + (1 + \frac{3}{4}\mu^2 - \mu \sin 3\psi)x_s. \quad (2.18)$$

Neglecting the periodic coefficients, the MBC forcing vector is

$$\begin{Bmatrix} f_0 \\ f_c \\ f_s \end{Bmatrix} = \begin{bmatrix} (1 + \frac{1}{2}\mu^2) & 0 & \mu \\ 0 & (1 + \frac{1}{4}\mu^2) & 0 \\ 2\mu & 0 & (1 + \frac{3}{4}\mu^2) \end{bmatrix} \begin{Bmatrix} x_0 \\ x_c \\ x_s \end{Bmatrix}. \quad (2.19)$$

For an N -bladed rotor, only N/rev harmonic coefficients will appear in the forcing terms when the summation operators are applied. As N increases, the periodic coefficients are swept upward in frequency and become smaller in magnitude, leaving the first collective and cyclic components to dominate the response. In general, these N/rev periodic coefficients are on the order of μ^2 and may be neglected yielding a linear time invariant approximation for the rotor dynamics. This constant coefficient approximation improves with decreasing advance ratio, μ , and increasing number of blades. For the limiting cases of a rotor in hover or a rotor with an infinite number of blades, this constant coefficient model is exact.

Using the three degree of freedom MBC expansion of Equation (2.7), all inputs, outputs, and state variables will contain terms with factors 1, $\cos \psi$, and $\sin \psi$. The rotor controls will be expressed in terms of collective and cyclic inputs. The hub load outputs will be the thrust, pitching moment, and rolling moment. Furthermore, any internal state variables will have collective and cyclic components. Unless otherwise noted, vector notation will be used to represent the MBC expansion. For example, the MBC vector for the flapping angle is

$$\boldsymbol{\beta} = \begin{Bmatrix} \beta_0 \\ \beta_c \\ \beta_s \end{Bmatrix}. \quad (2.20)$$

In the following sections, the techniques developed in this section will be used to obtain an LTI state space model of the rotor system.

2.3 *In Vacuo* Blade Dynamics

The *in vacuo* blade dynamics include only inertial and elastic effects, and will be derived in this section using Lagrange's method. Specifically, the equations for rigid flapping motion and elastic torsion will be evaluated. The elastic pitch angle of the blade will be represented by the summation of a few spanwise shape functions, $\xi_{\theta_k}(r)$, and corresponding coordinates, θ_k . The defined degrees of freedom are β for the rigid flapping angle and the generalized coordinates θ_k ($k = 1, 2, \dots$) for the elastic pitch angle. Although an arbitrary number of torsional modes may be included in the model, rigid blade flapping without blade bending was assumed. Flapwise bending can be included in the model, but the effects are expected to be minor for an articulated rotor. Once the blade equations of motion are derived, they will be transformed into multiblade coordinates, so that they represent the dynamics of several rotor disk modes.

2.3.1 Torsional Modal Analysis

The sectional pitch angle of the blade is represented by a superposition of rigid pitch, θ_r , and elastic pitch, θ_e , so that

$$\theta(r) = \theta_r + \theta_e(r), \quad (2.21)$$

$$= \theta_r + \sum_k \xi_{\theta_k}(r) \theta_k, \quad (2.22)$$

where $\xi_{\theta_k}(r)$ are spanwise shape functions and θ_k are the generalized twist coordinates which will be normalized by the tip pitch angle. An arbitrary number of shapes functions can be used. The functions $\xi_{\theta_k}(r)$ can be assumed mode shapes or can be evaluated using continuous or lumped models.

A continuous beam model with constant spanwise properties facilitates the use

of natural orthogonal modes with $\xi_{\theta_k}(r)$ as a continuous function of radial position. Solving the modal equation

$$-\omega_k^2 \xi_{\theta_k}(r) - \left(\frac{GJ}{I_\theta} \right) \frac{\partial^2 \xi_{\theta_k}(r)}{\partial r^2} = 0 \quad (2.23)$$

subject to the boundary conditions

$$\theta_k|_{r=e} = 0 \quad (2.24)$$

and

$$GJ \frac{\partial \theta_k}{\partial r} \Big|_{r=R} = 0 \quad (2.25)$$

yields the mode shape and natural frequency for the k th mode,

$$\xi_{\theta_k}(r) = \sin \left(\frac{\pi(k - \frac{1}{2})}{(R - e)} (r - e) \right), \quad (2.26)$$

$$\omega_k = \frac{\pi(k - \frac{1}{2})}{(R - e)} \sqrt{\frac{GJ}{I_\theta}}. \quad (2.27)$$

The k th modal stiffness and inertia are therefore

$$K_{\theta_k} = \int_e^R \xi_{\theta_k}(r) GJ \frac{\partial^2 \xi_{\theta_k}(r)}{\partial r^2} dr, \quad (2.28)$$

$$I_{\theta_k} = \int_e^R I_\theta \xi_{\theta_k}^2(r) dr. \quad (2.29)$$

For orthogonal mode shapes, the dynamics of θ_k ($k = 1, 2, \dots$) will be uncoupled. For arbitrary shapes $\xi_{\theta_k}(r)$ and $\xi_{\theta_j}(r)$, the torsional modes may not be orthogonal which will introduce cross-coupling. The expressions

$$K_{\theta_k \theta_j} = \int_e^R \xi_{\theta_k}(r) GJ \frac{\partial^2 \xi_{\theta_j}(r)}{\partial r^2} dr, \quad (2.30)$$

$$I_{\theta_k \theta_j} = \int_e^R \xi_{\theta_k}(r) I_\theta \xi_{\theta_j}(r) dr. \quad (2.31)$$

represent the stiffness and inertia coupling terms between arbitrary modes k and j .

For a blade with spanwise-varying properties, a lumped parameter model may be

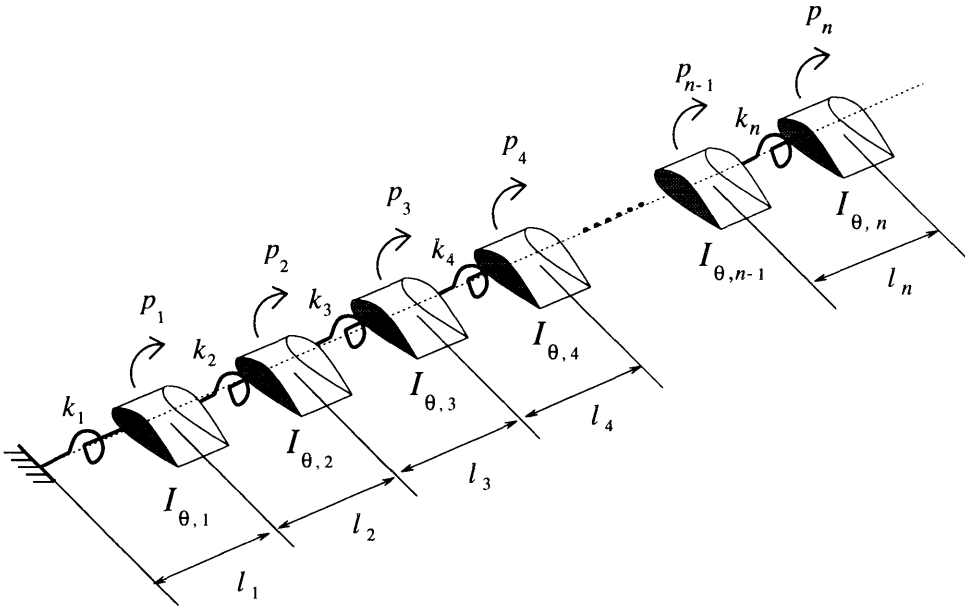


Figure 2-5: Lumped torsional approximation of rotor blade.

employed. The rotor blade is approximated by a string of lumped inertias joined in series by torsional springs as shown in Figure 2-5. The mode shapes and natural frequencies are obtained by solving the following generalized eigenvalue problem

$$\mathcal{K}\xi_{\theta_k} = \omega_k^2 \mathcal{M}\xi_{\theta_k} \quad (2.32)$$

where \mathcal{K} is the stiffness matrix and \mathcal{M} is the mass matrix of the lumped torsional system. Defining the vector ξ_{θ_k} ,

$$\xi_{\theta_k} = \begin{Bmatrix} p_1 \\ p_2 \\ \vdots \\ p_n \end{Bmatrix}_k, \quad (2.33)$$

where p_i is the pitch angle of the i th lumped inertia, the generalized eigenvalue

problem for a lumped torsional system is explicitly presented as

$$\begin{bmatrix} k_1 & -k_2 & & & \\ -k_2 & k_1 + k_2 & -k_3 & & \\ & -k_3 & \ddots & \ddots & \\ & \ddots & k_n + k_{n-1} & -k_n & \\ & & -k_n & k_n & \end{bmatrix} \begin{Bmatrix} p_1 \\ p_2 \\ \vdots \\ p_n \end{Bmatrix}_k = \omega_k^2 \begin{bmatrix} I_{\theta,1} & & & \\ & I_{\theta,2} & & \\ & & \ddots & \\ & & & I_{\theta,n} \end{bmatrix} \begin{Bmatrix} p_1 \\ p_2 \\ \vdots \\ p_n \end{Bmatrix}_k \quad (2.34)$$

where $I_{\theta,i}$ are the lumped pitch inertias and k_i are the lumped torsional springs joining them, defined as

$$k_i = \frac{GJ_i}{l_i}, \quad (2.35)$$

where l_i is the distance between adjacent lumped inertias. The eigenvectors ξ_{θ_k} and corresponding eigenvalues ω_k^2 are the mode shapes and squared natural frequencies of this lumped parameter model. The k th modal stiffness and inertia for this lumped system are

$$K_{\theta_k} = \xi_{\theta_k}^T K \xi_{\theta_k}, \quad (2.36)$$

$$I_{\theta_k} = \xi_{\theta_k}^T M \xi_{\theta_k}. \quad (2.37)$$

2.3.2 *In Vacuo* Equations of Motion

The equations of motion for pitch and flap motion are derived using Lagrange's method. The first step in the derivation is to define the components of the Lagrangian

$$L = T^* - V, \quad (2.38)$$

where T^* and V are the kinetic and potential energies of the system.

Looking at a sectional slice of the rotor blade and assuming a chordwise mass distribution m_x , the sectional properties are

$$m = \int_{-\frac{1}{4}c}^{\frac{3}{4}c} m_x dx, \quad (2.39)$$

$$I_\theta = \int_{-\frac{1}{4}c}^{\frac{3}{4}c} m_x x^2 dx , \quad (2.40)$$

$$x_{cg} = \frac{1}{m} \int_{-\frac{1}{4}c}^{\frac{3}{4}c} m_x x dx . \quad (2.41)$$

A thin airfoil is assumed so that property variations through the thickness are neglected.

The kinetic energy T^* of the entire rotor blade is defined as

$$T^* = \int_e^R \int_{-\frac{1}{4}c}^{\frac{3}{4}c} m_x (v_1^2 + v_2^2) dx dr . \quad (2.42)$$

Only two velocity components of a differential chordwise element of mass, $m_x dx$, will be considered. A component normal to the disk plane, v_1 , is due to the sectional pitch and flapping velocities. A radially tangential component, v_2 , parallel to the disk plane is the product of the angular velocity of the rotor, Ω , and the radial position of the mass element, \tilde{r} , dependent on the pitch and flapping coordinates. The velocity components are illustrated in Figure 2-6, and are given by

$$v_1 = (r - e)\dot{\beta} - x\dot{\theta} , \quad (2.43)$$

$$v_2 = \Omega\tilde{r} , \quad (2.44)$$

$$= \Omega \left([e + (r - e)\cos\beta + x\sin\theta\sin\beta]^2 + [x\cos\theta]^2 \right)^{\frac{1}{2}} . \quad (2.45)$$

To simplify notation, the subscript k will imply a summation. Inserting the expressions for the velocity components (Equations (2.43) and (2.45)), and the pitch angle (Equation (2.22)) into Equation (2.42), and evaluating the chordwise integrals, the

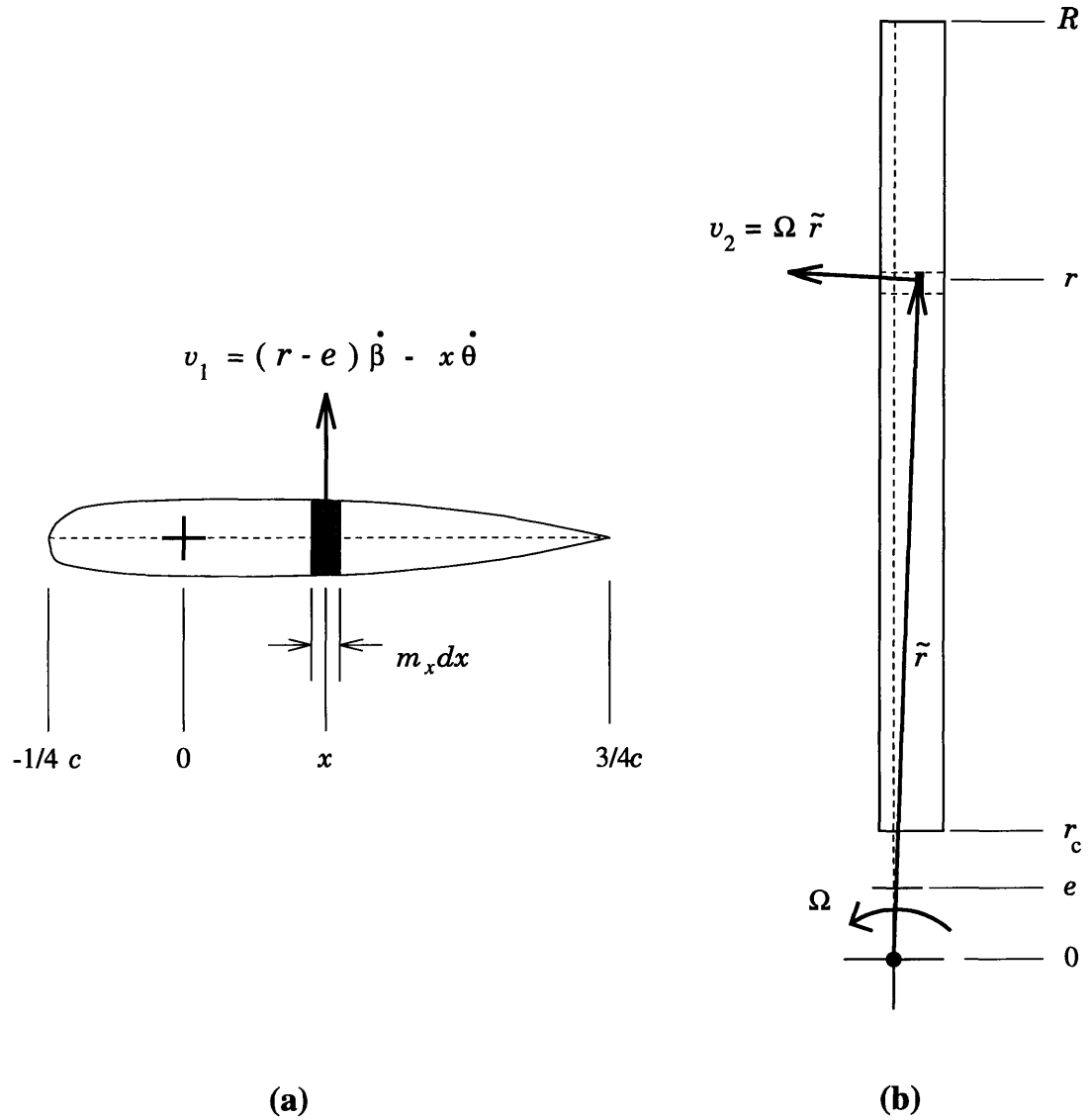


Figure 2-6: Velocity components of differential chordwise element of mass:
(a) sectional view and **(b)** top view.

kinetic energy is rewritten as

$$\begin{aligned}
T^* = & \int_e^R \left[\frac{1}{2}m(r-e)^2\dot{\beta}^2 - mx_{cg}(r-e)\dot{\theta}_r\dot{\beta} - mx_{cg}(r-e)\xi_{\theta_k}(r)\dot{\theta}_k\dot{\beta} \right. \\
& + \frac{1}{2}I_\theta\dot{\theta}_r^2 + I_\theta\xi_{\theta_k}(r)\dot{\theta}_k\dot{\theta}_r + \frac{1}{2}I_\theta\xi_{\theta_k}^2(r)\dot{\theta}_k^2 \Big] dr \\
& + \int_e^R \left[\frac{1}{2}me^2 + me(r-e)\cos\beta + mx_{cg}\sin(\theta_r + \xi_{\theta_k}(r)\theta_k)\sin\beta \right. \\
& + \frac{1}{2}m(r-e)^2\cos^2\beta + \frac{1}{2}mx_{cg}(r-e)\sin(\theta_r + \xi_{\theta_k}(r)\theta_k)\sin 2\beta \\
& \left. + \frac{1}{2}I_\theta\sin^2(\theta_r + \xi_{\theta_k}(r)\theta_k)\sin^2\beta + \frac{1}{2}I_\theta\cos^2(\theta_r + \xi_{\theta_k}(r)\theta_k) \right] \Omega^2 dr . \quad (2.46)
\end{aligned}$$

The potential energy of the rotor blade, which has contributions from the strain energy due to elastic twist and a flapping hinge spring, is given by

$$V = \frac{1}{2}K_{\theta_k}\theta_k^2 + \frac{1}{2}K_\beta\beta^2 , \quad (2.47)$$

where K_β is simply the hinge spring stiffness.

The equations of motion can now be derived for the k th torsional mode and rigid flapping dynamics using Lagrange's method. For convenience, the mode shape $\xi_\beta(r) = (r - e)$ will be used to represent the rigid flapping mode. Higher order terms will be neglected and small angle approximations will be used. Lagrange's equation for the elastic twist coordinate θ_k is

$$\frac{d}{dt} \left(\frac{\partial L}{\partial \dot{\theta}_k} \right) - \frac{\partial L}{\partial \theta_k} = N_k . \quad (2.48)$$

Assuming the modes shapes are orthogonal, the equation of motion for the k th torsional mode is

$$\begin{aligned}
& \left[\int_e^R I_\theta\xi_{\theta_k}^2 dr \ddot{\theta}_k + \left(\int_e^R I_\theta\xi_{\theta_k}^2 dr \Omega^2 + K_{\theta_k} \right) \theta_k \right] \\
& + \left[\int_e^R I_\theta\xi_{\theta_k} dr \ddot{\theta}_r + \int_e^R I_\theta\xi_{\theta_k} dr \Omega^2 \theta_r \right] \\
& - \left[\int_e^R mx_{cg}\xi_\beta\xi_{\theta_k} dr \ddot{\beta} + \int_e^R mx_{cg}r\xi_{\theta_k} dr \Omega^2 \beta \right] = \int_e^R N_{aero} \xi_{\theta_k} dr . \quad (2.49)
\end{aligned}$$

Lagrange's equation for the rigid flapping coordinate β is

$$\frac{d}{dt} \left(\frac{\partial L}{\partial \dot{\beta}} \right) - \frac{\partial L}{\partial \beta} = M_F , \quad (2.50)$$

and the equation of motion for rigid flapping is

$$\begin{aligned} & \left[\int_e^R m \xi_\beta^2 dr \ddot{\beta} + \left(\int_e^R m r \xi_\beta^2 dr \Omega^2 + K_\beta \right) \beta \right] \\ & - \left[\int_e^R m x_{cg} \xi_\beta dr \ddot{\theta}_r + \int_e^R m x_{cg} r dr \Omega^2 \theta_r \right] \\ & - \left[\int_e^R m x_{cg} \xi_\beta \xi_{\theta_k} dr \ddot{\theta}_k + \int_e^R m x_{cg} r \xi_{\theta_k}(r) dr \Omega^2 \theta_k \right] = \int_e^R F_z \xi_\beta dr . \end{aligned} \quad (2.51)$$

The elastic twist and flap dynamics are structurally coupled by the center of gravity offset x_{cg} .

For convenience, the coupled dynamics may be non-dimensionalized and rewritten in matrix form. The resulting equations of motion are

$$\begin{bmatrix} I_{\theta_k}^* & -I_{\theta_k \bar{\beta}}^* \\ -I_{\theta_k \bar{\beta}}^* & I_\beta^* \end{bmatrix} \begin{Bmatrix} \ddot{\theta}_k \\ \ddot{\beta} \end{Bmatrix} + \begin{bmatrix} I_{\theta_k}^* (\bar{\omega}_k^2 + 1) & -I_{\theta_k \beta}^* \\ -I_{\theta_k \beta}^* & I_\beta^* \bar{\nu}_\beta^2 \end{bmatrix} \begin{Bmatrix} \theta_k \\ \beta \end{Bmatrix} = \begin{Bmatrix} -I_{\theta_k \theta_r}^* \\ I_{\beta \theta_r}^* \end{Bmatrix} \theta_r + \begin{Bmatrix} -I_{\theta_k \theta_r}^* \\ I_{\beta \theta_r}^* \end{Bmatrix} \ddot{\theta}_r + \begin{Bmatrix} \bar{N}_k \\ \bar{M}_F \end{Bmatrix} . \quad (2.52)$$

The nondimensional torsional frequency of the k th mode is defined as

$$\bar{\omega}_k = \sqrt{\frac{K_{\theta_k}}{\Omega^2 I_{\theta_k}}} . \quad (2.53)$$

Note that $\bar{\omega}_k$ is the non-rotating natural frequency. The propeller moment, a centrifugal effect, stiffens the blade torsionally; hence the term $(\bar{\omega}_k^2 + 1)$. The nondimensional flapping frequency is defined as

$$\bar{\nu}_\beta = \sqrt{1 + \frac{K_\beta}{\Omega^2 I_\beta} + \frac{\int_e^R m e(r - e) dr}{I_\beta}} \quad (2.54)$$

where I_β is the inertia about the flapping hinge. Note that the blade will flap with

frequency Ω when there is no flapping spring, K_β , or hinge offset, e . The non-dimensional mass and inertial integrals are defined in Appendix A.

Further pitch/flap coupling is introduced when the blade root configuration includes a δ_3 hinge. The effect of the δ_3 hinge is a reduction in the apparent pitch angle relative to the disk plane when the blade flaps up. This can be incorporated into the model by defining a coupling coefficient $K_p = \tan \delta_3$, so that

$$\theta_{act} = \theta - K_p \beta . \quad (2.55)$$

To implement this coupling effect, Equation (2.55) is simply substituted wherever θ_r appears in the dynamics.

Transforming the matrix Equation (2.52) to MBC, the coupled equations of motion are

$$\begin{bmatrix} \Delta_{\theta_k \ddot{\theta}_k} & \Delta_{\theta_k \ddot{\beta}} \\ \Delta_{\theta_k \ddot{\beta}} & \Delta_{\beta \ddot{\beta}} \end{bmatrix} \begin{Bmatrix} \ddot{\theta}_k \\ \ddot{\beta} \end{Bmatrix} + \begin{bmatrix} \Delta_{\theta_k \dot{\theta}_k} & \Delta_{\theta_k \dot{\beta}} \\ \Delta_{\theta_k \dot{\beta}} & \Delta_{\beta \dot{\beta}} \end{bmatrix} \begin{Bmatrix} \dot{\theta}_k \\ \dot{\beta} \end{Bmatrix} + \begin{bmatrix} \Delta_{\theta_k \theta_k} & \Delta_{\theta_k \beta} \\ \Delta_{\theta_k \beta} & \Delta_{\beta \beta} \end{bmatrix} \begin{Bmatrix} \theta_k \\ \beta \end{Bmatrix} = \\ \begin{bmatrix} \Psi_{\theta_k \theta_r} \\ \Psi_{\beta \theta_r} \end{bmatrix} \{ \theta_r \} + \begin{bmatrix} \Psi_{\theta_k \dot{\theta}_r} \\ \Psi_{\beta \dot{\theta}_r} \end{bmatrix} \{ \dot{\theta}_r \} + \begin{bmatrix} \Psi_{\theta_k \ddot{\theta}_r} \\ \Psi_{\beta \ddot{\theta}_r} \end{bmatrix} \{ \ddot{\theta}_r \} + \begin{Bmatrix} \bar{N}_k \\ \bar{M}_F \end{Bmatrix} . \quad (2.56)$$

The various Δ matrices are defined in Appendix B, and are similar in form to the matrices derived in the MBC example. To complete the derivation, the aerodynamic forcing terms \bar{N}_k and \bar{M}_F need to be evaluated. The aerodynamic forcing will introduce additional coupling between the rigid flapping and elastic pitch dynamics.

2.4 Aerodynamic Model

Several simplifying assumptions about non-linear effects and the unsteady aerodynamics have been made to produce a LTI rotor model. These assumptions will be discussed and the aerodynamic forcing terms will be derived and presented in the MBC frame. Before proceeding with the aerodynamic derivation, the nondimensional fixed and rotating frame velocity components will be defined.

The rotor disk may have an angle of attack, α_d , with respect to V , the helicopter

velocity. The velocity of the air relative to the rotor disk may be decomposed into two components, one parallel and one normal to the disk plane. The velocities are non-dimensionalized by the rotor blade tip speed ΩR . The advance ratio μ is the non-dimensional velocity component parallel to the rotor disk plane, defined as

$$\mu = \frac{V \cos \alpha_d}{\Omega R} . \quad (2.57)$$

The inflow λ is the non-dimensional velocity normal to the rotor disk plane and is composed of two components

$$\lambda = \lambda_f + \lambda_i , \quad (2.58)$$

where λ_f is the inflow due to the free stream velocity V defined as

$$\lambda_f = \frac{V \sin \alpha_d}{\Omega R} , \quad (2.59)$$

and λ_i is the induced inflow of the rotor.

The nondimensional rotating frame velocity components of the air relative to the rotor blade are u_T , u_R , and u_P and are illustrated in Figure 2-7. The term u_T is the tangential velocity (positive toward the trailing edge), u_R is the radial velocity (positive toward the blade tip), and u_P is the normal velocity (positive up through the disk plane). In forward flight these velocity components are

$$u_T = \bar{r} + \mu \sin \psi , \quad (2.60)$$

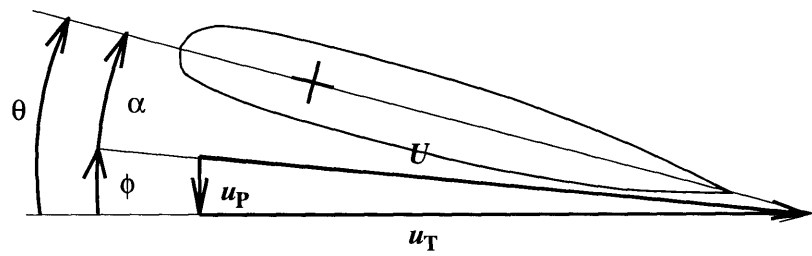
$$u_R = \mu \cos \psi , \quad (2.61)$$

$$u_P = \lambda + (\bar{r} - \bar{e})\dot{\beta} + \mu \beta \cos \psi , \quad (2.62)$$

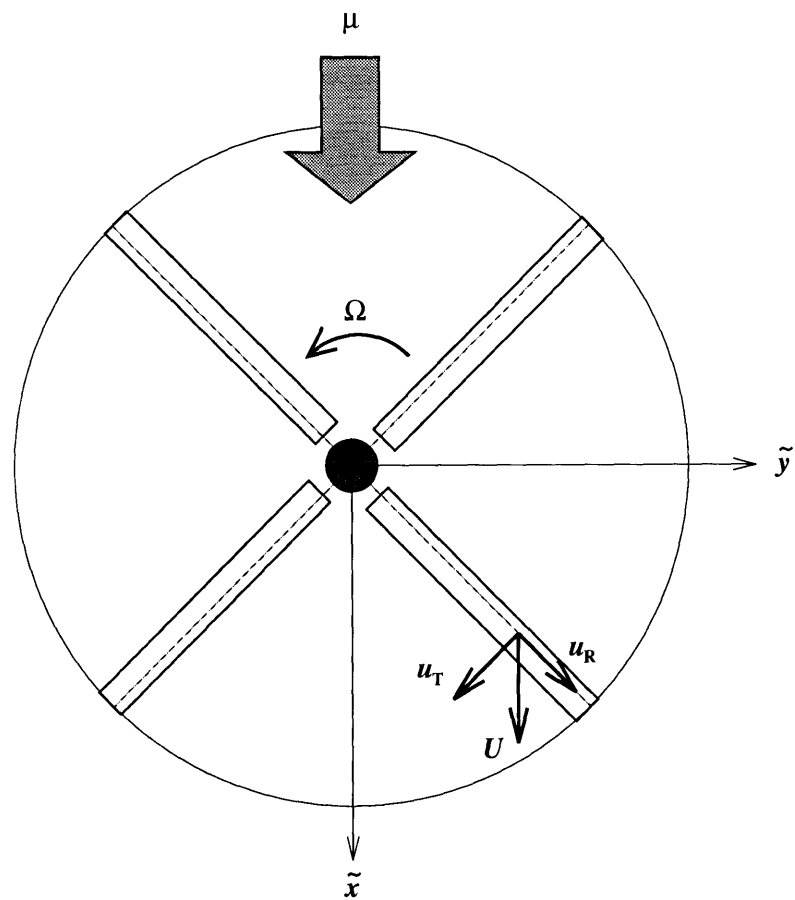
which are functions of the rotor blade azimuth ψ .

With the small angle approximations, the sectional vertical force on a blade is equivalent to the aerodynamic lift, which yields

$$F_z \approx \frac{1}{2} \rho c u_T^2 (\Omega R)^2 c_l , \quad (2.63)$$



(a)



(b)

Figure 2-7: Non-dimensional velocity components: (a) sectional view, (b) top view.

$$\approx \frac{1}{2} \rho c u_T^2 (\Omega R)^2 (a\alpha + n\eta) . \quad (2.64)$$

where the sectional lift coefficient, c_l , is approximated by a linear combination of angle of attack α , and servoflap deflection η . The lift curves are assumed to be linear, with the constant slopes a and n . Assuming a symmetric airfoil, the aerodynamic moment coefficient is only dependent on the servo-flap angle, so that

$$N_{\text{aero}} = \frac{1}{2} \rho c^2 u_T^2 (\Omega R)^2 (p\eta) . \quad (2.65)$$

The moment curve is also assumed linear with a constant slope, p . The contribution due to the servoflap is nonzero only from $\bar{r} = \bar{r}_1$ to $\bar{r} = \bar{r}_2$, the spanwise extent of the servoflap. It is evident from these assumptions that any *linear* aerodynamic actuator can be included in the rotor model.

Since the effectiveness of a trailing edge flap can be significantly reduced by the airfoil's boundary layer, airfoil lift, moment, and drag coefficients were obtained using the 2-dimensional panel code XFOIL [9] which includes the effects of viscosity and compressibility. If the hub loads of interest were in-plane forces, drag effects could be included. These coefficients are generally a complex function of angle of attack, Reynold's number, and Mach number. For this work, a NACA-0012 airfoil at a characteristic design point speed at the 75% radial station was evaluated by XFOIL to determine a , n , and p .

Due to three-dimensional flow effects, blade loading must drop to zero over a finite distance near the blade tips, resulting in so-called *tip loss* [19, pg. 59]. A simple way to approximate the tip loss is to assume that the blade elements outboard of the radial station $\bar{r} = B$ produce no lift. Typical values for B range from 0.96 to 0.98. In general, aerodynamic spanwise integrals will be evaluated from the root cutout, \bar{r}_c , to B .

The total flapping moment M_F is obtained by integrating the sectional lift F_z over

the moment arm ($r - e$). Normalizing M_F by $I_b\Omega^2$ gives

$$\bar{M}_F = \gamma \int_{\bar{r}_c}^B \frac{1}{2}(\bar{r} - \bar{e})u_T^2 \alpha d\bar{r} + \gamma \int_{\bar{r}_1}^{\bar{r}_2} \frac{1}{2}\bar{n}(\bar{r} - \bar{e})u_T^2 \eta d\bar{r}. \quad (2.66)$$

The angle of attack in equation (2.66) can be expanded to give

$$\alpha(\bar{r}) = \theta_r + \sum_k \xi_{\theta_k}(\bar{r})\theta_k - \frac{u_p}{u_T} \quad (2.67)$$

$$= \theta_r + \sum_k \xi_{\theta_k}(\bar{r})\theta_k - \frac{1}{u_T} (\lambda + \mu\beta \cos \psi + (\bar{r} - \bar{e})\dot{\beta}). \quad (2.68)$$

Note that pitch, flapping, and downwash affect the apparent angle of attack of the blade, and therefore the lift. The nondimensional flapping moment has contributions due to the servoflap deflection and each variation in angle of attack, so that

$$\bar{M}_F = \bar{M}_{\theta_r} + \bar{M}_{\theta_k} + \bar{M}_\lambda + \bar{M}_\beta + \bar{M}_{\dot{\beta}} + \bar{M}_\eta. \quad (2.69)$$

The angle of attack expansion of Equation (2.68) may be substituted into the flapping moment Equation (2.66), producing the flapping moment components

$$\bar{M}_{\theta_r} = \gamma \int_{\bar{r}_c}^B \frac{1}{2}(\bar{r} - \bar{e})u_T^2 d\bar{r} \theta_r, \quad (2.70)$$

$$\bar{M}_{\theta_k} = \gamma \int_{\bar{r}_c}^B \frac{1}{2}(\bar{r} - \bar{e})\xi_{\theta_k}(\bar{r})u_T^2 d\bar{r} \theta_k, \quad (2.71)$$

$$\bar{M}_\lambda = -\gamma \int_{\bar{r}_c}^B \frac{1}{2}(\bar{r} - \bar{e})u_T \lambda(\bar{r}) d\bar{r}, \quad (2.72)$$

$$\bar{M}_\beta = -\gamma \int_{\bar{r}_c}^B \frac{1}{2}(\bar{r} - \bar{e})\xi'_\beta(\bar{r})u_T (\mu \cos \psi) d\bar{r} \beta, \quad (2.73)$$

$$\bar{M}_{\dot{\beta}} = -\gamma \int_{\bar{r}_c}^B \frac{1}{2}(\bar{r} - \bar{e})\xi_\beta(\bar{r})u_T d\bar{r} \dot{\beta}, \quad (2.74)$$

$$\bar{M}_\eta = \gamma \int_{\bar{r}_1}^{\bar{r}_2} \frac{1}{2}(\bar{r} - \bar{e})\bar{n}u_T^2 d\bar{r} \eta, \quad (2.75)$$

where $\xi_\beta(\bar{r})$ represents the flapping mode shape and $\xi'_\beta(\bar{r})$ is its derivative with respect to \bar{r} . In this derivation, $\xi_\beta(\bar{r}) = (\bar{r} - \bar{e})$ and $\xi'_\beta(\bar{r}) = 1$ for rigid flapping. Inserting the linear inflow approximation of Equation (2.88), the tangential velocity expression of Equation (2.60), and the rotor integrals of Appendix A, the flapping moment

components can be rewritten as

$$\overline{M}_{\theta_r} = \frac{\gamma}{2} [J^2 + 2\mu J^1 \sin \psi + \mu^2 J^0 \sin^2 \psi] \theta_r , \quad (2.76)$$

$$\overline{M}_{\theta_k} = \frac{\gamma}{2} [M_k^2 + 2\mu M_k^1 \sin \psi + \mu^2 M_k^0 \sin^2 \psi] \theta_k , \quad (2.77)$$

$$\begin{aligned} \overline{M}_\lambda &= -\frac{\gamma}{2} [J^1 + \mu J^0 \sin \psi] \lambda_0 \\ &\quad - \frac{\gamma}{2} [J^2 + \mu J^1 \sin \psi] (\lambda_c \cos \psi + \lambda_s \sin \psi) , \end{aligned} \quad (2.78)$$

$$\overline{M}_\beta = -\frac{\gamma}{2} [\mu L^1 \cos \psi + \mu^2 L^0 \cos \psi \sin \psi] \beta , \quad (2.79)$$

$$\overline{M}_{\dot{\beta}} = -\frac{\gamma}{2} [K^1 + \mu K^0 \sin \psi] \dot{\beta} , \quad (2.80)$$

$$\overline{M}_\eta = \frac{\gamma}{2} [\bar{n} B^2 + 2\bar{n} \mu B^1 \sin \psi + \bar{n} \mu^2 B^0 \sin^2 \psi] \eta . \quad (2.81)$$

The generalized torsional moment due to aerodynamics is calculated by integrating N_{aero} over the torsional mode shape. Normalizing again by $I_b \Omega^2$, the moment \overline{N}_k corresponding to the torsional mode k has two components, so that

$$\overline{N}_k = \overline{N}_{\eta k} + \overline{N}_{\dot{\theta} k} , \quad (2.82)$$

where $\overline{N}_{\eta k}$ is the moment due to servoflap deflection, and $\overline{N}_{\dot{\theta} k}$ is aerodynamic damping. Deflecting the servoflap produces a moment about the rotor blade

$$\overline{N}_{\eta k} = \gamma \int_{\bar{r}_1}^{\bar{r}_2} \frac{1}{2} \bar{p} \bar{c} \xi_{\theta_k}(\bar{r}) u_T^2 d\bar{r} \eta . \quad (2.83)$$

Aerodynamic forces are primarily responsible for damping the torsional motion of the rotor blade, and tend to dominate structural damping. Assuming quasi-steady aerodynamics and an elastic axis coincident with the aerodynamic center, the equations of motion for the torsional dynamics will include a damping term [6, pg. 279] of the form

$$\overline{N}_{\dot{\theta} k} = -\gamma \int_{\bar{r}_c}^B \frac{\bar{c}^2}{16} \xi_{\theta_k}^2(\bar{r}) u_T d\bar{r} \dot{\theta}_k . \quad (2.84)$$

Substituting the tangential velocity expression of Equation (2.60) into Equations (2.83) and (2.84), the moments can be expressed in terms of the rotor integrals of

Appendix A as

$$\bar{N}_{\eta k} = \frac{\gamma \bar{p} \bar{c}}{2} [C_k^2 + 2\mu C_k^1 \sin \psi + \mu^2 C_k^0 \sin^2 \psi] \eta , \quad (2.85)$$

$$\bar{N}_{\dot{\theta} k} = -\frac{\gamma \bar{c}^2}{16} [H_k^1 + \mu H_k^0 \sin \psi] \dot{\theta}_k . \quad (2.86)$$

Collecting both the \bar{N}_k and \bar{M}_F terms and transforming them to MBC, the coupled twist/flapping forcing may be expressed as the vector

$$\begin{Bmatrix} \bar{N}_k \\ \bar{M}_F \end{Bmatrix} = \begin{bmatrix} \Lambda_{\theta_k \theta_k} & \mathbf{0} \\ \Lambda_{\beta \theta_k} & \Lambda_{\beta \beta} \end{bmatrix} \begin{Bmatrix} \theta_k \\ \beta \end{Bmatrix} + \begin{bmatrix} \Lambda_{\theta_k \dot{\theta}_k} & \mathbf{0} \\ \mathbf{0} & \Lambda_{\dot{\beta} \dot{\beta}} \end{bmatrix} \begin{Bmatrix} \dot{\theta}_k \\ \dot{\beta} \end{Bmatrix} + \begin{bmatrix} \mathbf{0} \\ \Lambda_{\beta \theta_r} \end{bmatrix} \{\theta_r\} \\ + \begin{bmatrix} \mathbf{0} \\ \Lambda_{\beta \lambda} \end{bmatrix} \{\lambda\} + \begin{bmatrix} \Lambda_{\theta_k \eta} \\ \Lambda_{\beta \eta} \end{bmatrix} \{\eta\} . \quad (2.87)$$

The Λ matrices are given in Appendix B.

2.5 Inflow Dynamics

For a fixed wing, the unsteady aerodynamics due to the shed wake is classically modelled using Theodorsen's shed wake function. For a helicopter rotor in forward flight, the wake structure is much more complicated. The rotating airfoils produce shed and trailing vorticity, creating a skewed helical wake which influences the induced flow at the rotor disk. While the analysis of rotor wake structure is an important research topic, it is beyond the scope of this work, whose objective is to define a linear rotor model. Although non-linear lift deficiency functions were not included, a simple model for the induced inflow was incorporated, since this significantly affects rotor hub loads. Perturbations in the induced inflow will appear in the rotor blade airloads as a perturbation in the sectional angle of attack. Induced inflow is generally a complicated function of radius and azimuth, but a linear approximation can provide adequate results [19], [34], [35]. The linear inflow approximation

$$\lambda = \lambda_0 + \lambda_c \bar{r} \cos \psi + \lambda_s \bar{r} \sin \psi , \quad (2.88)$$

was used for the purpose of this research with simple dynamics developed by Pitt and Peters [35]. These dynamics are based on actuator disk theory and relate perturbations in λ to changes in the *aerodynamic* hub load coefficients, C_T , C_M , and C_L . While the total hub loads may be balanced by inertial effects, the aerodynamic components of those loads still affect the induced air flow encountered by the rotor. Defining the vectors

$$\mathbf{y}_{\text{aero}} = \begin{Bmatrix} C_T \\ C_M \\ C_L \end{Bmatrix}_{\text{aero}}, \quad \boldsymbol{\lambda} = \begin{Bmatrix} \lambda_0 \\ \lambda_c \\ \lambda_s \end{Bmatrix}, \quad (2.89)$$

the inflow dynamics are presented in the following form,

$$\dot{\boldsymbol{\lambda}} = -\mathbf{M}^{-1}\mathbf{L}^{-1}\boldsymbol{\lambda} + \mathbf{M}^{-1}\mathbf{y}_{\text{aero}}, . \quad (2.90)$$

which can easily be incorporated into the state space model. The inflow dynamics matrices are presented in Appendix C.

2.6 Hub Reactions

In the rotating frame, the forces and moments on individual blades are the vertical shear force, S , defined positive up along the z axis and the flapping hinge moment, M_β , defined positive about the x axis. The nose up torsional moment along the blade is negligible compared to the flapping moment and will not be included in the hub load calculation. In the non-rotating frame, the non-dimensional hub reactions of interest are C_T , C_M , and C_L , the thrust, pitch moment, and roll moment coefficients respectively. The thrust force is defined as positive in the \tilde{z} direction, the roll moment is positive about the \tilde{x} axis, and the pitch moment is positive about the \tilde{y} axis. In this section, the rotating blade loads will be transformed to the fixed frame hub loads using MBC. The total hub loads have components due to aerodynamic and inertial

forcing terms, so that

$$\begin{Bmatrix} C_T \\ C_M \\ C_L \end{Bmatrix} = \begin{Bmatrix} C_T \\ C_M \\ C_L \end{Bmatrix}_{\text{aero}} + \begin{Bmatrix} C_T \\ C_M \\ C_L \end{Bmatrix}_{\text{inertial}} . \quad (2.91)$$

The aerodynamic components will be needed to force the inflow dynamics.

The vertical shear force at the blade root, S , is the integral of the vertical force acting along the blade, where the vertical force is composed of the section aerodynamic lift acting upward and the section inertia force acting downward. The resultant force is normalized by $\rho A(\Omega R)^2$, so that $\bar{S} = S/\rho A(\Omega R)^2$. The normalized shear force may be written as

$$\begin{aligned} \bar{S} = & \frac{\sigma a}{N} \int_{\bar{r}_c}^R \frac{1}{2} u_T^2 \alpha \, d\bar{r} + \frac{\sigma a}{N} \int_{\bar{r}_1}^{\bar{r}_2} \frac{1}{2} \bar{n} u_T^2 \eta \, d\bar{r} - \frac{\sigma a}{N \gamma I_b} \int_e^R m(r - e) \ddot{\beta} \, dr \\ & + \frac{\sigma a}{N \gamma I_b} \int_e^R m x_{cg} \ddot{\theta}_r \, dr + \frac{\sigma a}{N \gamma I_b} \int_e^R m x_{cg} \xi_{\theta_k}(r) \ddot{\theta}_k \, dr . \end{aligned} \quad (2.92)$$

The shear force has components due to the sectional angle of attack defined in Equation (2.68), as well as the servoflap angle. The last three terms are inertial forces. The vertical shear force may be rewritten as

$$\bar{S} = \bar{S}_{\theta_r} + \bar{S}_{\theta_k} + \bar{S}_\lambda + \bar{S}_\beta + \bar{S}_{\dot{\beta}} + \bar{S}_\eta + \bar{S}_{\ddot{\theta}_r} + \bar{S}_{\ddot{\theta}_k} . \quad (2.93)$$

These forces may be rewritten in terms of the integrals of Appendix A as

$$\bar{S}_{\theta_r} = \frac{\sigma a}{2N} [D^2 + 2\mu D^1 \sin \psi + \mu^2 D^0 \sin^2 \psi] \theta_r , \quad (2.94)$$

$$\bar{S}_{\theta_k} = \frac{\sigma a}{2N} [G_k^2 + 2\mu G_k^1 \sin \psi + \mu^2 G_k^0 \sin^2 \psi] \theta_k , \quad (2.95)$$

$$\begin{aligned} \bar{S}_\lambda = & -\frac{\sigma a}{2N} [D^1 + \mu D^0 \sin \psi] \lambda_0 \\ & - \frac{\sigma a}{2N} [D^2 + \mu D^1 \sin \psi] (\lambda_c \cos \psi + \lambda_s \sin \psi) , \end{aligned} \quad (2.96)$$

$$\bar{S}_\beta = -\frac{\sigma a}{2N} [\mu F^1 \cos \psi + \mu^2 F^0 \cos \psi \sin \psi] \beta , \quad (2.97)$$

$$\bar{S}_{\dot{\beta}} = -\frac{\sigma a}{2N} [E^1 + \mu E^0 \sin \psi] \dot{\beta} , \quad (2.98)$$

$$\bar{S}_\eta = \frac{\sigma a}{2N} [\bar{n} A^2 + 2\bar{n} \mu A^1 \sin \psi + \bar{n} \mu^2 A^0 \sin^2 \psi] \eta , \quad (2.99)$$

$$\bar{S}_{\tilde{\beta}} = -\frac{\sigma a}{N\gamma} m_{\tilde{\beta}}^* \ddot{\beta}, \quad (2.100)$$

$$\bar{S}_{\tilde{\theta}_r} = \frac{\sigma a}{N\gamma} m_{\tilde{\theta}_r}^* \ddot{\theta}_r, \quad (2.101)$$

$$\bar{S}_{\tilde{\theta}_k} = \frac{\sigma a}{N\gamma} m_{\tilde{\theta}_k}^* \ddot{\theta}_k. \quad (2.102)$$

Summing over N blades, the rotor thrust coefficient is given by

$$C_T = \sum_{q=1}^N (\bar{S}_{\theta_r} + \bar{S}_{\theta_k} + \bar{S}_\lambda + \bar{S}_\beta + \bar{S}_{\dot{\beta}} + \bar{S}_\eta + \bar{S}_{\tilde{\beta}} + \bar{S}_{\tilde{\theta}_r} + \bar{S}_{\tilde{\theta}_k}). \quad (2.103)$$

which is equivalent to the MBC collective summation operator. M_β is simply the moment due to the flap hinge spring ($K_\beta \beta$). The non-dimensional moment due to the q th blade is

$$C_{M_q} = \frac{M_\beta + e S}{\rho A R (\Omega R)^2} \quad (2.104)$$

or

$$C_{M_q} = \frac{\sigma a}{N\gamma} (\bar{\omega}_\beta^2 I_\beta^*) \beta + \bar{e} (\bar{S}_{\theta_r} + \bar{S}_{\theta_k} + \bar{S}_\lambda + \bar{S}_\beta + \bar{S}_{\dot{\beta}} + \bar{S}_\eta + \bar{S}_{\tilde{\beta}} + \bar{S}_{\tilde{\theta}_r} + \bar{S}_{\tilde{\theta}_k}). \quad (2.105)$$

If the contributions of each blade are summed, then the pitch and roll coefficients are

$$C_M = \sum_{q=1}^N (-C_{M_q} \cos \psi_q) \quad (2.106)$$

and

$$C_L = \sum_{q=1}^N (C_{M_q} \sin \psi_q) \quad (2.107)$$

which are similar in form to the MBC cyclic summation operators. Including only the aerodynamic terms, the hub reactions are

$$\begin{aligned} \left\{ \begin{array}{c} C_T \\ C_M \\ C_L \end{array} \right\}_{\text{aero}} &= \left[\begin{array}{cc} \Gamma_{\theta_k} & \Gamma_\beta \end{array} \right] \left\{ \begin{array}{c} \theta_k \\ \beta \end{array} \right\} + \left[\begin{array}{cc} \mathbf{0} & \Gamma_{\dot{\beta}} \end{array} \right] \left\{ \begin{array}{c} \dot{\theta}_k \\ \dot{\beta} \end{array} \right\} \\ &\quad + [\Gamma_{\theta_r}] \{\theta_r\} + [\Gamma_\lambda] \{\lambda\} + [\Gamma_\eta] \{\eta\}. \end{aligned} \quad (2.108)$$

The Γ matrices are defined in Appendix B. The total thrust, pitch moment, and roll moment coefficients are obtained by simply adding the inertial terms, represented by the Φ matrices, also defined in Appendix B. Therefore,

$$\begin{aligned} \begin{Bmatrix} C_T \\ C_M \\ C_L \end{Bmatrix} &= \left[(\Gamma_{\theta_k} + \Phi_{\theta_k}) \quad (\Gamma_\beta + \Phi_\beta) \right] \begin{Bmatrix} \theta_k \\ \beta \end{Bmatrix} + \left[\Phi_{\dot{\theta}_k} \quad (\Gamma_{\dot{\beta}} + \Phi_{\dot{\beta}}) \right] \begin{Bmatrix} \dot{\theta}_k \\ \dot{\beta} \end{Bmatrix} \\ &\quad + \left[\Phi_{\ddot{\theta}_k} \quad \Phi_{\ddot{\beta}} \right] \begin{Bmatrix} \ddot{\theta}_k \\ \ddot{\beta} \end{Bmatrix} + \left[(\Gamma_{\theta_r} + \Phi_{\theta_r}) \right] \{\theta_r\} + \left[\Phi_{\dot{\theta}_r} \right] \{\dot{\theta}_r\} + \left[\Phi_{\ddot{\theta}_r} \right] \{\ddot{\theta}_r\} \\ &\quad + [\Gamma_\lambda] \{\lambda\} + [\Gamma_\eta] \{\eta\}. \end{aligned} \quad (2.109)$$

2.7 State Space Model

With the dynamics and hub reactions defined in MBC matrix form, an LTI state space representation of a rotor with blade-mounted servo-flaps can be presented:

$$\dot{x} = Ax + Bu + B_\lambda y_{\text{aero}}, \quad (2.110)$$

$$y_{\text{aero}} = C_{\text{aero}}x + D_{\text{aero}}u, \quad (2.111)$$

$$y = Cy + Du. \quad (2.112)$$

For convenience, the vector

$$z = \begin{Bmatrix} \theta_k \\ \beta \end{Bmatrix} \quad (2.113)$$

is defined to represent the coupled elastic pitch/flap coordinates. The state and control vectors, x and u , are defined as

$$x = \begin{Bmatrix} \theta_r \\ \dot{\theta}_r \\ z \\ \dot{z} \\ \lambda \end{Bmatrix}, \quad u = \begin{Bmatrix} \ddot{\theta}_r \\ \eta \end{Bmatrix}. \quad (2.114)$$

The output vectors, \mathbf{y}_{aero} and \mathbf{y} , are defined as

$$\mathbf{y}_{\text{aero}} = \begin{Bmatrix} C_T \\ C_M \\ C_L \end{Bmatrix}_{\text{aero}}, \quad \mathbf{y} = \begin{Bmatrix} C_T \\ C_M \\ C_L \end{Bmatrix}. \quad (2.115)$$

Therefore, the state space matrices are

$$\mathbf{A} = \begin{bmatrix} \mathbf{0} & \mathbf{I} & \mathbf{0} & \mathbf{0} & \mathbf{0} \\ \mathbf{0} & \mathbf{0} & \mathbf{0} & \mathbf{0} & \mathbf{0} \\ \mathbf{0} & \mathbf{0} & \mathbf{0} & \mathbf{I} & \mathbf{0} \\ \Delta_{\tilde{z}}^{-1}(\Psi_{z\theta_r} + \Lambda_{z\theta_r}) & \Delta_{\tilde{z}}^{-1}\Psi_{z\dot{\theta}_r} & \Delta_{\tilde{z}}^{-1}(\Lambda_{zz} - \Delta_z) & \Delta_{\tilde{z}}^{-1}(\Lambda_{z\dot{z}} - \Delta_{\dot{z}}) & \Delta_{\tilde{z}}^{-1}\Lambda_{z\lambda} \\ \mathbf{0} & \mathbf{0} & \mathbf{0} & \mathbf{0} & -\mathbf{M}^{-1}\mathbf{L}^{-1} \end{bmatrix} \quad (2.116)$$

$$\mathbf{B} = \begin{bmatrix} \mathbf{0} & \mathbf{0} \\ \mathbf{I} & \mathbf{0} \\ \mathbf{0} & \mathbf{0} \\ \Delta_{\tilde{z}}^{-1}\Psi_{z\ddot{\theta}_r} & \Delta_{\tilde{z}}^{-1}\Lambda_{z\eta} \\ \mathbf{0} & \mathbf{0} \end{bmatrix} \quad (2.117)$$

$$\mathbf{B}_\lambda = \begin{bmatrix} \mathbf{0} \\ \mathbf{0} \\ \mathbf{0} \\ \mathbf{0} \\ \mathbf{M}^{-1} \end{bmatrix} \quad (2.118)$$

$$\mathbf{C}_{\text{aero}} = [\Gamma_{\theta_r} \ \mathbf{0} \ \Gamma_z \ \Gamma_{\dot{z}} \ \Gamma_\lambda] \quad (2.119)$$

$$\mathbf{D}_{\text{aero}} = [\mathbf{0} \ \Gamma_\eta] \quad (2.120)$$

$$\begin{aligned} \mathbf{C} = & [(\Gamma_{\theta_r} + \Phi_{\theta_r}) \ \Phi_{\dot{\theta}_r} \ (\Gamma_z + \Phi_z) \ (\Gamma_{\dot{z}} + \Phi_{\dot{z}}) \ \Gamma_\lambda] \\ & + \Phi_{\tilde{z}} [\Delta_{\tilde{z}}^{-1}(\Psi_{z\theta_r} + \Lambda_{z\theta_r}) \ \Delta_{\tilde{z}}^{-1}\Psi_{z\dot{\theta}_r} \ \Delta_{\tilde{z}}^{-1}(\Lambda_{zz} - \Delta_z) \ \Delta_{\tilde{z}}^{-1}(\Lambda_{z\dot{z}} - \Delta_{\dot{z}}) \ \Delta_{\tilde{z}}^{-1}\Lambda_{z\lambda}] \end{aligned} \quad (2.121)$$

$$\mathbf{D} = [\Phi_{\ddot{\theta}_r} \ \Gamma_\eta] + \Phi_{\tilde{z}} [\Delta_{\tilde{z}}^{-1}\Psi_{z\ddot{\theta}_r} \ \Delta_{\tilde{z}}^{-1}\Lambda_{z\eta}] \quad (2.122)$$

The rotor loads \mathbf{y}_{aero} serve as inputs to the λ dynamics. Closing the dynamic inflow loop yields the state space model

$$\dot{\mathbf{x}} = (\mathbf{A} + \mathbf{B}_\lambda \mathbf{C}_{\text{aero}})\mathbf{x} + (\mathbf{B} + \mathbf{B}_\lambda \mathbf{D}_{\text{aero}})\mathbf{u} , \quad (2.123)$$

$$\mathbf{y} = \mathbf{C}\mathbf{x} + \mathbf{D}\mathbf{u} , \quad (2.124)$$

or,

$$\dot{\mathbf{x}} = \tilde{\mathbf{A}}\mathbf{x} + \tilde{\mathbf{B}}\mathbf{u} , \quad (2.125)$$

$$\mathbf{y} = \mathbf{C}\mathbf{x} + \mathbf{D}\mathbf{u} . \quad (2.126)$$

The complete state space rotor model is presented in Tables 2.1 and 2.2. The state space rotor model was coded in Matlab and run on a DEC-5000/25 workstation. A listing of the code and an explanation of the subroutines is provided in Appendix D.

Table 2.1: State space equation for the rotor system dynamics.

$$\begin{aligned} \begin{Bmatrix} \dot{\theta}_r \\ \ddot{\theta}_r \\ \dot{z} \\ \ddot{z} \\ \lambda \end{Bmatrix} &= \begin{bmatrix} 0 & I & 0 & 0 & 0 \\ 0 & 0 & 0 & 0 & 0 \\ 0 & 0 & I & 0 & 0 \\ \Delta_{\bar{z}}^{-1}(\Psi_{z\theta_r} + \Lambda_{z\theta_r}) & \Delta_{\bar{z}}^{-1}\Psi_{z\dot{\theta}_r} & \Delta_{\bar{z}}^{-1}(\Lambda_{zz} - \Delta_z) & \Delta_{\bar{z}}^{-1}(\Lambda_{z\dot{z}} - \Delta_{\dot{z}}) & \Delta_{\bar{z}}^{-1}\Lambda_{z\lambda} \\ M^{-1}\Gamma_{\theta_r} & M^{-1}\Gamma_z & M^{-1}\Gamma_z & M^{-1}\Gamma_z & M^{-1}(\Gamma_\lambda - L^{-1}) \end{bmatrix} \begin{Bmatrix} \theta_r \\ \dot{\theta}_r \\ z \\ \dot{z} \\ \lambda \end{Bmatrix} \\ &+ \begin{bmatrix} 0 & 0 & 0 \\ I & 0 & 0 \\ 0 & 0 & 0 \\ \Delta_{\bar{z}}^{-1}\Psi_{z\ddot{\theta}_r} & \Delta_{\bar{z}}^{-1}\Lambda_{z\eta} \\ 0 & M^{-1}\Gamma_\eta \end{bmatrix} \begin{Bmatrix} \ddot{\theta}_r \\ \eta \end{Bmatrix} \end{aligned}$$

Table 2.2: State space equation for the hub loads.

$$\begin{aligned} \left\{ \begin{array}{c} C_T \\ C_M \\ C_L \end{array} \right\} &= \left[\begin{bmatrix} (\Gamma_{\theta_r} + \Phi_{\theta_r}) & \Phi_{\dot{\theta}_r} & (\Gamma_z + \Phi_z) & (\Gamma_z + \Phi_z) & \Gamma_\lambda \end{bmatrix} + \Phi_z \Delta_z^{-1} \left[\begin{bmatrix} (\Psi_{z\theta_r} + \Lambda_{z\theta_r}) & \Psi_{z\dot{\theta}_r} & (\Lambda_{zz} - \Delta_z) & (\Lambda_{zz} - \Delta_z) & \Lambda_{z\lambda} \end{bmatrix} \right. \right. \\ &\quad \left. \left. + \left[\begin{bmatrix} (\Phi_{\ddot{\theta}_r} + \Phi_z \Delta_z^{-1} \Psi_{z\dot{\theta}_r}) & (\Gamma_\eta + \Phi_z \Delta_z^{-1} \Lambda_{z\eta}) \end{bmatrix} \right] \right\} \right\} \end{aligned}$$

Chapter 3

State Space Model Results

In the previous chapter, a multi-input multi-output (MIMO) model of a *smart rotor* which utilizes both root-pitch and servo-flap actuation was presented. This model has six control inputs and three outputs, yielding eighteen individual transfer functions. In this chapter, we will investigate the performance capabilities of a smart rotor, concentrating on just two of these transfer functions. In particular, we will present results on the effects of collective root pitch and servoflap actuation on thrust. The collective inputs are chosen because they are the most effective in controlling the thrust response.

In the previous chapter, the rotor state space model was derived with root pitch acceleration, $\ddot{\theta}_r$, as a control input. This was necessary to maintain the state space format, since $\ddot{\theta}_r$ is a forcing term for the torsional dynamics. However, in practice it is the root pitch position, θ_r , that is actuated. Therefore, the transfer functions of interest are $(C_T/\sigma)/\theta_{r0}$ and $(C_T/\sigma)/\eta_0$, which will be referred to as $G_{\theta_{r0}}(\bar{s})$ and $G_{\eta_0}(\bar{s})$ respectively, where \bar{s} is the normalized Laplace variable, s/Ω . $G_{\theta_{r0}}(\bar{s})$ is obtained from the state space model by integrating the control input, $\ddot{\theta}_{r0}$, so that

$$G_{\theta_{r0}}(\bar{s}) = \bar{s}^2 \frac{C_T/\sigma}{\ddot{\theta}_{r0}} = \frac{C_T/\sigma}{\theta_{r0}} . \quad (3.1)$$

To validate the state space model, the rotor analysis program C60 obtained from Boeing Helicopters was utilized. Using a generic rotor with typical parameters listed

Table 3.1: Baseline parameters of generic and H-34 rotors.

Parameters	Generic Rotor	H-34 Rotor
N	4	4
\bar{c}	0.0800	0.0488
σ	0.1019	0.0621
\bar{e}	0.0500	0.0357
\bar{r}_c	0.0500	0.2100
\bar{r}_1	0.6500	0.6000
\bar{r}_2	0.8500	0.8000
a	5.73	6.30
n	3.84	3.13
p	-0.688	-0.513
I_{β}^*	8.5740×10^{-1}	8.9263×10^{-1}
$\bar{\nu}_{\beta}$	1.04	1.03
$I_{\theta_1}^*$	3.2035×10^{-4}	1.3386×10^{-4}
$\bar{\omega}_1$	4.50	7.65
γ	8.00	8.11

in Table 3.1, continuous frequency responses produced by the state space model were compared to the rotor response at discrete frequency points obtained from C60. Using the H-34 rotor as a baseline configuration, parametric studies involving various rotor parameters were performed. Baseline H-34 parameters are also listed in Table 3.1. In addition to parametric studies, the implementation of a servo-flap actuation scheme in a HHC system will be discussed. The state space model was coded in Matlab and run on a DEC-5000/25 workstation. The C60 runs were performed on a SUN SPARCstation.

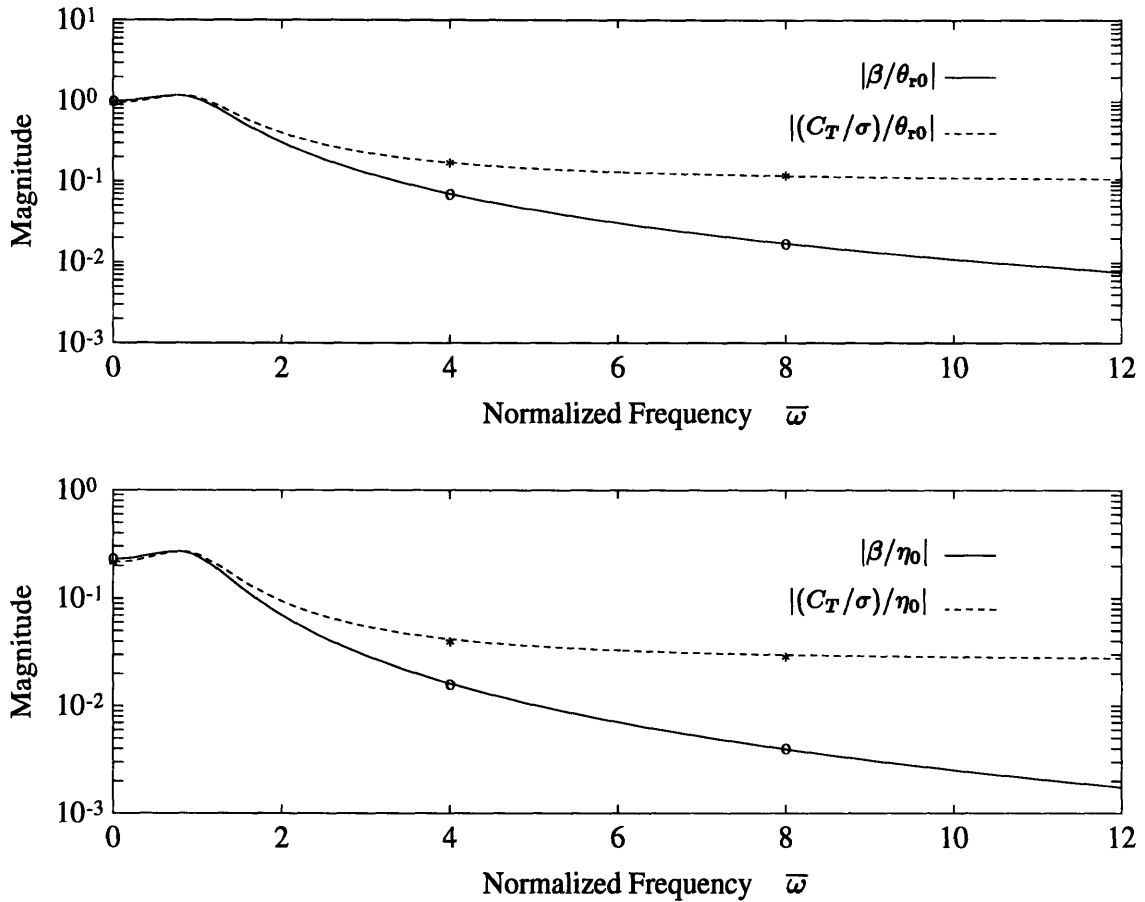


Figure 3-1: Continuous frequency response from state space model and C60 validation points at $\bar{\omega} = 0, 4$, and 8 . Rigid flapping only case.

3.1 Model validation using C60

C60 is a comprehensive aeroelastic rotor analysis program which has been in continuous development by Boeing Helicopters since the late 1960's. The C60 program has been used in the development of numerous helicopters including various Chinook CH47 models, the Comanche RAH-66, and others. It has also been used as an analytical tool in a number of research projects [51], [50]. One of the latest revisions to this program is the addition of incremental aerodynamic coefficients to simulate the behavior of a trailing edge servo-flap.

C60 was used to obtain the rotor response due to root pitch and servo-flap actuation of a generic four-bladed rotor. Due to time and computation constraints, simulations were performed at hover with linear aerodynamics and *without* aerody-

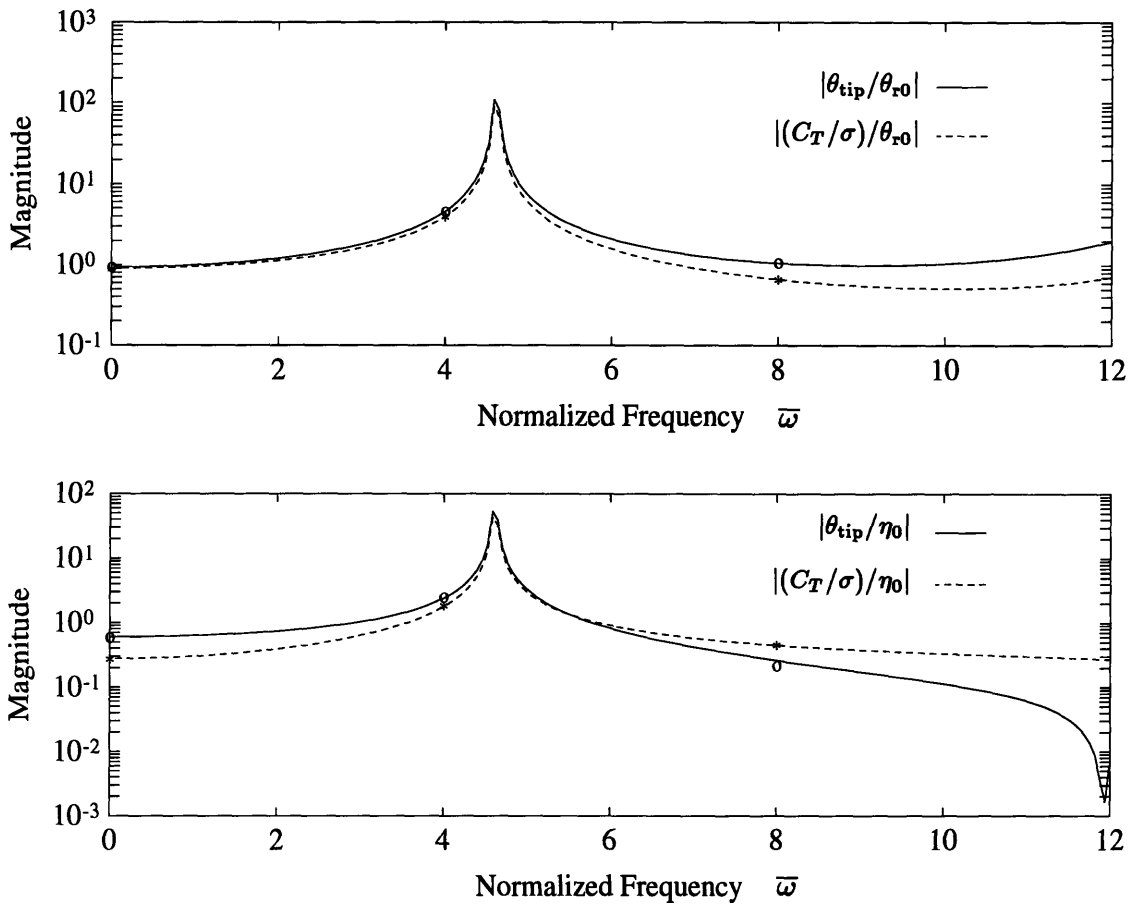


Figure 3-2: Continuous frequency response from state space model and C60 validation points at $\bar{\omega} = 0, 4$, and 8 . Elastic torsion only case.

namic torsional damping or inflow. The inputs to the rotor were collective root pitch, θ_{r0} , and servo-flap commands, η_0 . Outputs of interest were the tip angle, θ_{tip} , flapping angle, β , and the thrust response, \mathcal{C}_T/σ . Responses were obtained by running a baseline case and then exciting the rotor at 0Ω , 4Ω , and 8Ω and evaluating the change in the outputs ($\Delta\theta_{\text{tip}}$, $\Delta\beta$, and $\Delta\mathcal{C}_T/\sigma$) from baseline.

Cases which were run include rigid flapping only (Figure 3-1), elastic torsion only (Figure 3-2), and torsion/flapping coupled by a c.g. offset (Figure 3-3). The rigid flapping only and torsion only cases, which utilized the generic rotor with $\bar{\omega}_1 = 4.50$, were originally presented in [12]. The coupled torsion/flapping case incorporated an \bar{x}_{cg} of 0.0833 along the servo-flap span from $\bar{r} = 6.5$ to 8.5 . Elsewhere, the c.g. was coincident with the pitch axis at the quarter chord. For the coupled case, the torsional stiffness was scaled up to provide a $\bar{\omega}_1$ of 6.00 to help speed up convergence

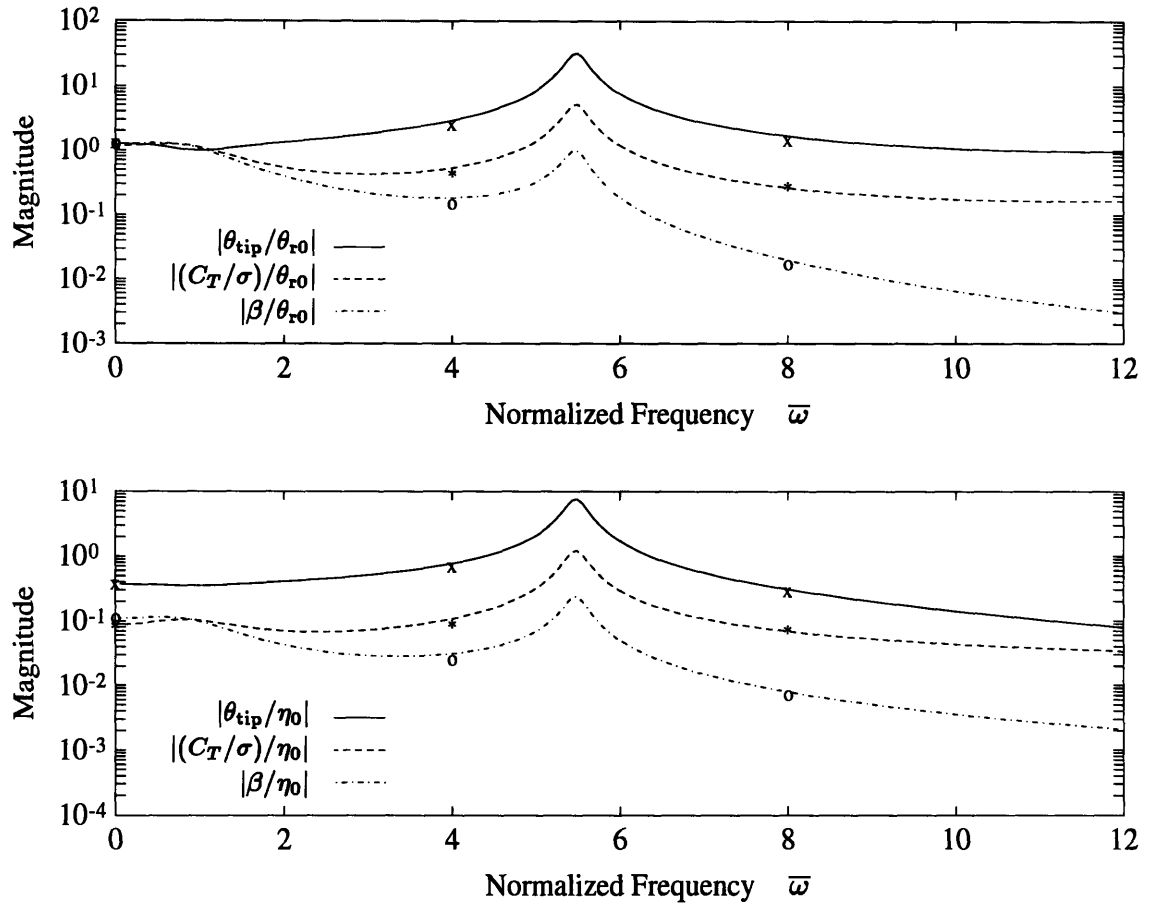


Figure 3-3: Continuous frequency response from state space model and C60 validation points at $\bar{\omega} = 0, 4$, and 8 . Rigid flapping and elastic torsion coupled by c.g. offset.

at 4Ω . Note that in Figure 3-3, the actual resonant peak appears at $\bar{\omega} \approx 5.5$. This is attributed to the coupling of the rigid flapping and first elastic torsional modes by the c.g. offset. In general, there was good agreement between the state space model and C60. In fact, for the flapping only case there was agreement to three significant digits. The coupled case shows satisfactory agreement, but there is still some discrepancy attributed to convergence problems with C60.

For each case presented, the C60 program was run seven times in order to provide information at three discrete frequency points. The C60 runs required approximately 20 minutes of CPU time each. Unfortunately, the time domain simulations provided by C60 could not provide additional information at other frequencies, which was part of the motivation for developing an LTI model. The results presented in this section

provide adequate validation for the state space rotor model. In the following sections, the full state space model will be exercised to determine the performance capabilities of a smart rotor.

3.2 Parametric Studies

Using the state space model, parametric studies involving torsional stiffness, actuator placement, c.g. offset, and additional mass due to the actuator were performed on the H-34 rotor model. The H-34 has been well-documented in a number of wind tunnel and flight tests. In fact, the H-34 was used by Kaman as a baseline rotor in early CTR development. Since the H-34 rotor blade has spanwise-varying properties, a lumped model with 25 mass and stiffness elements was assumed. Results are presented as frequency response plots of $G_{\theta_{r0}}(j\bar{\omega})$ and $G_{\eta_0}(j\bar{\omega})$.

The frequency response format was chosen to investigate various smart rotor applications. Different rotor control concepts can be distinguished by the frequency ranges in which they operate. Possible applications for a servo-flap controlled rotor include automatic blade tracking, maneuvering and trim control, gust disturbance rejection, performance enhancement, stall alleviation, vibration reduction, and acoustic control. Automatic blade tracking can be performed by assigning the appropriate DC offset to each of the servo-flaps. For maneuvering and gust disturbances, the control authority at lower frequencies ($\bar{\omega} \leq 1$) is important. Moving up to higher frequencies, ($1 \leq \bar{\omega} \leq 10$), performance enhancement, vibration reduction, and acoustic control are important issues. Specifically, a mixture of 1Ω , 2Ω , and 3Ω control can be used to increase lift in the fore and aft rotor areas and alleviate retreating blade stall. For HHC systems for vibration reduction, the control effort is centered around $N\Omega$, 4Ω for the H-34 rotor. The predominant vibratory loading and noise disturbance is usually attributed to blade vortex interaction (BVI) at $N\Omega$.

The nominal value of C_T/σ is approximately equivalent to 1 g of thrust, so that $(\Delta C_T/\sigma)/(C_T/\sigma)$ is a measure of control authority in g 's. For these parametric studies, a moderate C_T/σ of 0.1 is used. The nominal C_T is needed to calculate

parameters for the Pitt and Peters inflow model (see Appendix C). For convenience, magnitude plots are presented in 1/deg units to determine the amount of authority per degree of root pitch or servo-flap deflection. For root pitch actuation, various electro-hydraulic actuators can provide from 1 to 3 degrees of rotation at higher harmonic frequencies [49], [30], [40]. For the piezoelectric servo-flap actuator developed by Spangler and Hall [43], deflections of about 5–10 degrees are achievable over a wide bandwidth. Using these standards, the effectiveness of root pitch, servo-flap, or a combination can be investigated.

3.2.1 Torsional Stiffness Study

An obvious parameter of interest in a servo-flap rotor system is the torsional stiffness, represented by $\bar{\omega}_1$, the normalized first torsional frequency. The baseline H-34 rotor blade has a $\bar{\omega}_1$ of 7.65, based on a 25 lumped inertia/stiffness approximation. For the torsional stiffness study, $\bar{\omega}_1$ was varied from 2.50 to 7.65 at both hover and at $\mu = 0.25$.

Figures 3-4 and 3-5 show the thrust response of $G_{\theta_{r0}}(j\bar{\omega})$ and $G_{\eta_0}(j\bar{\omega})$ at hover. Changing the torsional stiffness does not significantly affect the $G_{\theta_{r0}}(j\bar{\omega})$ response except for the shifting of resonant peaks at the high frequency modes (see Figure 3-4). Using root pitch actuation, the rotor blades behave primarily as rigid bodies at $\bar{\omega} \leq 1$, so that a torsionally stiff rotor is desirable. Looking at Figure 3-5, the sensitivity of servo-flap authority to torsional stiffness is much more significant. At low frequencies ($\bar{\omega} \leq 1$), there are orders of magnitude changes in the thrust response due to collective servo-flap actuation. As expected, servo-flap authority increases as torsional stiffness decreases, with the baseline H-34 rotor having the least servo-flap authority. The baseline H-34 rotor is actually very near the aileron reversal point causing this very low response. Aileron reversal is dependent on torsional stiffness as well as other parameters and will be discussed in more detail in Section 3.2.4. Looking at the higher frequency range ($1 \leq \bar{\omega} \leq 10$), the elastic torsional dynamics determine the shape of the $G_{\eta_0}(j\bar{\omega})$ response. For $\bar{\omega}_1 = 2.50$, the $G_{\eta_0}(j\bar{\omega})$ thrust response essentially rolls off after $\bar{\omega}_1 = 1$. For $\bar{\omega}_1 = 4.50$, the thrust response remains fairly

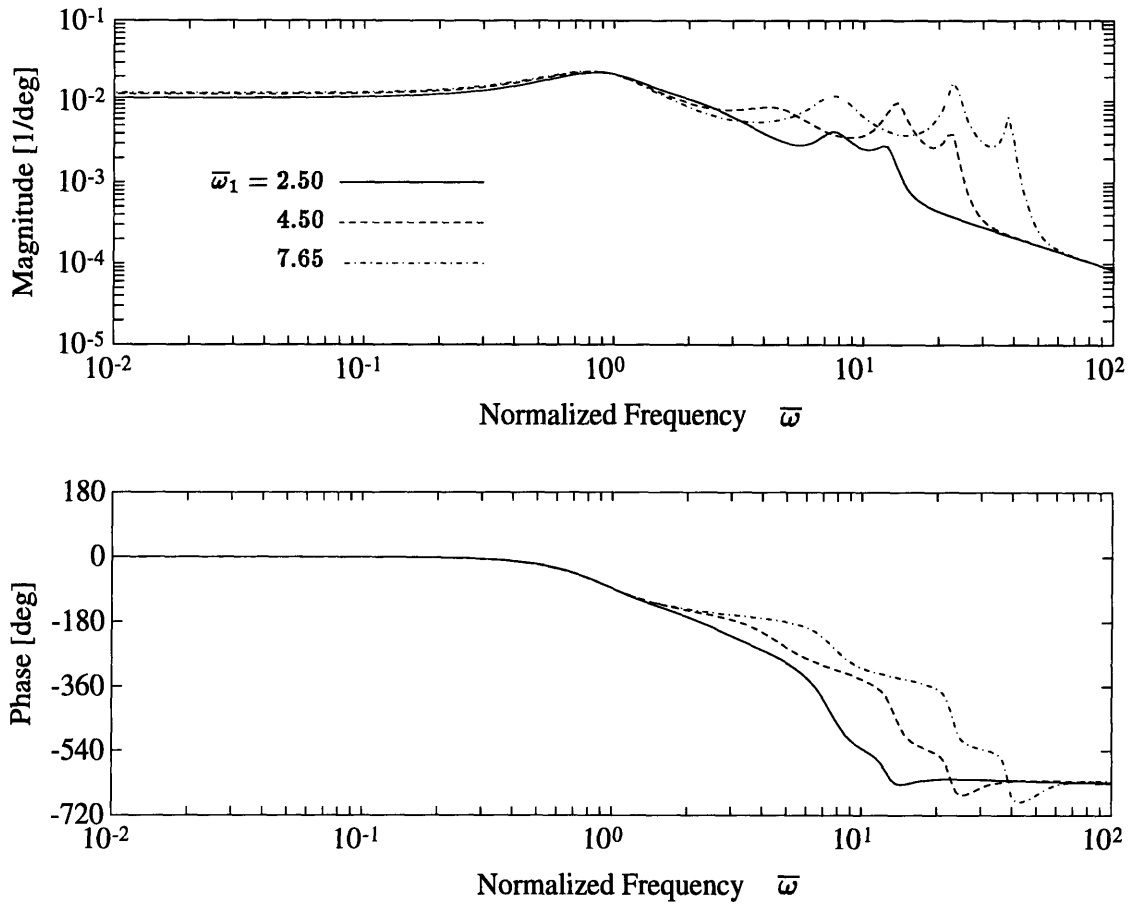


Figure 3-4: The effect of blade torsional stiffness on $G_{\theta_r0}(j\bar{\omega})$ for H-34 rotor in hover.

flat up to $\bar{\omega} = 4.5$ and then begins to roll off. Note that at extremely high frequencies ($\bar{\omega} \gg 10$), the $G_{\eta_0}(j\bar{\omega})$ flattens out, since the η_0 control input is a feedthrough term in the thrust response.

Figures 3-6 and 3-7 show the thrust response of $G_{\theta_r0}(j\bar{\omega})$ and $G_{\eta_0}(j\bar{\omega})$ in edgewise forward flight ($\mu = 0.25$) as $\bar{\omega}_1$ is varied. There is very little change between the $G_{\theta_r0}(j\bar{\omega})$ responses at hover and $\mu = 0.25$. Differences are on the order of $10^{-3}/\text{deg}$. For the $G_{\eta_0}(j\bar{\omega})$ response, the differences due to forward flight are larger (on order of $10^{-2}/\text{deg}$). The higher dynamic pressure associated with forward flight provides the servo-flap with more authority. Looking at the higher frequency region ($(1 \leq \bar{\omega} \leq 10)$) of Figure 3-7, forward flight introduces a dip at $\bar{\omega} \approx 2$ in the η_0 thrust response. This is attributed to the β_s or *lateral tilt mode*. In forward flight, the dynamic pressure on the advancing side of the rotor disk is greater than that on the retreating side,

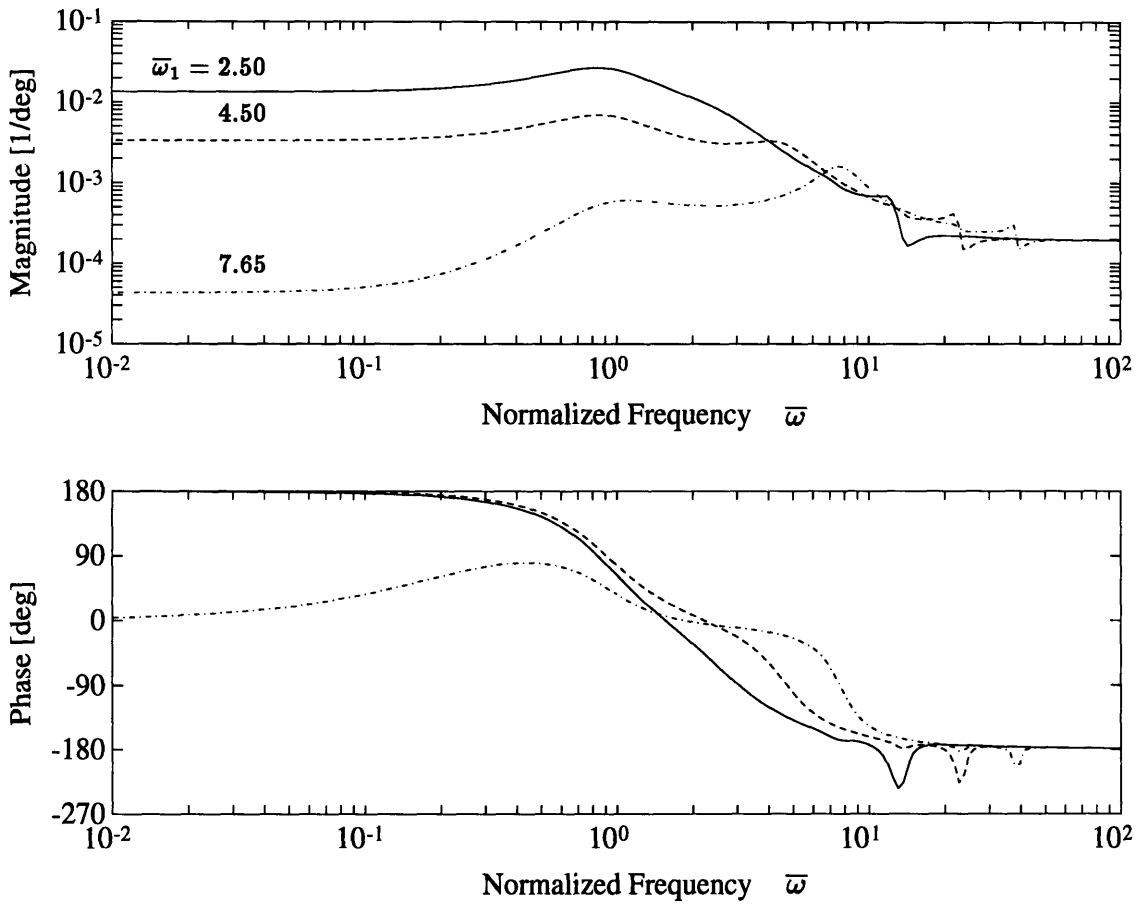


Figure 3-5: The effect of blade torsional stiffness on $G_{\eta_0}(j\bar{\omega})$ for H-34 rotor in hover.

allowing a collective input to influence this cyclic mode. The effect of the β_s mode is alleviated by placing the first torsional frequency $\bar{\omega}_1$ at 2.50. For both θ_{r0} and η_0 actuation, the largest increase due to forward flight occurs at approximately 1Ω . This dominant response is due to the collective flapping or *coning* mode.

The $G_{\eta_0}(j\bar{\omega})$ response with $\bar{\omega}_1 = 2.50$ has more authority than any of the configurations, including root pitch actuation; but may produce excessively large pitch deflections. Too large a pitch angle may push the angle of attack past the stall point. Since the baseline H-34 rotor with $\bar{\omega}_1 = 7.65$ appears too stiff, a modified H-34 with a $\bar{\omega}_1$ of 4.50 will be used to represent a typical smart rotor. With this configuration, 10 deg of servo-flap deflection can provide approximately 0.6 g of DC thrust response. This will allow the servo-flap to augment conventional root pitch trim control, as well as provide sufficient actuation for vibration control and other

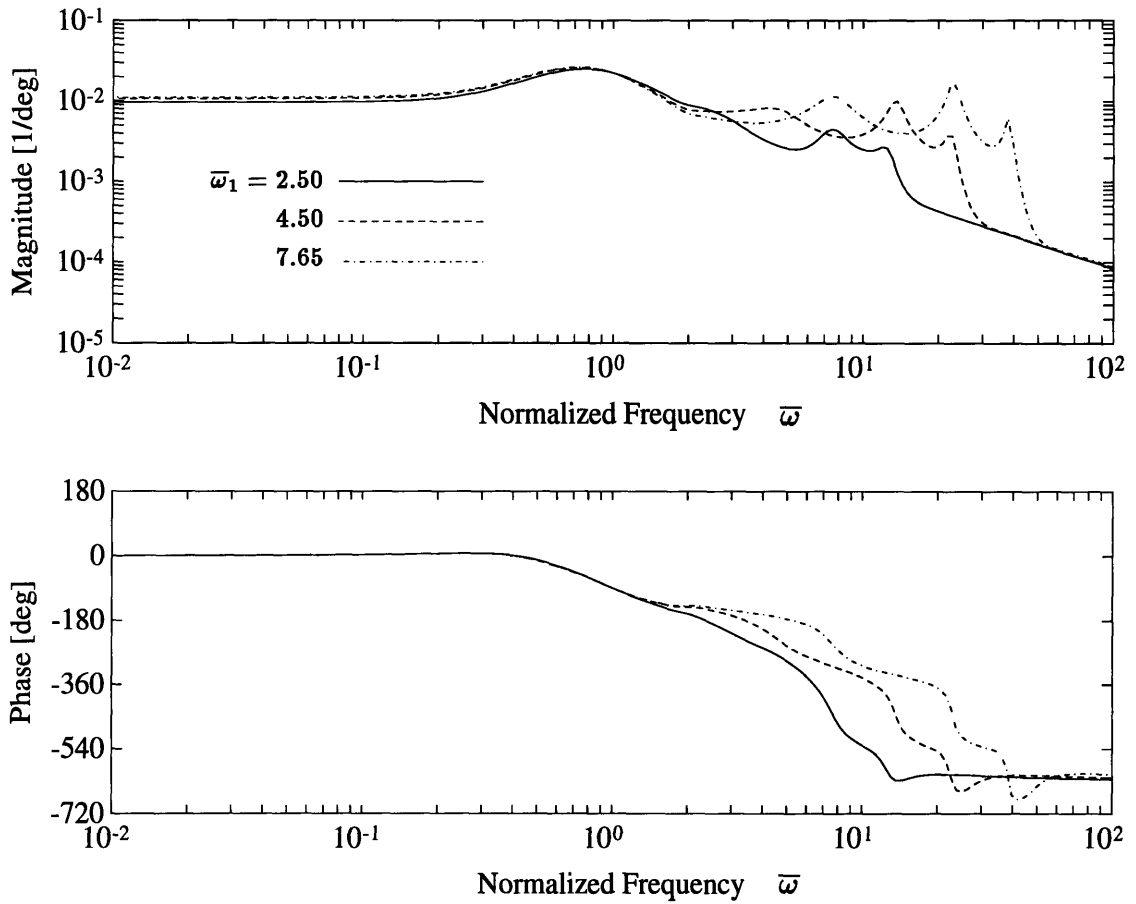


Figure 3-6: The effect of blade torsional stiffness on thrust $G_{\theta_{r0}}(j\bar{\omega})$ for H-34 rotor in edgewise flight ($\mu = .25$).

applications. For a “swashplateless” rotor, at least 1 or possibly 2 g ’s of DC authority would be needed for full maneuvering control. A more comprehensive study of the feasibility of piezoelectric actuators for rotor control is presented by Fox [12].

3.2.2 C.G. Offset and Additional Mass Study

Other practical parameters of interest are the c.g. offset, \bar{x}_{cg} (normalized by the chord), and additional mass, $\Delta\bar{m}$ (normalized by the baseline mass), due to the blade mounted actuator. The \bar{x}_{cg} is of particular importance in determining flutter and stability. For a rotor blade without any structural or aerodynamic damping, any c.g. offset will cause instability. For this reason, assumptions about damping become very important. The amount of damping will determine how much c.g. offset can be

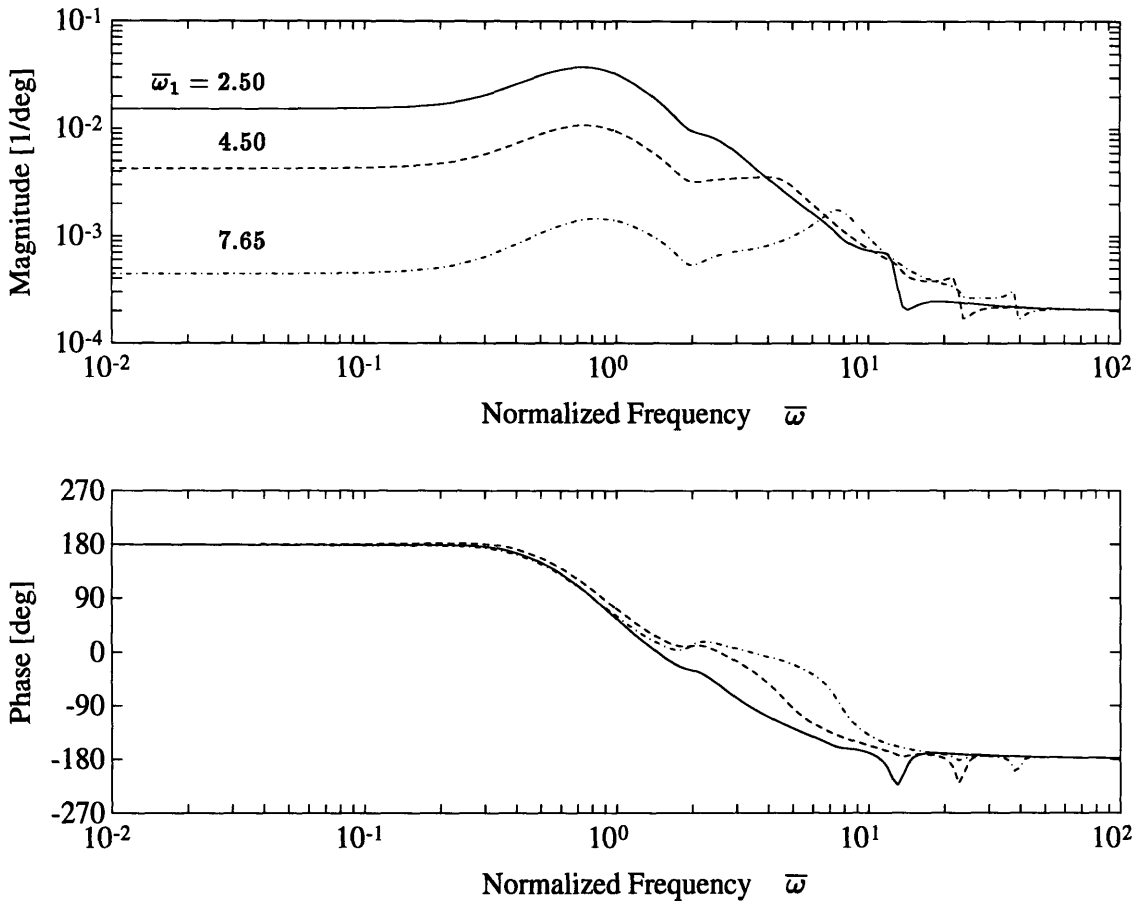


Figure 3-7: The effect of blade torsional stiffness on $G_{\eta_0}(j\bar{\omega})$ for H-34 rotor in edgewise flight ($\mu = 0.25$).

accommodated. Using a H-34 rotor with moderately stiff blades ($\bar{\omega}_1 = 4.50$) as a new baseline, the influence of \bar{x}_{cg} and $\Delta\bar{m}$ on the thrust response was investigated. Once again, cases were run at hover and edgewise forward flight.

Figures 3-8 and 3-9 shows the frequency responses of $G_{\theta_{r0}}(j\bar{\omega})$ and $G_{\eta_0}(j\bar{\omega})$ in hover as \bar{x}_{cg} is varied from 0% to 20% chord. For this study, \bar{x}_{cg} is only varied at the actuator locations and remains unchanged along the rest of the span. Increasing \bar{x}_{cg} improves the authority of both actuation methods in the lower frequency range ($\bar{\omega} \leq 1$). Moving the c.g. back from the pitch axis increases the DC thrust response of the rotor by coupling the centrifugal effects due to flap and elastic pitch motion. The net effect is a reduction in the propeller moment, allowing the blade to twist more and providing a larger thrust response. In the higher frequency range ($1 \leq \bar{\omega} \leq 10$), the effect of varying \bar{x}_{cg} is more subtle. The addition of \bar{x}_{cg} shifts $\bar{\omega}_1$ and $\bar{\nu}_\beta$ down in

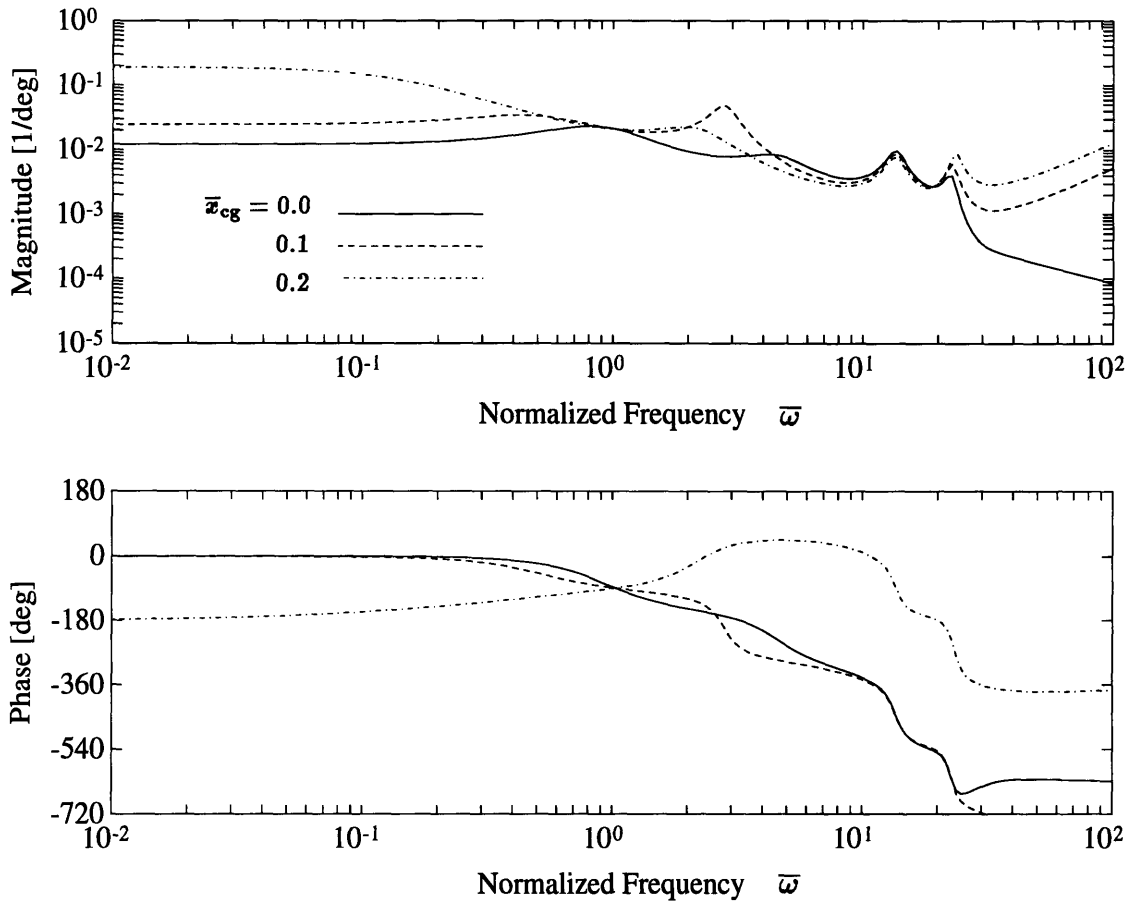


Figure 3-8: The effect of c.g. offset on $G_{\theta_{r0}}(j\bar{\omega})$ for H-34 rotor in hover. Note that $\bar{x}_{cg} = 0.2$ case is unstable.

frequency and decreases the damping of the elastic torsion and rigid flapping modes. It is important to note that the $\bar{x}_{cg} = 0.20$ case is unstable. This shows up as a significant change in phase angle from the other cases in the frequency response plots. For this particular H-34 configuration with the aerodynamic damping approximation of Equation (2.84), increasing \bar{x}_{cg} past 0.12 will drive the system unstable. For all the \bar{x}_{cg} cases in hover, the magnitude and phase response at 1Ω remains unchanged.

Figures 3-10 and 3-11 shows the frequency responses of $G_{\theta_{r0}}(j\bar{\omega})$ and $G_{\eta_0}(j\bar{\omega})$ in edgewise forward flight ($\mu = 0.25$) as \bar{x}_{cg} is once again varied from 0% to 20% chord. These responses show the same general trends as the hover cases except for the presence of cyclic modes. The $\bar{x}_{cg} = 0.2$ remains unstable. In the $\bar{x}_{cg} = 0.1$ case, the coning mode shifts in magnitude and frequency, and the lateral tilt mode serves to accentuate the thrust response at 2Ω . In hover, the cyclic modes do not contribute

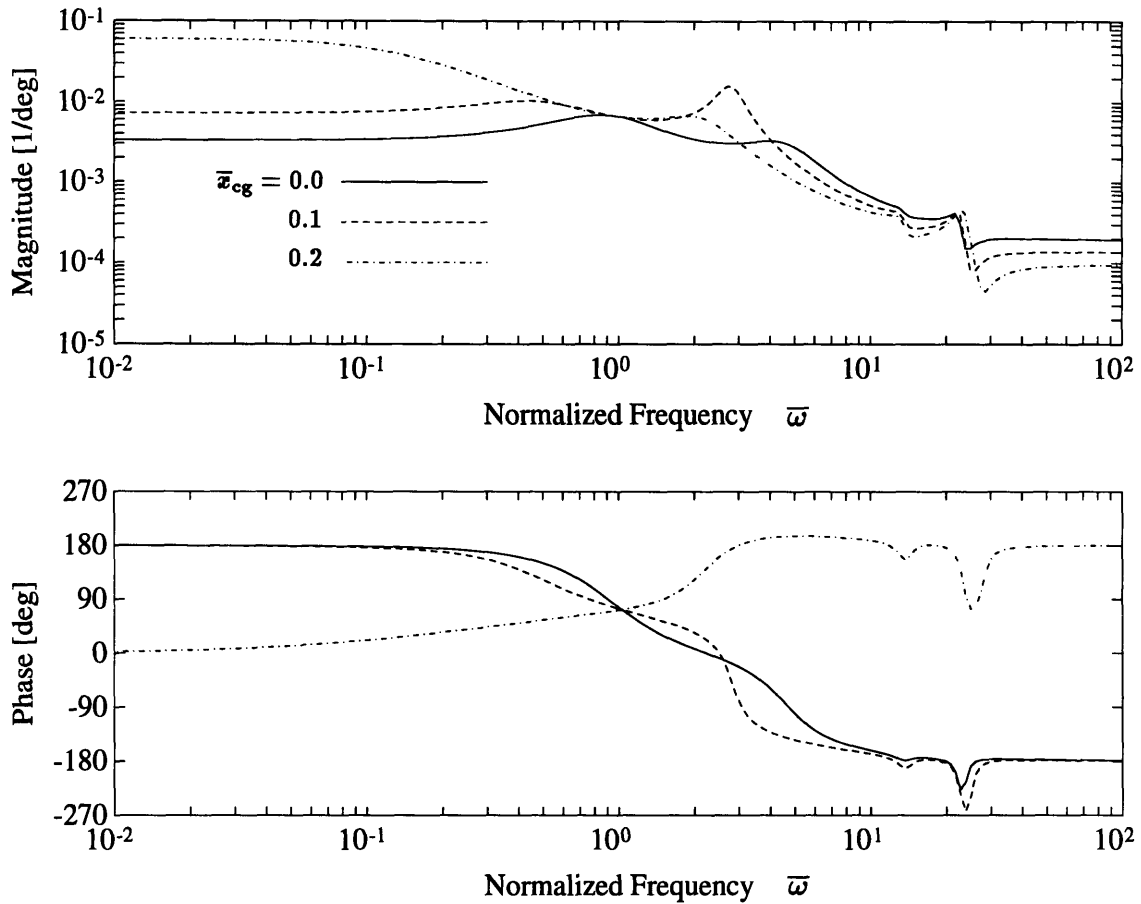


Figure 3-9: The effect of c.g. offset on $G_{\eta_0}(j\bar{\omega})$ for H-34 rotor in hover. Note that $\bar{x}_{cg} = 0.2$ case is unstable.

to the thrust response, which is interpreted as a perfect pole/zero cancellation. As the rotor moves into forward flight, the cyclic pole/zero pairs move apart.

The effect of additional mass and pitch inertia is investigated separately from the c.g. offset. Figures 3-12 and 3-13 show the θ_{r0} and η_0 thrust responses as the mass and pitch inertias at the servo-flap locations is varied from nominal to twice the nominal value. The term $\Delta\bar{m}$ is the sectional actuator mass normalized by the baseline sectional mass of the rotor blade. It is assumed that the pitch inertia increases proportionally with the mass. Increasing the mass decreases the Locke number γ , which is a measure of damping for the β dynamics. This decrease in damping provides both actuation methods with increased authority especially due to the coning mode at $\bar{\omega} \approx 1$, but it further limits the amount of \bar{x}_{cg} that can be accommodated. The increase in pitch inertia also shifts $\bar{\omega}_1$ down slightly in frequency.

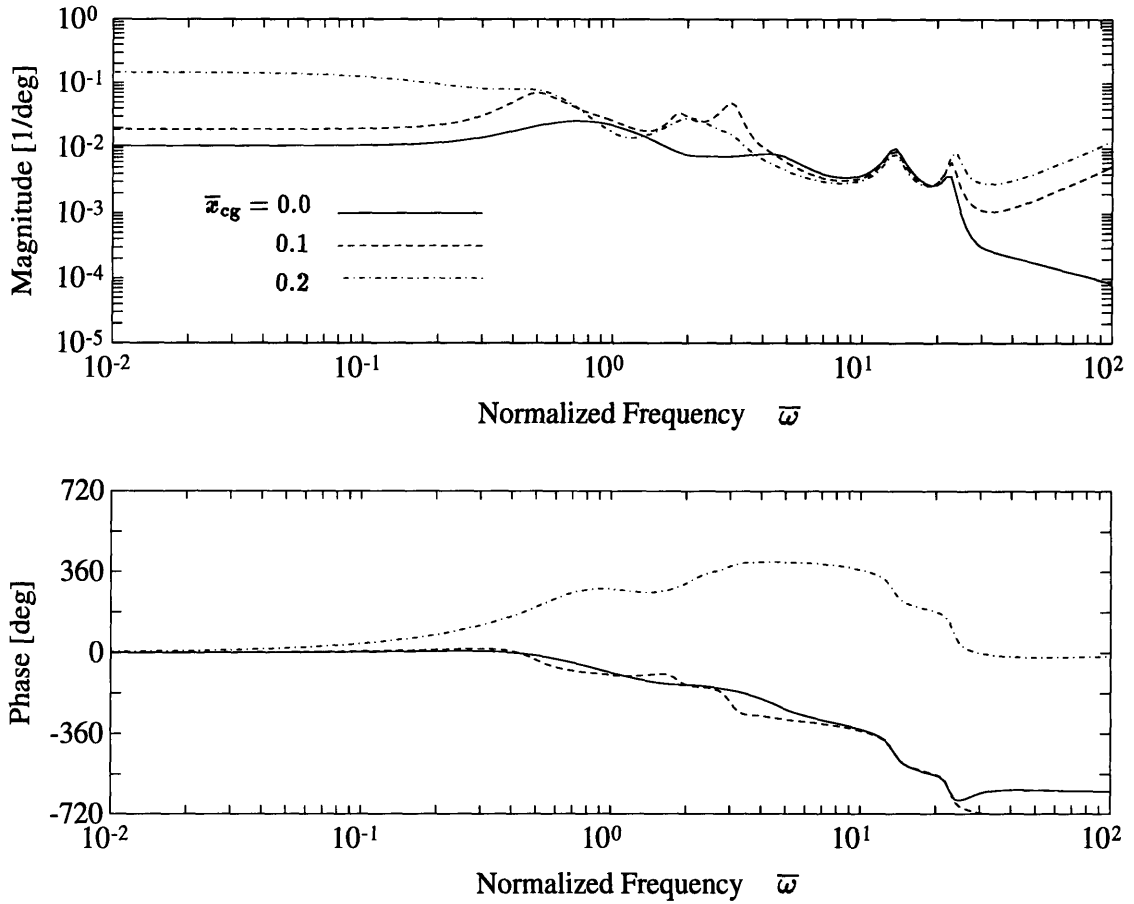


Figure 3-10: The effect of c.g. offset on $G_{\theta,0}(j\bar{\omega})$ of H-34 rotor in edgewise flight ($\mu = 0.25$). Note that $\bar{x}_{cg} = 0.2$ case is unstable.

To offset \bar{x}_{cg} stability problems, additional mass may be added to bring the center of mass closer to the pitch axis. This additional mass does not adversely affect root pitch or servo-flap authority, but it may increase the required control loads. The stability of the rotor system is highly dependent on the c.g. offset and the aerodynamic damping assumptions. A safe approach to implementing blade-mounted actuators is to accept the additional mass penalty while keeping \bar{x}_{cg} as small as possible. In general, any \bar{x}_{cg} offset is undesirable in terms of stability, although it does increase the magnitude of the thrust response especially at DC. It has been proposed that this aeroelastic instability can be feedback stabilized to take advantage of this increased authority [25]. Work by Loewy proposes the use of “feedback stabilized aerodynamically overbalanced controls” to deflect a trailing edge flap for airstream actuated rotor control.

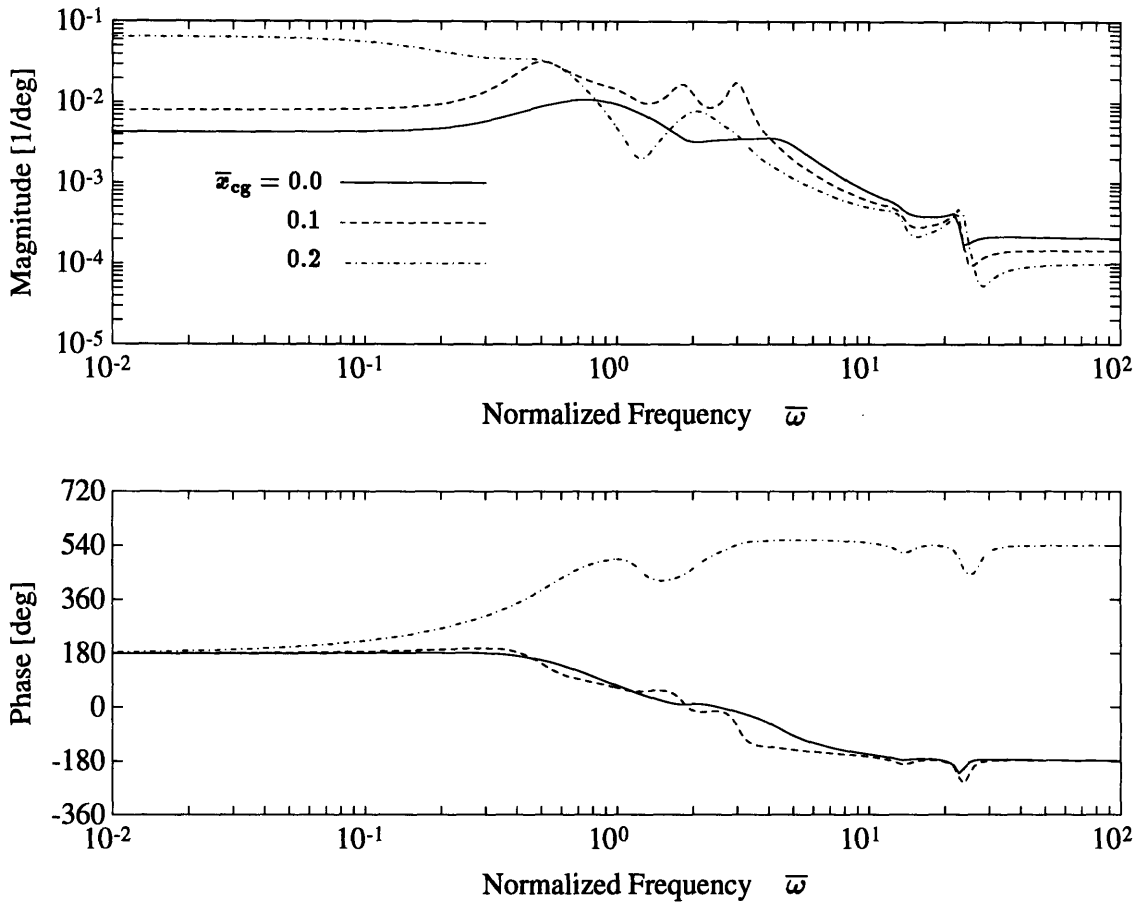


Figure 3-11: The effect of c.g. offset $G_{\eta_0}(j\bar{\omega})$ for H-34 rotor in edgewise flight ($\mu = 0.25$). Note that $\bar{x}_{cg} = 0.2$ case is unstable.

3.2.3 Actuator Placement Study

In this subsection, the effect of servo-flap placement on $G_{\theta_{r0}}(\bar{s})$ and $G_{\eta_0}(\bar{s})$ is investigated. Keeping the servo-flap span a constant $0.20R$, its radial position is varied from $\bar{r} = 0.5\text{--}0.7$ to $\bar{r} = 0.7\text{--}0.9$ in both hover and forward flight conditions. To insure that the rotor blades operate in reversal, the servo-flap is placed outboard of the 50% span. Inboard of this position, a servo-flap is less effective in twisting the blade into reversal. For practical reasons, the servo-flap is kept inboard of the 90% radial station to avoid tip loss effects. In reality, the servo-flap may encounter trailing tip vortices which will significantly affect the flap's performance. While moving the servo-flap outboard should increase its authority, this will require a stronger actuator, since the dynamic pressure is proportional to \bar{r}^2 . Servo-flap placement is a trade-off between

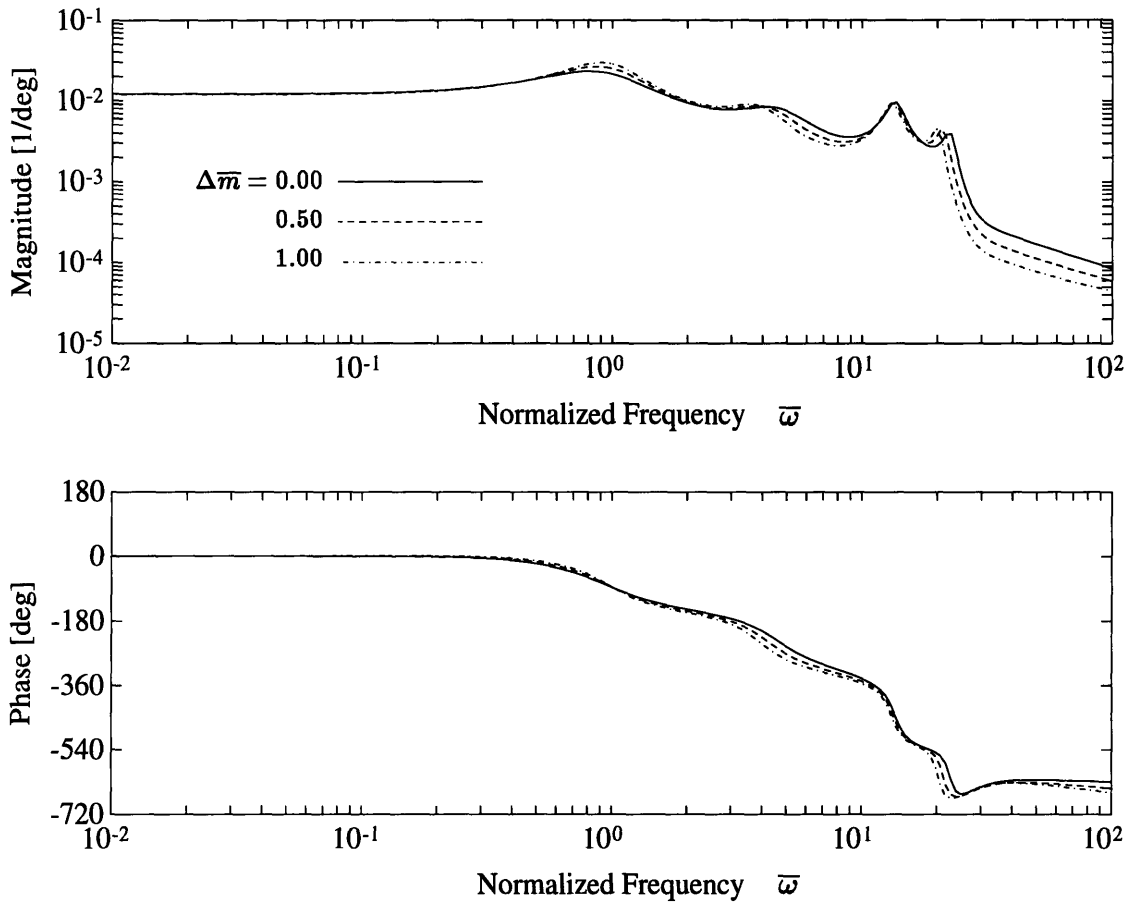


Figure 3-12: The effect of additional actuator mass on $G_{\theta_0}(j\bar{\omega})$ for H-34 rotor.

desired thrust response and the amount of deflection the actuator can achieve in the face of high dynamic pressures.

Figure 3-14 shows the frequency response $G_{\eta_0}(\bar{s})$ in hover as the actuator is moved outboard. Moving the servo-flap from 0.50–0.70 to 0.70–0.90 increases the DC response by approximately 150% (0.03 g/deg), the 1Ω response by 120% (0.06 g/deg), and the 4Ω response by about 100% (0.02 g/deg). Figure 3-15 presents the same study conducted in edgewise forward flight ($\mu = 0.25$) and shows the same general trends. The higher dynamic pressure on the advancing side of the rotor due to forward flight provides an increase in authority which is offset by the presence of the first cyclic modes, especially the β_s mode. Most of the increase in authority occurs at 1Ω due to the coning mode. The higher frequency response ($\bar{\omega} \geq 10$) shows considerable changes as the actuator is moved from the nodes to the anti-nodes of the second and

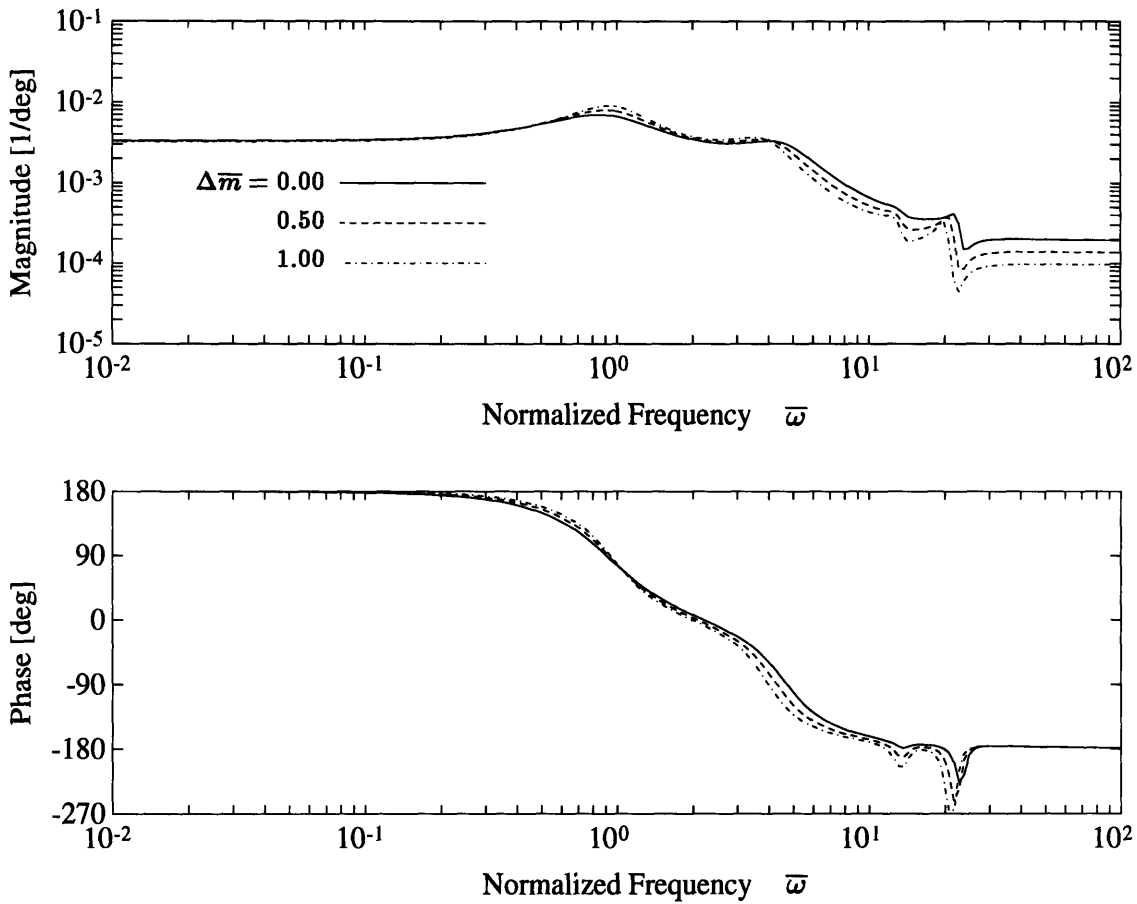


Figure 3-13: The effect of additional actuator mass on $G_{\eta_0}(j\bar{\omega})$ for H-34 rotor in hover.

third torsional modes.

3.2.4 Aileron Reversal Study

To provide sizable thrust control, it is desired that the rotor blades operate in aileron reversal, which is dependent on the torsional stiffness and many other parameters. The amount of torsional moment provided by the servo-flap depends on spanwise placement and advance ratio. It also depends on the flap/chord ratio of the actuator, but this will be constrained by the sectional structure and geometry of the rotor blade and will not be investigated. This aileron reversal study will only look at the H-34 rotor *in hover*. If the servo-flap system is able to “reverse” the rotor in hover, then it should be able to accomplish this in forward flight due to the increased dynamic pressure.

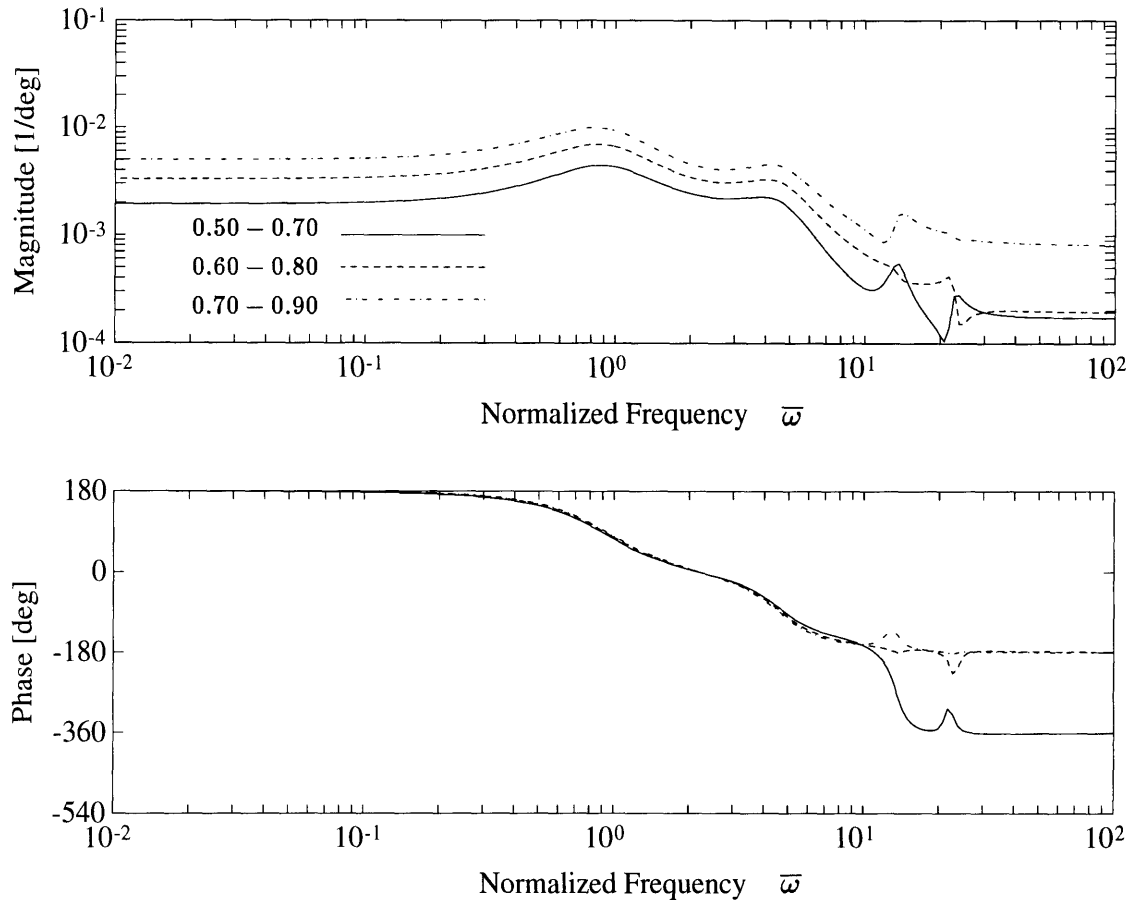


Figure 3-14: The effect of actuator placement on $G_{\eta_0}(j\bar{\omega})$ for H-34 rotor in hover.

In this section, the influence of torsional stiffness, rotor blade inertia, Lock number, and actuator placement on aileron reversal will be illustrated.

At hover for the $\bar{\omega}_1 = 2.50$ and 4.50 stiffness cases (Figure 3-5), the rotor is in reversal at DC, since the phase angle is 180 deg. This means that for a positive flap deflection, there is a net negative thrust response, and vice versa. The *rotor reversal* point occurs when the incremental thrust due to the servo flap is canceled out by the thrust response of the entire rotor. At this point, any flap deflection will cause no net thrust response. It is analogous to aileron reversal for a fixed wing, and takes into account induced inflow and a radially and azimuthally varying velocity field, effects specific to the rotor environment.

Using the full state space rotor model, the sensitivity of the DC $G_{\eta_0}(j\bar{\omega})$ response to torsional stiffness ($\bar{\omega}_1$) is evaluated and presented in Figure 3-16. Using this analy-

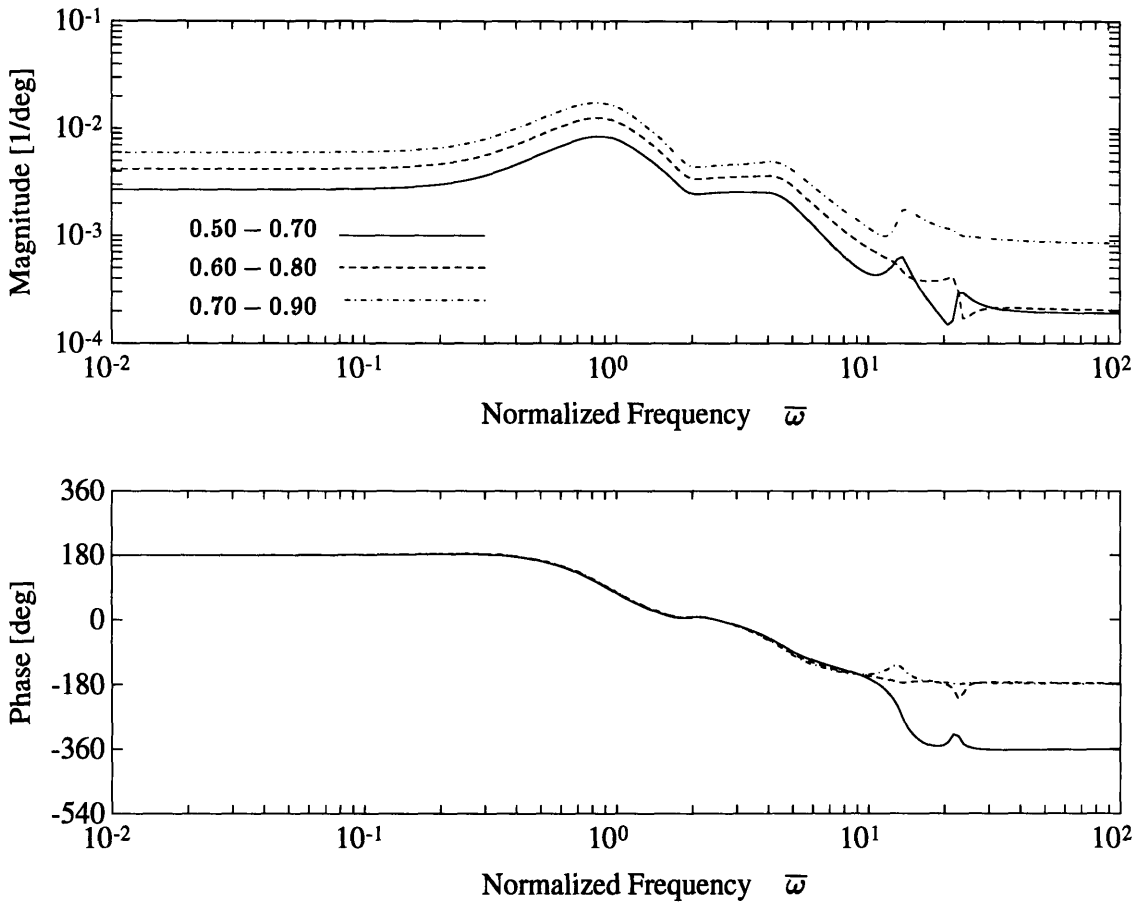


Figure 3-15: The effect of actuator placement on $G_{n0}(j\bar{\omega})$ for H-34 rotor in edgewise flight ($\mu = 0.25$).

sis, H-34 rotor reversal at hover occurs for $\bar{\omega}_1 = 7.56$. For rotor blades with $\bar{\omega}_1 < 7.56$, aileron reversal is guaranteed, with the thrust response being 180 deg out of phase with servo-flap deflection. For rotor blades with $\bar{\omega}_1 > 7.56$, the rotor is not in aileron reversal, with the thrust response being in phase with the servo-flap deflection. Most of the thrust response for $\bar{\omega}_1 > 7.56$ is due to the incremental lift provided by the servo-flap. For the limiting case of a torsionally rigid blade ($\bar{\omega}_1 = \infty$), the thrust response is entirely due to the servo-flap.

The baseline H-34 rotor in hover is just to the right of the reversal point with $\bar{\omega}_1 = 7.65$. This explains the significantly lower magnitude and 0 deg of phase angle at DC compared to the less stiff rotors (see Figure 3-5). In forward flight, the $\bar{\omega}_1 = 7.65$ rotor exhibits a 180 deg phase angle at DC (see Figure 3-7). The increased dynamic pressure provides the servo-flap with more authority to twist the $\bar{\omega}_1 = 7.65$ blade

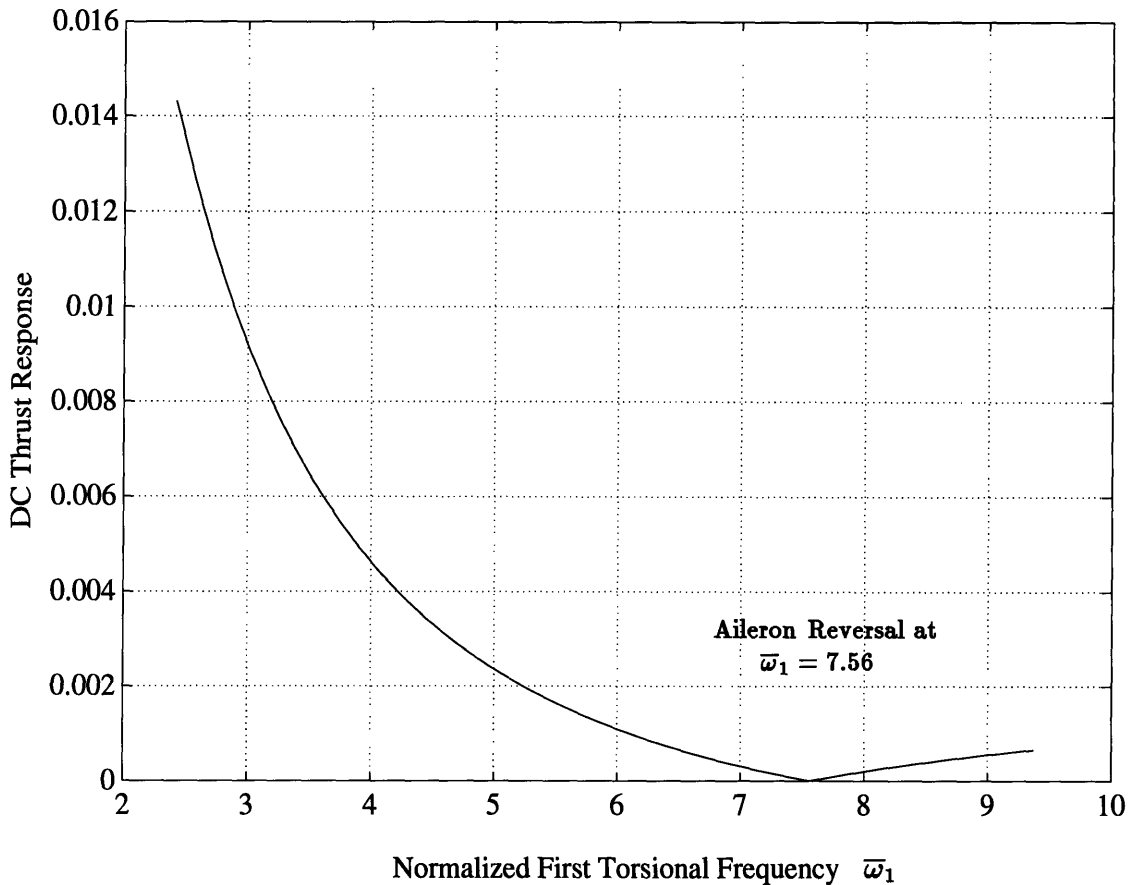


Figure 3-16: Aileron reversal study for the H-34 rotor in hover. Based on state space model analysis.

into reversal, although the magnitude of the thrust response remains quite small. If a complete aileron reversal study were conducted with $\mu = 0.25$, it is predicted that the torsional frequency $\bar{\omega}_1$ for the reversal point would be shifted upward.

The state space model could be employed to conduct studies on the sensitivity of rotor reversal to various parameters, but a simple, less computationally intensive analysis can be derived for a rotor in hover. It would be desirable to define a range of typical rotor parameters that would guarantee rotor reversal. This would be useful in determining the applicability of servo-flaps to existing helicopter rotors and providing a quick check on new rotor designs.

To start off this simple analysis, a rotor blade with only elastic pitch is assumed. No flap motion or inflow velocity will be included. The rotor blade is torsionally clamped at $r = e$, and the airfoil spans $r_c \leq r \leq R$. The aerodynamic moment of the

servo-flap will be modelled as a *point moment* acting on a uniform rod at position R_o . The total lift of the system has components due to the angle attack distribution of the blade, L_{blade} and the incremental lift due to servo-flap deflection, L_η ,

$$L_{\text{total}} = L_{\text{blade}} + L_\eta \quad (3.2)$$

$$= L_\eta(K + 1), \quad (3.3)$$

where

$$K = \frac{L_{\text{blade}}}{L_\eta}. \quad (3.4)$$

At aileron reversal, $K = -1$. In this simplified formulation, the angle of attack is equivalent to the pitch angle θ . The lift of the rotor blade due to θ is

$$L_{\text{blade}} = \int_{r_c}^R \frac{1}{2} \rho \Omega^2 r^2 c a \theta(r) dr. \quad (3.5)$$

The lift and moment produced by the servo-flap are

$$L_\eta = \frac{1}{2} \rho \Omega^2 R_o^2 c n \eta \Delta R, \quad (3.6)$$

$$M_\eta = \frac{1}{2} \rho \Omega^2 R_o^2 c^2 p \eta \Delta R. \quad (3.7)$$

The servo-flap spans a distance ΔR along the blade, but these terms will eventually drop out in the derivation.

It is assumed that the pitch angle distribution is defined by the elastic pitch expression of Equation (2.22), so that

$$\theta(\bar{r}) = \sum_k \xi_{\theta_k}(\bar{r}) \theta_k. \quad (3.8)$$

The pitch angle deflection due to the point moment M_η acting at \bar{R}_o is simply

$$\theta(\bar{r}) = \sum_k \frac{M_\eta}{I_{\theta_k} \omega_k^2} \xi_{\theta_k}(\bar{R}_o) \xi_{\theta_k}(\bar{r}). \quad (3.9)$$

Evaluating the term K and substituting non-dimensional parameters yields the ex-

Table 3.2: Typical rotor parameters.

Parameters	Typical Values
\bar{c}	0.5–0.1
\bar{e}	0.05
\bar{r}_c	0.15
\bar{r}_1	0.6
\bar{r}_2	0.8
n	3.13
p	-0.513
$I_{\theta_1}^*$	$0.033\bar{c}^2$
$\bar{\omega}_1$	4–6
γ	7–9

pression

$$K = \frac{1}{2} \bar{c} \gamma \frac{p}{n} \sum_k \frac{1}{I_{\theta_k}^* \bar{\omega}_k^2} \xi_{\theta_k}(\bar{R}_o) \int_{\bar{r}_c}^1 \bar{r}^2 \xi_{\theta_k}(\bar{r}) d\bar{r}. \quad (3.10)$$

Setting $K = -1$, one can evaluate the reversal point given a set of rotor parameters. Figure 3-17 shows aileron reversal curves versus $\bar{\omega}_1$ and R_o for the H-34 rotor and some typical rotors. Typical rotor parameters are listed in Table 3.2. Given servo-flap location, R_o , and a first torsional frequency, $\bar{\omega}_1$, one can determine if rotor reversal is possible. Looking at Figure 3-17, rotor reversal is achieved if the point $(R_o, \bar{\omega}_1)$ is below the curve for that particular rotor. As expected, moving the servo-flap outboard and making the blade less stiff makes aileron reversal easier. A more subtle trend is demonstrated by the Locke number, γ . As γ increases, the aileron reversal curve shifts upward. The physical interpretation of this trend is that decreasing the rotor blade's inertia makes rotor reversal easier to achieve.

For the H-34 rotor evaluated by the full state space model, the servo-flap was centered at $R_o \approx 0.7$ with the reversal point occurring at $\bar{\omega}_1 = 7.56$. The simplified analysis yields a slightly higher $\bar{\omega}_1$ of 7.75 for H-34 rotor reversal. This is to be expected, since the simplified model does not include lift deficiency due to downwash

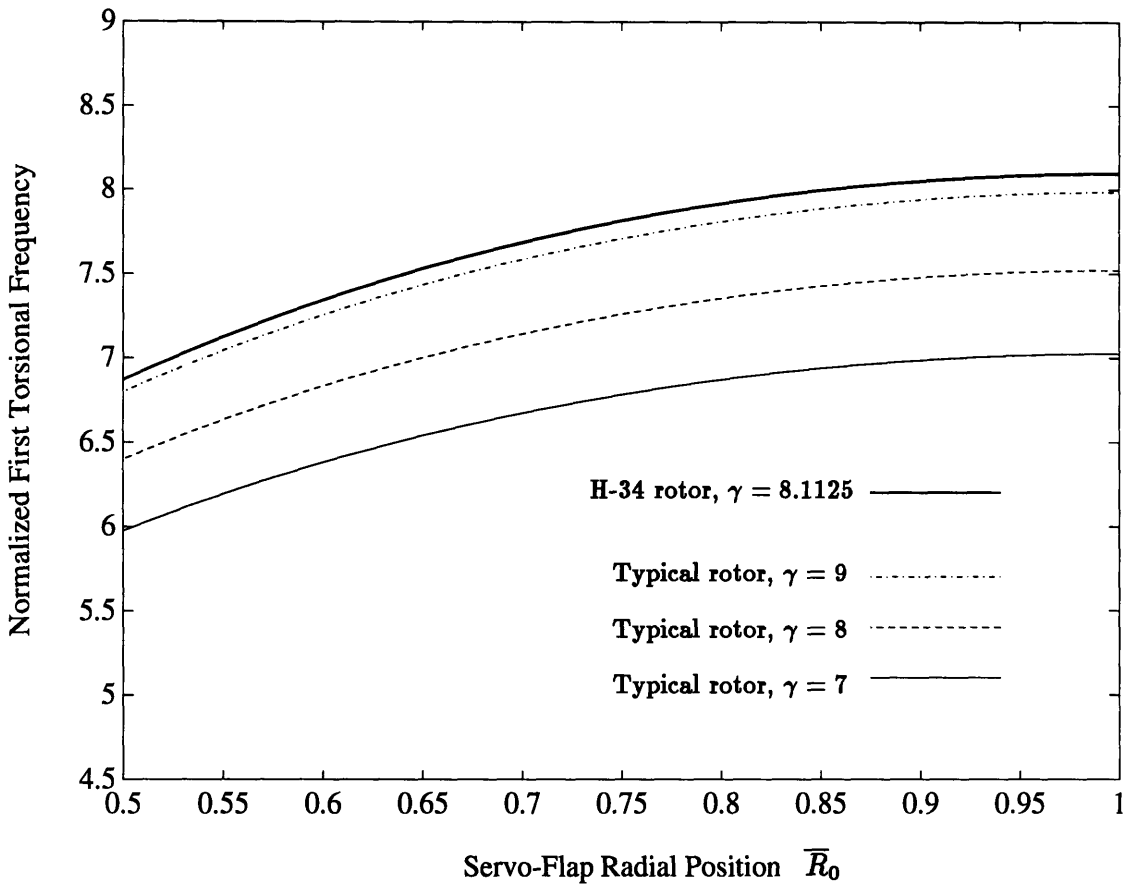


Figure 3-17: Aileron reversal curves for typical rotor parameters and the H-34 rotor in hover. Based on simplified analysis.

and centrifugal stiffening effects. Since the state space model includes these effects, it provides a more conservative answer. Regardless, this simplified aileron reversal analysis is within 2% of the full analysis and can provide a quick check on torsional stiffness, servo-flap placement, and other parameters to insure aileron reversal. Looking again at Figure 3-17, it is apparent that placing a servo-flap outboard of the 50% span will guarantee aileron reversal for most typical rotors with $\bar{w}_1 = 4\text{--}6$.

Chapter 4

Servo-Flap Actuation for Higher Harmonic Control

As discussed in Chapter 1, a number of research projects have demonstrated the use of higher harmonic swashplate actuation, primarily at $N\Omega$, for vibration reduction. Because of the limitations of the swashplate mechanism, an alternative actuation method may be better suited for higher harmonic control (HHC). In this chapter, HHC algorithms will be applied to servo-flap rotor actuation. As mentioned earlier, piezo-electric driven servo-flaps have a higher bandwidth and encounter smaller control loads compared to electro-hydraulic swashplate actuators. Based on the previous parametric study section, a rotor equipped with trailing edge flaps can provide adequate higher harmonic vibration control using reasonable servo-flap deflections. The actual magnitude of servo-flap deflection required for HHC will vary depending on the rotor system.

The results of Chapter 3 presented the open-loop characteristics of various rotor plants using root pitch and servo-flap control inputs. The intent of this chapter is to close the loop using HHC algorithms and investigate any limitations of the servo-flap actuation scheme on performance and stability. First, the actuator requirements for adequate HHC vibration reduction will be investigated. A comparison of servo-flap and root pitch control loads for the H-34 rotor will be made. In the following section, the characterization of various HHC compensators to classical narrowband

disturbance rejection will be made based on work by Hall and Wereley [15]. Particular examples include the discrete time HHC algorithm proposed by Shaw [39] and frequency shaped cost function designs proposed by Gupta and DuVal [14]. A continuous time compensator will be applied to the state space rotor model using both root pitch and servo-flap actuation, and the closed-loop system will be evaluated. A linear quadratic regulator design will also be used to demonstrate multivariable vibration control with servo-flap control inputs.

4.1 Higher Harmonic Control Loads

A proposed benefit of blade-mounted servo-flap actuation is a reduction in the required control loads compared to root pitch actuation. This section will evaluate the control loads required for 0.25 g of HHC authority. The necessary root pitch and servo-flap commands to provide a 0.25 g thrust response at 4Ω will be determined using the H-34 smart rotor defined in the previous chapter. Based on these values, the required torque to feather the entire blade and the required aerodynamic hinge moment to deflect the servo-flap will be calculated.

Table 4.1 presents 4Ω thrust response data based on the H-34 rotor with a modified first torsional frequency $\bar{\omega}_1 = 4.5$ and a 20% servo-flap spanning from $\bar{r}_1 = 0.6$ to $\bar{r}_2 = 0.8$. The C_T/σ responses as well as the required root pitch and servo-flap amplitude for 0.25 g are listed. The authority in g 's is obtained by dividing the C_T/σ response by the nominal $C_T/\sigma = 0.1$, which roughly corresponds to 1 g of thrust. Both hover and forward flight cases are included.

For root pitch actuation, the control load is the required torque to feather the blade at $N\Omega$. Normalizing by $I_b\Omega^2$, the non-dimensional root pitch control load is

$$u_{\theta_{r0}} = \frac{I_\theta |\ddot{\theta}_{r0}|}{I_b \Omega^2} = I_\theta^* N^2 |\theta_{r0}| , \quad (4.1)$$

where $|\theta_{r0}|$ is the required root pitch amplitude.

For servo-flap actuation, the control load is the aerodynamic hinge moment en-

Table 4.1: Thrust response data for H-34 rotor at 4Ω .

Flight Case	$ C_T/\sigma /\theta_{r0}$ (per deg)	$ C_T/\sigma /\eta_0$ (per deg)	$ \theta_{r0} $ for $0.25 g$ (deg)	$ \eta_0 $ for $0.25 g$ (deg)
Hover	0.0084	0.0033	3.0	7.5
Edgewise Forward Flight ($\mu = 0.25$)	0.0081	0.0036	3.1	6.9

countered by the servo-flap. The largest aerodynamic hinge moment will occur at the advancing side of the rotor ($\psi = 90$ deg). Quasi-static thin airfoil theory will be used to evaluate this hinge moment. Based on work by Glauert [13], the hinge moment due to a servo-flap deflection η is

$$M_H = (Ec)^2 \rho V^2 b_2 \eta , \quad (4.2)$$

where E is the flap/chord ratio. Defining the following terms

$$a_2 = \pi - 2 \left[\cos^{-1} \sqrt{E} - \sqrt{E(1-E)} \right] \quad (4.3)$$

$$b_1 = \frac{1}{E^2} \left[\left(\frac{3}{2} - E \right) \sqrt{E(1-E)} - \left(\frac{3}{2} - 2E \right) \left(\frac{\pi}{2} - \cos^{-1} \sqrt{E} \right) \right] \quad (4.4)$$

$$b = \frac{2(1-E)\sqrt{E(1-E)}}{E^2} \left[\frac{\pi}{2} - \cos^{-1} \sqrt{E} - \sqrt{E(1-E)} \right] \quad (4.5)$$

the term b_2 is given by

$$b_2 = b_1 \frac{a_2}{\pi} - b . \quad (4.6)$$

Normalizing M_H by $I_b \Omega^2$, the non-dimensional control load due to servo-flap deflection is

$$u_{\eta_0} = \frac{M_H}{I_b \Omega^2} = \gamma E^2 \bar{c} \frac{b_2}{a} \left[\frac{1}{3} (\bar{r}_2^3 - \bar{r}_1^3) + (\bar{r}_2^2 - \bar{r}_1^2) \mu + (\bar{r}_2 - \bar{r}_1) \mu^2 \right] |\eta_0| \quad (4.7)$$

where $|\eta_0|$ is the required servo-flap amplitude. Note that this is the maximum control load encountered by the advancing rotor blade at $\psi = 90$ deg.

Table 4.2: Required non-dimensional control loads for H-34 rotor at 4Ω .

Flight Case	$ u_{\theta,r_0} $	$ u_{\eta_0} $
Hover	1.04	3.27×10^{-2}
Edgewise Forward Flight ($\mu = 0.25$)	1.07	6.13×10^{-2}

The resulting control loads for the H-34 smart rotor are presented in Table 4.2 showing orders of magnitude differences between u_{θ,r_0} and u_{η_0} requirements. As expected, the servo-flap control load requirements for HHC are significantly less than the control loads required for root pitch actuation. The required torque for root pitch actuation stays fairly constant as the advance ratio increases. The servo-flap hinge moments, however, are much more sensitive to forward flight conditions due to the increased dynamic pressure. Note the large change in u_{η_0} from hover to forward flight. Although the required servo-flap amplitude decreases with forward flight, the required control load increases. Using the state space rotor model and this simple control load analysis as a guide, actuator requirements for HHC can be obtained.

4.2 HHC Algorithms

A number of HHC algorithms have been developed which range from simple fixed gain controllers to fully adaptive systems. Most of these techniques utilize the control response matrix, \mathbf{T} , which relates the Fourier coefficients of the $N\Omega$ control inputs to the $N\Omega$ vibration outputs. One method developed by Shaw [39] utilizes a discrete time HHC algorithm based on a quasi-steady assumption with the plant dynamics represented by \mathbf{T} . The helicopter plant is considered quasi-steady if the settling time of the plant is short compared to that of the closed-loop system. The sine and cosine

components of the N/rev vibration can be defined by

$$\mathbf{y} = \mathbf{T}\mathbf{u} + \mathbf{y}_0 , \quad (4.8)$$

where \mathbf{y} is the vibration output vector, \mathbf{u} is the control input vector, and \mathbf{y}_0 is the vibration level vector without any control input. The resulting discrete time control law is simply

$$\mathbf{u}_{n+1} = \mathbf{u}_n - \mathbf{T}^{-1} \mathbf{y}_n , \quad (4.9)$$

where the subscript n corresponds to the time step index.

The helicopter rotor can also be represented by a SISO, LTI transfer function $G(s)$. With the LTI assumption, the \mathbf{T} matrix represents the rotor plant at the frequency $N\Omega$ such that

$$\mathbf{T} = \begin{bmatrix} \operatorname{Re}\{G(jN\Omega)\} & \operatorname{Im}\{G(jN\Omega)\} \\ -\operatorname{Im}\{G(jN\Omega)\} & \operatorname{Re}\{G(jN\Omega)\} \end{bmatrix} . \quad (4.10)$$

Applying Shaw's algorithm to $G(s)$, the equivalent continuous time compensator is shown in [15] to be

$$H(s) = -\frac{u(s)}{y(s)} = \frac{2k(as + bN\Omega)}{s^2 + (N\Omega)^2} , \quad (4.11)$$

where

$$a = \operatorname{Re}\{G(jN\Omega)\}/|G(jN\Omega)|^2 , \quad (4.12)$$

$$b = \operatorname{Im}\{G(jN\Omega)\}/|G(jN\Omega)|^2 , \quad (4.13)$$

$$k = 1/T . \quad (4.14)$$

The term T is analogous to the update period in the discrete-time HHC algorithm and can be viewed as the settling time of the closed-loop system. For most systems, T is approximately the period of one rotor revolution.

An LTI assumption allows the helicopter dynamics to be represented in an LTI state space format. This allows the application of numerous multivariable control techniques. In particular, the LQR/FSCF (Linear Quadratic Regulator/Frequency Shaped Cost Function) approach presented by Gupta and DuVal in Reference 14

yields a compensator similar in form to Equation 4.11. The helicopter plant $G(s)$ can be represented in state space form

$$\dot{\mathbf{x}}_p(t) = \mathbf{A}_p \mathbf{x}_p(t) + \mathbf{B}_p u(t), \quad (4.15)$$

$$y(t) = \mathbf{C}_p \mathbf{x}_p(t) + d(t), \quad (4.16)$$

where $\mathbf{x}_p(t)$ is the state vector, $u(t)$ is the control input, $d(t)$ is the disturbance at the output, and $y(t)$ is the vibration output. By placing a filter of the form

$$G_n(s) = \frac{(N\Omega)^2 s}{s^2 + (N\Omega)^2} \quad (4.17)$$

at the vibration output and augmenting the filter states \mathbf{x}_n to the plant states \mathbf{x}_p to form a new state vector \mathbf{x} , the optimal feedback gains \mathbf{F} are obtained from solving the LQR problem. The resulting control law for the LQR/FSCF approach is

$$u(t) = -\mathbf{F}\mathbf{x}. \quad (4.18)$$

It has been shown in Reference 15 that the resulting simplified LQR/FSCF compensator can be written as

$$H(s) = \frac{(F_1 + F_2)(N\Omega)^2}{s^2 + (N\Omega)^2} \quad (4.19)$$

which is similar in form to the continuous time compensator of Equation 4.11.

4.3 Implementing HHC

Using a compensator of the form of Equation 4.11, the sensitivity transfer function of a higher harmonic control system using servo-flap actuators is evaluated. The sensitivity transfer function is defined as

$$S(s) = \frac{1}{1 + G(s)H(s)} \quad (4.20)$$

and represents the closed-loop system response to disturbances at the output. In HHC, the objective is to reject disturbances at a known frequency $N\Omega$. Using the normalized Laplace variable $\bar{s} = s/\Omega$, the HHC compensator is

$$H(\bar{s}) = \frac{1}{\pi} \frac{a\bar{s} + bN}{\bar{s}^2 + N^2}. \quad (4.21)$$

This is based on a closed-loop settling time of one rotor revolution, or $T = 2\pi/\Omega$. In the following sections, the compensator $H(\bar{s})$ will be applied to the plants $G_{\theta_{r0}}(\bar{s})$ and $G_{\eta_0}(\bar{s})$. These plants are based on the H-34 smart rotor presented in Chapter 3, with $\bar{\omega}_1 = 4.5$ and a 20% servo-flap spanning from $\bar{r}_1 = 0.6$ to $\bar{r}_2 = 0.8$.

The transfer functions $G_{\theta_{r0}}(\bar{s})$ and $G_{\eta_0}(\bar{s})$ represent the hub thrust response to root pitch and servo-flap inputs. Since the thrust is proportional to vertical acceleration, closing the loop around these particular plants is functionally equivalent to using accelerometers as feedback sensors. The closed-loop HHC systems involving $G_{\theta_{r0}}(\bar{s})$ and $G_{\eta_0}(\bar{s})$ can be evaluated using a variety of techniques including bode plots, Nichols charts, and pole diagrams.

Bode plots of the loop and sensitivity transfer functions of the H-34 rotor to thrust disturbances are presented in Figures 4-1 and 4-2. The rotor model being evaluated is the H-34 rotor flown at a moderate advance ratio of $\mu = 0.15$. Figure 4-1 shows the transfer functions due to root pitch input, and Figure 4-2 shows the same functions due to servo-flap input. Both bode plots are very similar and possess good performance and robustness characteristics. In theory, any disturbance at 4Ω will be completely rejected. These plots also exhibit good gain and phase margin characteristics.

Looking at a Nichols chart of the loop transfer functions $G_{\theta_{r0}}(\bar{s})H(\bar{s})$ (Figure 4-3) and $G_{\eta_0}(\bar{s})H(\bar{s})$ (Figure 4-4), root pitch and servo-flap HHC systems have similar performance and robustness characteristics. Once again, the H-34 rotor flown at an advance ratio of $\mu = 0.15$ is used. The curves for both $G_{\theta_{r0}}(\bar{s})H(\bar{s})$ and $G_{\eta_0}(\bar{s})H(\bar{s})$ stay outside the 0 dB contour indicating that vibration disturbances are always attenuated. Stability and robustness information is interpreted based on how far the

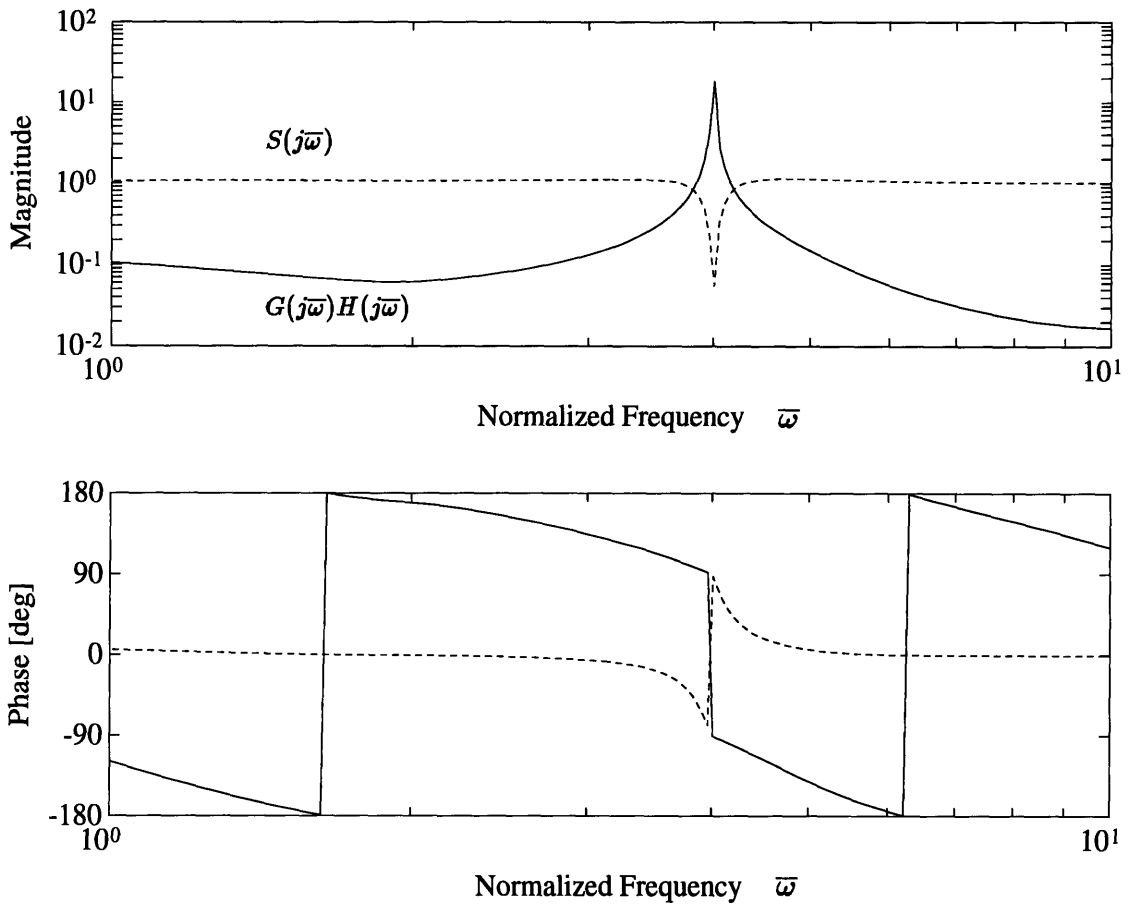


Figure 4-1: HHC loop and sensitivity transfer functions: root pitch actuation.

loop transfer function curves are from the -1 point (0 dB magnitude and 180 deg phase). These Nichols plots show gain margins of about 20 dB and phase margins of about 90 deg. It is apparent from these plots that a rotor equipped with servo-flap actuators can provide good HHC performance comparable to root pitch actuation.

The work of DuVal *et al.* [10] investigates the use of an LQG based controller with full state feedback and a simplified controller which utilizes only the vertical accelerometer signal for feedback. The rotor model used in [10] was in hover and only incorporated a rigid flapping degree of freedom. By using only vertical acceleration feedback, vibration reduction is achieved, but the closed-loop pole corresponding to the coning mode is less stable than the open-loop. This result is duplicated in this work by constructing a plant $G_{\theta_{r0}}(\bar{s})$ for a rotor in hover with only rigid flapping modes. Using the dynamics presented in Chapter 2 and implementing the HHC

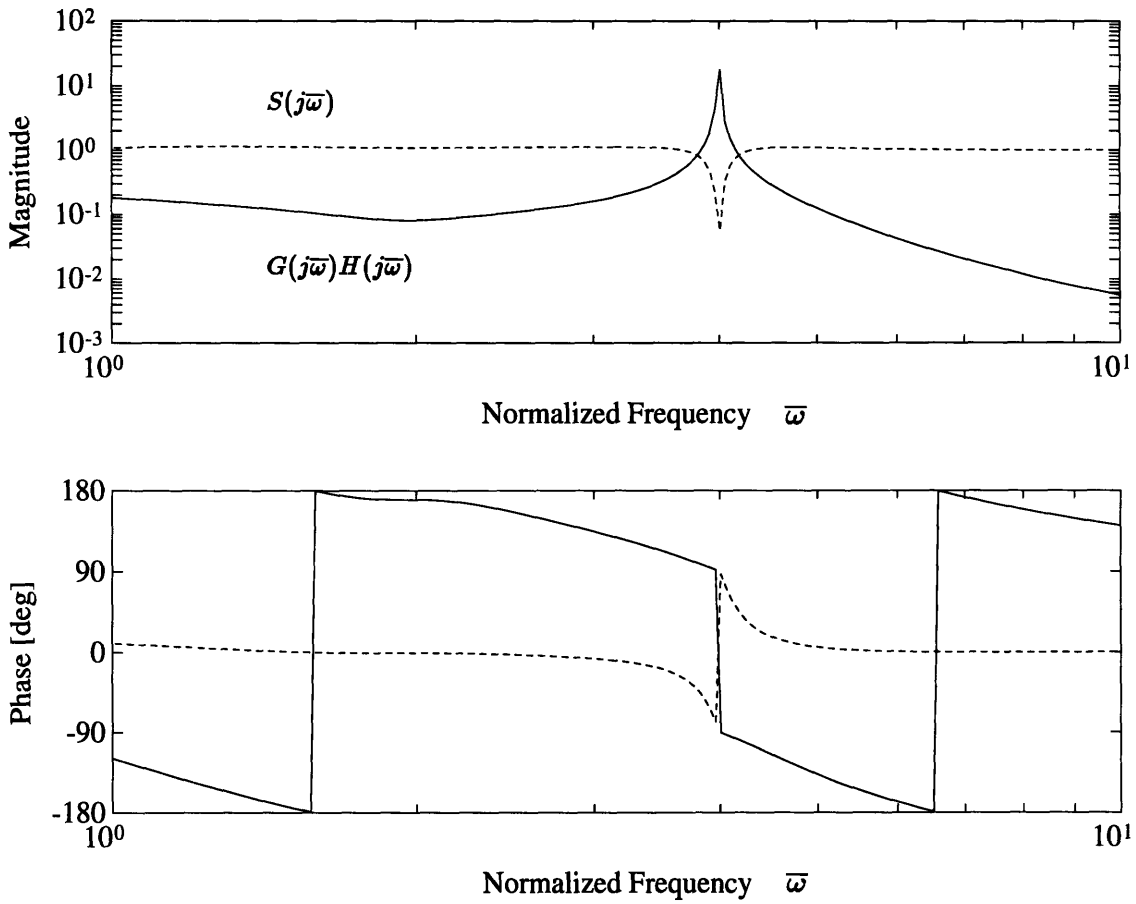


Figure 4-2: HHC loop and sensitivity transfer functions: servo-flap actuation.

compensator of Equation 4.21, the same stabilize effect is seen on the coning mode (see Figure 4-5, Case (a)). There is no change in the cyclic flapping modes, since longitudinal and lateral tilt are unobservable using only a vertical accelerometer and uncontrollable using only collective pitch commands in hover.

Of interest is the effect of HHC compensation on the fully defined rotor model including torsional motion and dynamic inflow. The open- and closed-loop poles for various $G_{\theta_{r_0}}(\bar{s})$ HHC systems in hover are presented in Figure 4-5. Case (a) is a rotor with rigid flapping only, corresponding to the DuVal rotor model. Case (b) is with rigid flapping and elastic torsion. Case (c) uses rigid flapping, elastic torsion, and aerodynamic torsional damping. Case (d) represents the full rotor model including dynamic inflow. These figures only present the upper half of the \bar{s} plane, since the poles are symmetric about the real axis. Note that all the plots show the closed

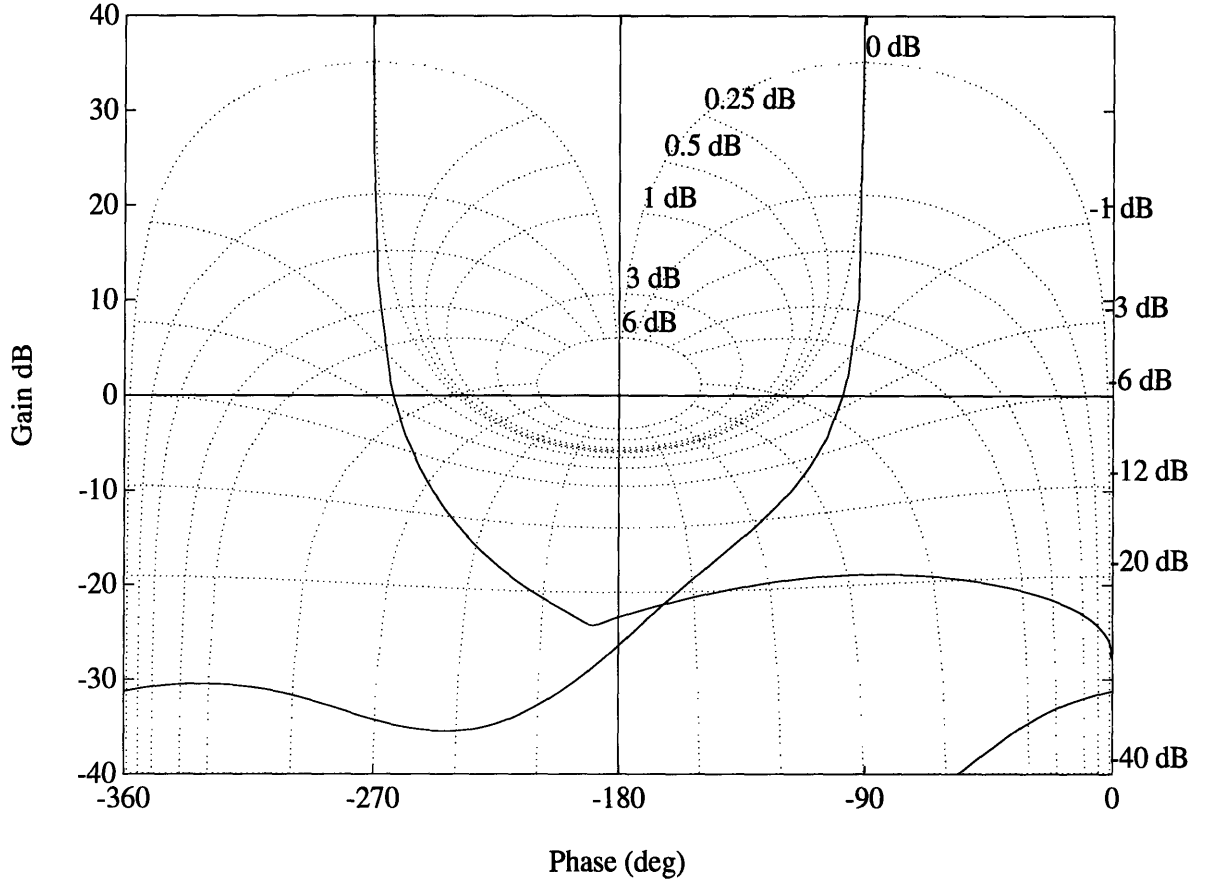


Figure 4-3: Nichols plot of HHC loop transfer function: root pitch actuation.

loop pole near $j\bar{\omega} = 4$ due to the HHC compensator. When the torsional degree of freedom is added in Case (b), the coning mode pole near $j\bar{\omega} = 1$ does not move right as in Case (a). Instead, it is the first torsional collective mode near $j\bar{\omega} = 4.5$ which becomes less stable. Since no aerodynamic or structural torsional damping was included for this Case (b), the first torsional mode moves into the right half plane, becoming unstable. Adding torsional damping in Case (c), remedies this instability, but highlights the importance of damping assumptions. Case (d) shows the same general behavior with the coning mode actually moving a small amount to the left. This is attributed to the additional aerodynamic “feedback” provided by the inflow model. The poles associated with inflow dynamics appear near the real axis. The collective inflow pole at $\bar{s} \approx -0.7$ moves slightly to the right. In addition, various $G_{\eta_0}(\bar{s})$ plants with servo-flap actuation were also evaluated and presented in Figure

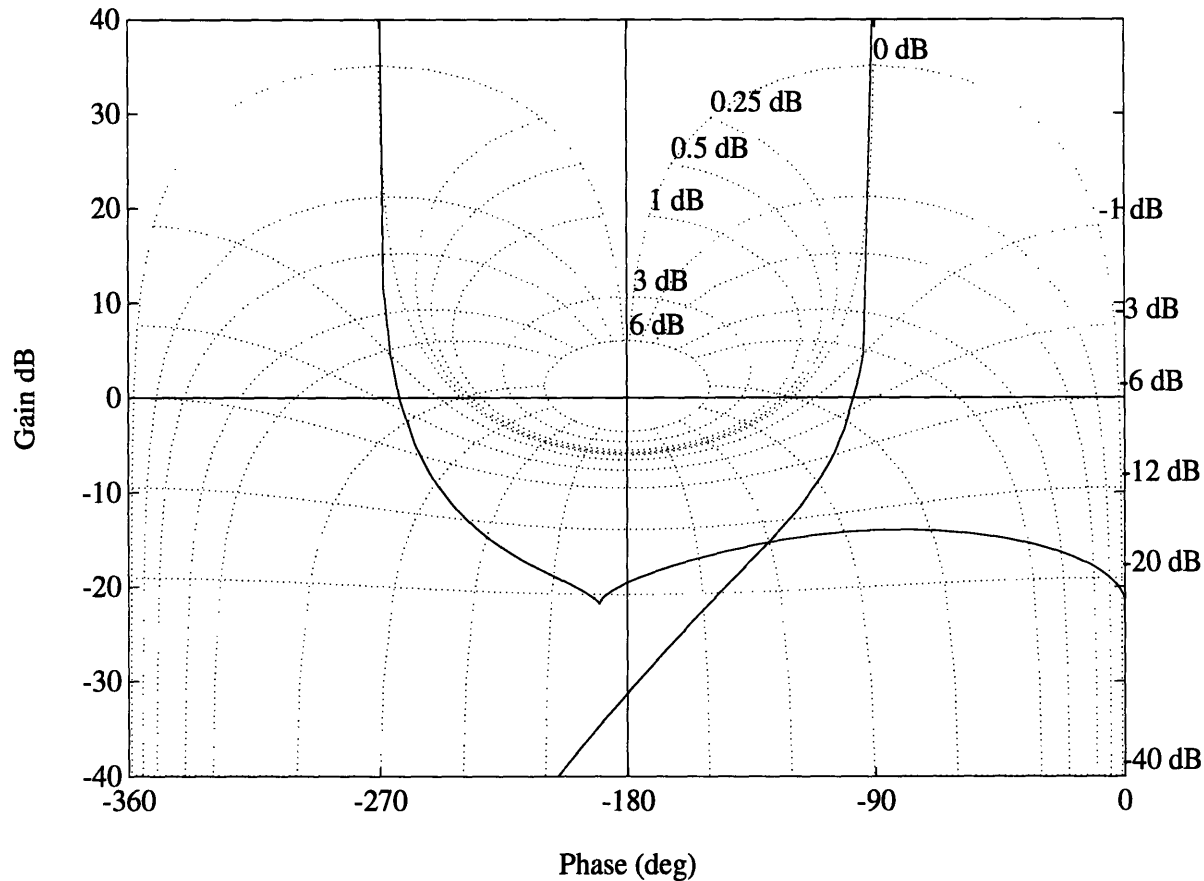


Figure 4-4: Nichols plot of HHC loop transfer function: servo-flap actuation.

4-6. The cases run were identical to the $G_{\theta_{r0}}(\bar{s})$ cases and provided similar results.

By using a simple second order compensator, the use of servo-flap actuation for closed-loop HHC has been evaluated and compared to the more traditional root pitch approach. It is evident from this work that there are no inherently serious limitations to using servo-flap for HHC, *i.e.*, non-minimum phase zeros near $N\Omega$. In fact, HHC performance characteristics using servo-flaps are nearly identical to the root pitch cases. This can be attributed to the robustness of the HHC algorithm. It was also found that the amount of aerodynamic damping has significant importance in maintaining closed-loop stability. Using only vertical acceleration feedback, a servo-flap HHC system can theoretically provide almost complete rejection of higher harmonic thrust disturbances but may decrease the damping of certain modes. It is predicted that the same results can be achieved on other disturbance components such as mo-

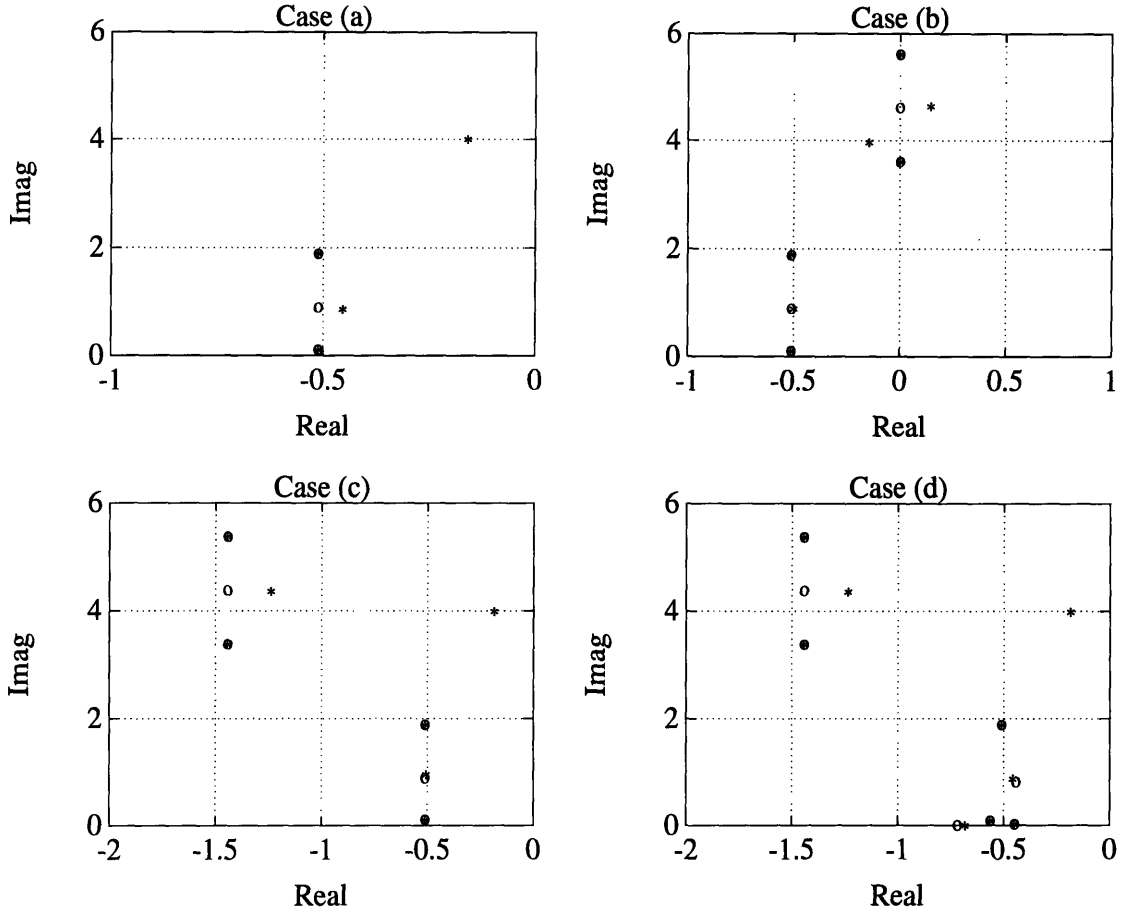


Figure 4-5: Open- and closed-loop poles for various $G_{\theta_{r0}}(\bar{s})$ HHC systems:
 \circ = open-loop pole, * = closed-loop pole.

ments and in-plane forces.

4.4 Multivariable HHC

In the previous sections, fundamental issues in implementing servo-flap HHC were demonstrated using SISO transfer functions and a simple second order compensator. Using the full state space model, one can demonstrate the effectiveness of multivariable control techniques for vibration reduction. In this section, the LQR/FSCF method proposed by Gupta and DuVal will be applied using collective and cyclic servo-flap inputs to minimize the sensitivity to thrust, pitching moment, and rolling moment disturbances. To accomplish this, the state space matrices will be modified to exclude root pitch dynamics and root pitch control inputs. Defining the state,

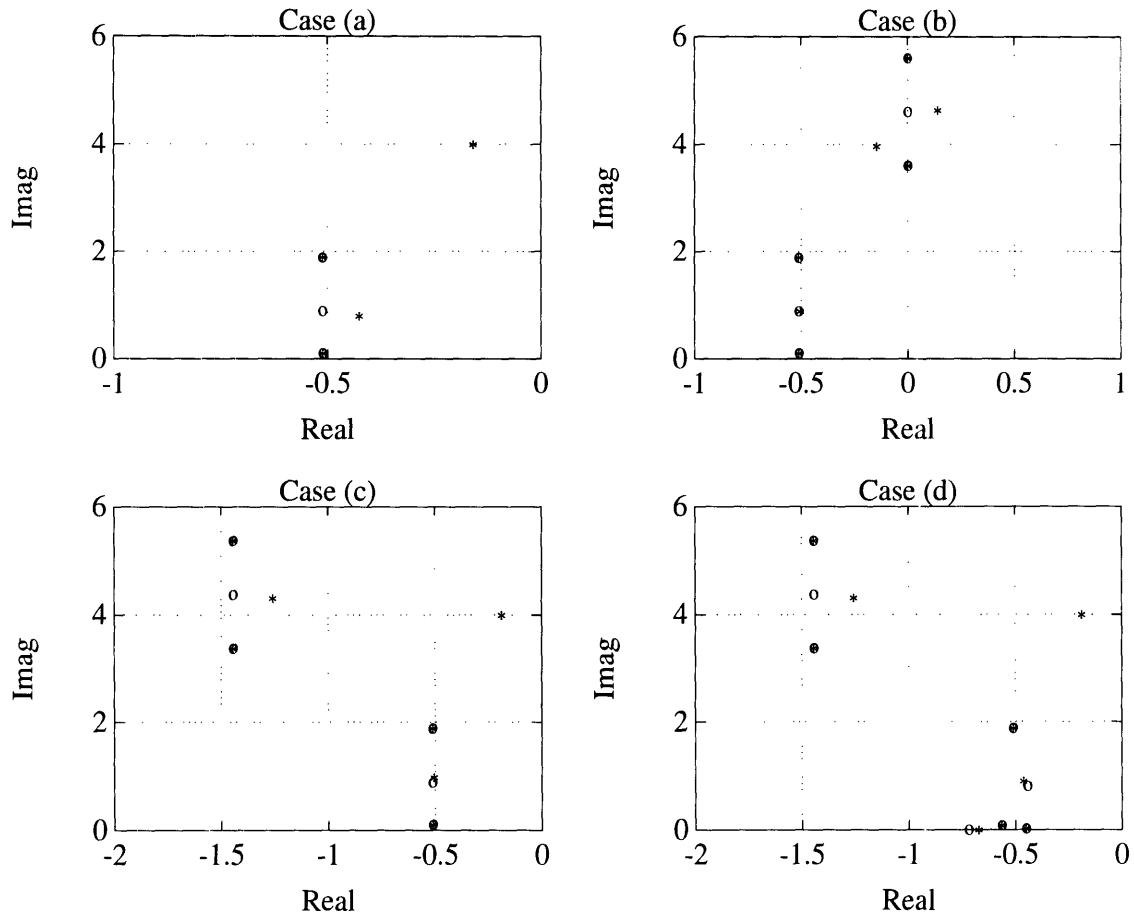


Figure 4-6: Open- and closed-loop poles for various $G_{\eta_0}(\bar{s})$ HHC systems:
 \circ = open-loop pole, $*$ = closed-loop pole.

control, and output vectors

$$\boldsymbol{x}_p = \begin{Bmatrix} z \\ \dot{z} \\ \lambda \end{Bmatrix}, \quad \boldsymbol{u}_p = \begin{Bmatrix} \eta_0 \\ \eta_c \\ \eta_s \end{Bmatrix}, \quad \boldsymbol{y}_p = \begin{Bmatrix} C_T \\ C_M \\ C_L \end{Bmatrix}, \quad (4.22)$$

the modified rotor plant is

$$\dot{\boldsymbol{x}}_p = \boldsymbol{A}_p \boldsymbol{x}_p + \boldsymbol{B}_p \boldsymbol{u}_p, \quad (4.23)$$

$$\boldsymbol{y}_p = \boldsymbol{C}_p \boldsymbol{x}_p + \boldsymbol{D}_p \boldsymbol{u}_p. \quad (4.24)$$

Using the normalized Laplace variable $\bar{s} = s/\Omega$, a filter of the form

$$G_n(\bar{s}) = \frac{N^2\bar{s}}{\bar{s}^2 + N^2} \quad (4.25)$$

will be appended to each of the vibration output channels to penalize disturbances at the $N\Omega$ frequency. The state space representation of all three filter dynamics is

$$\dot{\mathbf{x}}_n = \mathbf{A}_n \mathbf{x}_n + \mathbf{B}_n \mathbf{y}_p \quad (4.26)$$

$$\mathbf{y}_n = \mathbf{C}_n \mathbf{x}_n \quad (4.27)$$

The plant and filter dynamics can be combined so that

$$\begin{Bmatrix} \dot{\mathbf{x}}_p \\ \dot{\mathbf{x}}_n \end{Bmatrix} = \begin{bmatrix} \mathbf{A}_p & \mathbf{0} \\ \mathbf{B}_n \mathbf{A}_p & \mathbf{A}_n \end{bmatrix} \begin{Bmatrix} \mathbf{x}_p \\ \mathbf{x}_n \end{Bmatrix} + \begin{bmatrix} \mathbf{B}_p \\ \mathbf{B}_n \mathbf{D}_p \end{bmatrix} \{ \mathbf{u}_p \} , \quad (4.28)$$

$$\{ \mathbf{y}_n \} = \begin{bmatrix} \mathbf{0} & \mathbf{C}_n \end{bmatrix} \begin{Bmatrix} \mathbf{x}_p \\ \mathbf{x}_n \end{Bmatrix} , \quad (4.29)$$

which is rewritten as

$$\dot{\mathbf{x}} = \mathbf{A}\mathbf{x} + \mathbf{B}\mathbf{u} , \quad (4.30)$$

$$\mathbf{y} = \mathbf{C}\mathbf{x} . \quad (4.31)$$

The cost function J^* is to be minimized subject to Equation (4.30), the augmented dynamics, as a constraint. The quadratic cost function is

$$J^* = \lim_{T \rightarrow \infty} \frac{1}{2T} \int_0^T (\mathbf{x}^T \mathbf{Q} \mathbf{x} + \mathbf{u}^T \mathbf{R} \mathbf{u}) dt \quad (4.32)$$

where \mathbf{Q} is defined as

$$\mathbf{Q} = \mathbf{C}^T \mathbf{C} \quad (4.33)$$

and \mathbf{R} is defined as

$$\mathbf{R} = \frac{1}{\eta_{\max}^2} \begin{bmatrix} 1 & 0 & 0 \\ 0 & 1 & 0 \\ 0 & 0 & 1 \end{bmatrix} . \quad (4.34)$$

By minimizing this cost function, the sensitivity to output disturbances will be reduced significantly at $N\Omega$ and the servo-flap control commands will be limited by η_{\max} . By solving the algebraic Riccati equation,

$$\mathbf{K}\mathbf{A} + \mathbf{A}^T\mathbf{K} + \mathbf{Q} - \mathbf{K}\mathbf{B}\mathbf{R}^{-1}\mathbf{B}^T\mathbf{K} = \mathbf{0}, \quad (4.35)$$

the optimal control law

$$\mathbf{u} = -\mathbf{F}\mathbf{x}, \quad (4.36)$$

is obtained, where

$$\mathbf{F} = \mathbf{R}^{-1}\mathbf{B}^T\mathbf{K}. \quad (4.37)$$

The optimal control law can be rewritten as

$$\mathbf{u} = -\mathbf{F}_p\mathbf{x}_p - \mathbf{F}_n\mathbf{x}_n, \quad (4.38)$$

to separate the plant and filter state feedback signals. A block diagram of the resulting closed loop system is shown in Figure 4-7.

The LQR/FSCF method was applied to the H-34 rotor in moderate forward flight ($\mu = 0.15$) with the maximum servo-flap deflection, η_{\max} , limited to 10 deg. The singular value plot of the sensitivity transfer function matrix, which measures the sensitivity of the closed loop system to disturbances at the output, is presented in Figure 4-8. By augmenting the filter dynamics to the plant, a frequency weighted LQR solution which provides disturbance rejection centered at $\bar{\omega} = 4$ is obtained. The resulting sensitivity plot has quite a sharp notch at 4Ω . The width of this notch can be altered by modifying the filter transfer function $G_n(\bar{s})$.

Note that the resulting control law is a full state feedback solution. In general, the available feedback sensors are accelerometers mounted in the fuselage or possibly strain gauge sensors measuring hub loads. The actual rotor states themselves are difficult to measure or estimate. By measuring only fuselage states, vibration reduction can still be achieved, but this may result in a slightly less stable closed-loop system. This destabilizing effect was presented in [10] and was illustrated in the SISO

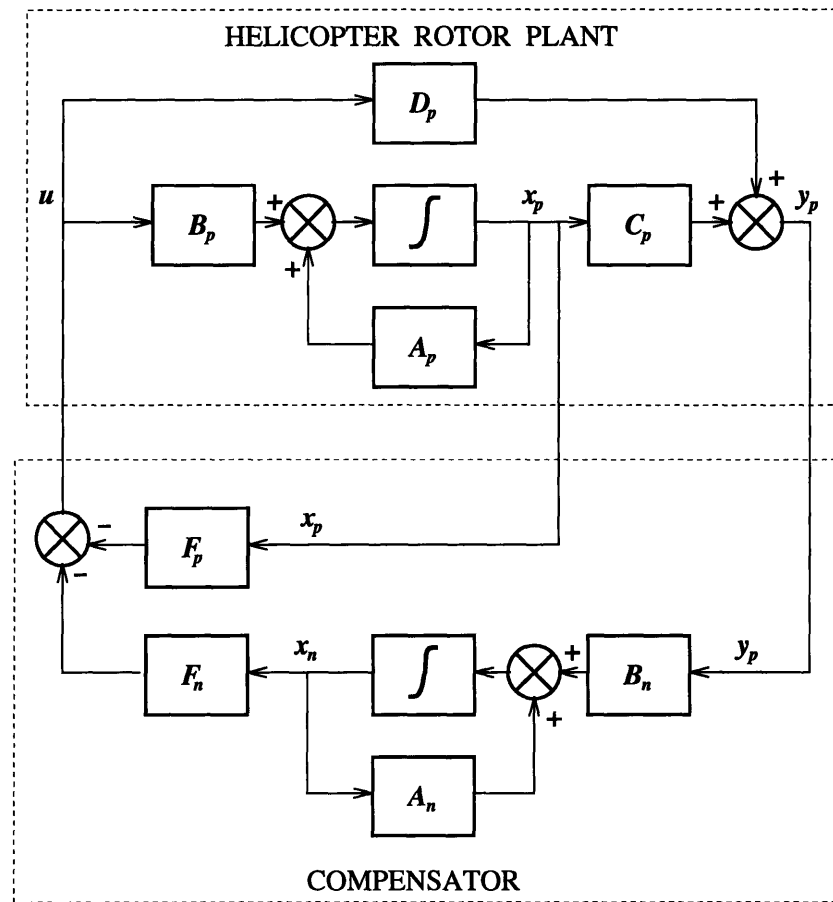


Figure 4-7: Block diagram of LQR/FSCF closed loop system.

examples of Section 4.3.

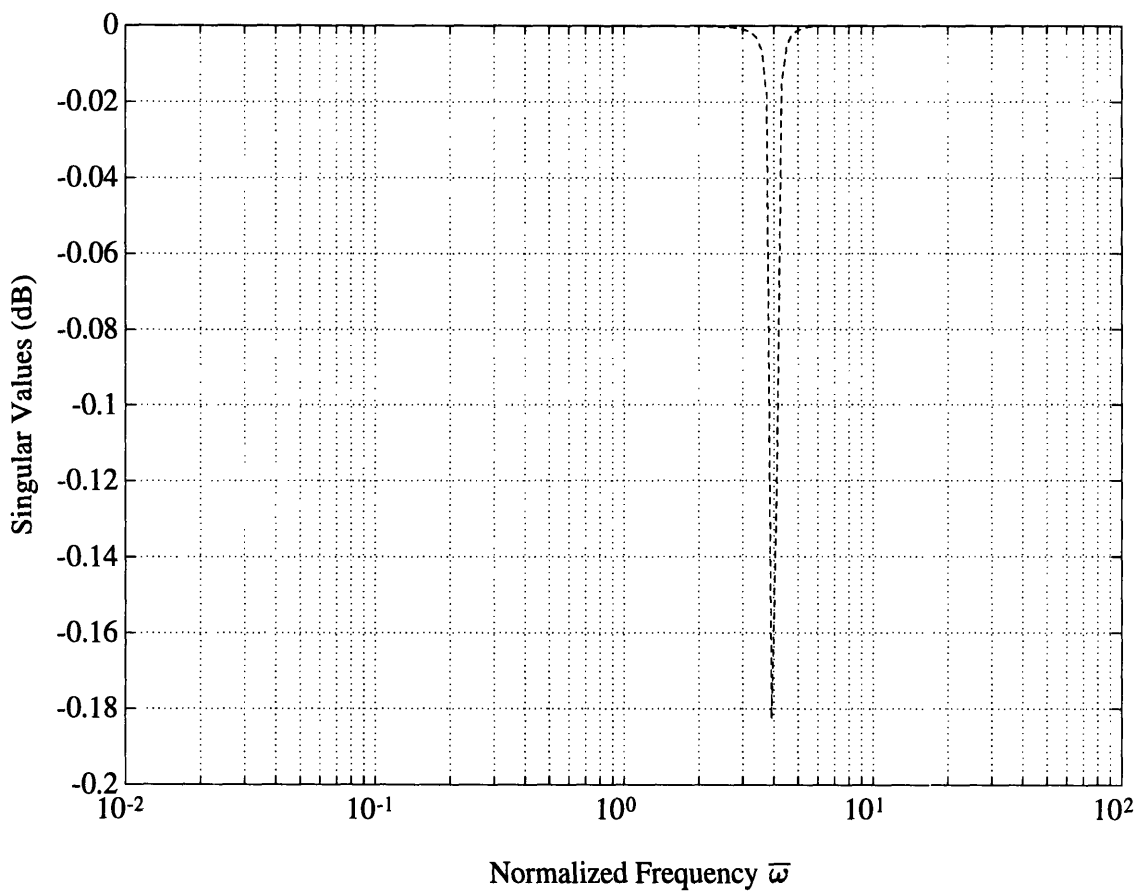


Figure 4-8: Singular value plot of sensitivity transfer function matrix. LQR/FSCF compensator applied to H-34 rotor plant in moderate forward flight.

Chapter 5

Conclusions

An LTI state space model of a smart rotor equipped with blade-mounted servo-flaps as well as conventional root pitch control has been presented. This rotor model features rigid blade flapping, elastic torsion using a modal approximation, and dynamic inflow. Any linear aerodynamic actuator can be incorporated into the model. The use of MBC transformations from the rotating to fixed frame yielded a constant coefficient approximation which neglects the periodic nature of the rotor dynamics. Parametric studies have been performed, and the application of servo-flaps to various rotor control concepts, particularly HHC for vibration reduction, has been evaluated.

5.1 Summary of Parametric Studies

The torsional stiffness study demonstrated the importance of this parameter to root pitch and servo-flap authority on the H-34 rotor. In general, root pitch thrust response is fairly insensitive to variations in torsional stiffness. At low frequencies, the rotor blades behave primarily as rigid bodies, so a torsionally stiff rotor is more desirable for root pitch actuation. In regards to servo-flap actuation, the torsional stiffness strongly influences the DC thrust response and the higher frequency dynamics. A torsionally soft blade improves collective servo-flap authority. Moving the rotor into forward flight increases the thrust response due to collective servo-flap actuation, particularly at 1Ω . The presence of the lateral tilt mode in forward flight reduces the

thrust response slightly at 2Ω . It was found that the baseline H-34 rotor was not a good candidate for servo-flap actuation, since this particular torsional stiffness puts the rotor blade very near the aileron reversal point. A rotor blade with a moderate first torsional frequency, $\bar{\omega}_1$, of 4.5 was defined for a typical smart rotor. A much softer blade could provide more authority but may encounter unreasonably large angles of attack.

Parametric studies involving chordwise c.g. offset and additional mass associated with blade-mounted actuators were performed using the modified H-34 rotor with $\bar{\omega}_1 = 4.5$. Increasing the c.g. offset improves thrust response authority while compromising stability. The additional mass and pitch inertia at the actuator locations does not have an adverse affect on authority, and actually provides a slight increase at the 1Ω response. Adding inertia, however, may increase the required control loads.

Spanwise placement of the actuator had a significant effect on servo-flap thrust authority, since the dynamic pressure is proportional to \bar{r}^2 . Moving the servo-flap from $\bar{r} = 0.5\text{--}0.7$ to $0.7\text{--}0.9$ increases the H-34 4Ω thrust response by almost 100%. For an effective servo-flap rotor system, the actuator must be placed far enough outboard to insure aileron reversal, but inboard of the tip region to avoid loss effects and higher aerodynamic hinge moments. A simplified aileron reversal study for a rotor in hover was conducted to define parameter ranges to guarantee rotor reversal. Based on this simplified analysis, placing a servo-flap outboard of the 50% span will guarantee aileron reversal for most typical rotors with $\bar{\omega}_1 = 4\text{--}6$.

5.2 Feasibility of Servo-flap Actuation for HHC

Using the state space model, the required servo-flap deflections and control loads for higher harmonic control can be determined. The main intent of this work was the application of piezo-electric driven servo-flaps, although other actuator designs can be evaluated. Using thin airfoil theory, the required hinge moment to provide 0.25 g of higher harmonic thrust authority using servo-flap actuation was calculated. This was compared with the required torque to feather the blade at $N\Omega$ and provide

the same amount of authority. Using the H-34 smart rotor as a baseline, servo-flap control loads were 2 orders of magnitude less than root pitch control loads in hover. In forward flight, servo-flap control loads increased significantly but remained well below the required root pitch torque.

Active rotor vibration reduction was demonstrated using HHC algorithms and both root pitch and servo-flap actuators. Using classical control techniques, SISO HHC systems with servo-flap actuators provided good disturbance rejection and exhibited gain margins of about 20 dB and phase margins of about 90 deg. Using a modified state space model, multivariable disturbance rejection was implemented using a frequency-weighted LQR technique. The control inputs were the collective and cyclic servo-flap commands, and the disturbances at the output were $N\Omega$ thrust, pitching moment, and rolling moment variations. An HHC system which uses only accelerometer feedback to measure hub loads can still provide good closed-loop performance, but may destabilize certain modes. Using HHC compensation techniques, a closed-loop servo-flap system exhibits good performance and robustness characteristics comparable to root pitch actuation. The servo-flap actuation scheme has no inherently serious limitations for HHC vibration reduction. Based on the benefits of lower control loads and higher bandwidth, piezoelectric servo-flaps are seen as a promising HHC actuator.

5.3 Further Research

This work has demonstrated the use of the state space smart rotor model for parametric studies and HHC applications. The modular nature of this code allows the various physical processes and properties to be separately analyzed. Aerodynamics, structural dynamics, and inflow dynamics are functionally separated. Other dynamics such as actuators, sensors, and disturbances can easily be incorporated into the state space format. The current configuration includes a single servo-flap surface, although a segmented servo-flap can easily be added to the model. The torsional dynamics could be altered to model a torsionally rigid blade with a soft torsional spring at the

root. Also, more extensive studies using a δ_3 hinge for flap/pitch coupling can be conducted. In its present form, the state space model represents a helicopter rotor plant whose outputs are the hub reactions. The output matrices could be modified to evaluate in-plane forces or rotor torque. By doing this, the rotor can be coupled to a fuselage model to obtain dynamics for an entire helicopter, or power requirements could be evaluated.

The main purpose of this rotor model is to identify the important design issues and parameters for various smart rotor applications. To accurately model airfoil behavior and compressibility effects, a more comprehensive aeroelastic rotor analysis routine such as C60 could be employed. By presenting an LTI state space rotor model with blade-mounted actuators, classical and multivariable control techniques can be used to investigate alternative concepts for rotor control.

Appendix A

Rotor Blade Integrals

The integrals evaluated along the rotor blade span, \bar{r} , are separated into aerodynamic and structural integrals. They are used in Chapter 2 to define the rotor blade dynamics, aerodynamic loads, and hub reactions.

A.1 Aerodynamic Integrals

$$\begin{aligned} A^n &= \int_{\bar{r}_1}^{\bar{r}_2} \bar{r}^n d\bar{r} \\ B^n &= \int_{\bar{r}_1}^{\bar{r}_2} (\bar{r} - \bar{e}) \bar{r}^n d\bar{r} \\ C_k^n &= \int_{\bar{r}_1}^{\bar{r}_2} \xi_{\theta_k}(\bar{r}) \bar{r}^n d\bar{r} \\ D^n &= \int_{\bar{r}_c}^B \bar{r}^n d\bar{r} \\ E^n &= \int_{\bar{r}_c}^B \xi_\beta(\bar{r}) \bar{r}^n d\bar{r} \\ F^n &= \int_{\bar{r}_c}^B \xi'_\beta(\bar{r}) \bar{r}^n d\bar{r} \\ G_k^n &= \int_{\bar{r}_c}^B \xi_{\theta_k}(\bar{r}) \bar{r}^n d\bar{r} \\ H_k^n &= \int_{\bar{r}_c}^B \xi_{\theta_k}^2(\bar{r}) \bar{r}^n d\bar{r} \\ J^n &= \int_{\bar{r}_c}^B (\bar{r} - \bar{e}) \bar{r}^n d\bar{r} \\ K^n &= \int_{\bar{r}_c}^B (\bar{r} - \bar{e}) \xi_\beta(\bar{r}) \bar{r}^n d\bar{r} \\ L^n &= \int_{\bar{r}_c}^B (\bar{r} - \bar{e}) \xi'_\beta(\bar{r}) \bar{r}^n d\bar{r} \\ M_k^n &= \int_{\bar{r}_c}^B (\bar{r} - \bar{e}) \xi_{\theta_k}(\bar{r}) \bar{r}^n d\bar{r} \end{aligned}$$

A.2 Structural Integrals

$$\begin{aligned}
I_b &= \int_0^R m r^2 dr \\
I_{\beta}^* &= \frac{1}{I_b} \int_e^R m(r - e)^2 dr \\
I_{\theta}^* &= \frac{1}{I_b} \int_e^R I_{\theta} dr \\
I_{\theta_k}^* &= \frac{1}{I_b} \int_e^R I_{\theta} \xi_{\theta_k}^2(r) dr \\
I_{\theta_k \theta_r}^* &= \frac{1}{I_b} \int_e^R I_{\theta} \xi_{\theta_k}(r) dr \\
I_{\theta_k \tilde{\beta}}^* &= \frac{1}{I_b} \int_e^R m x_{cg} \xi_{\theta_k}(r)(r - e) dr \\
I_{\theta_k \beta}^* &= \frac{1}{I_b} \int_e^R m x_{cg} \xi_{\theta_k}(r) r dr \\
I_{\beta \tilde{\theta}_r}^* &= \frac{1}{I_b} \int_e^R m x_{cg} (r - e) dr \\
I_{\beta \theta_r}^* &= \frac{1}{I_b} \int_e^R m x_{cg} r dr \\
m_{\tilde{\beta}}^* &= \frac{R}{I_b} \int_e^R m(r - e) dr \\
m_{\tilde{\theta}_r}^* &= \frac{R}{I_b} \int_e^R m x_{cg} dr \\
m_{\tilde{\theta}_k}^* &= \frac{R}{I_b} \int_e^R m x_{cg} \xi_{\theta_k}(r) dr
\end{aligned}$$

Appendix B

Matrices for Rotor Dynamics

This appendix defines the rotor dynamics matrices that were presented in Chapter 2. The matrices are functionally separated according to structural dynamics, aerodynamics, and hub reactions.

B.1 Structural Dynamics, Δ and Ψ Matrices

The blade dynamics matrices are divided into rigid flapping dynamics, elastic pitch dynamics, c.g. coupled dynamics, and root pitch inertial forcing terms. These matrices are used in Equation (2.56).

Rigid Flapping Dynamics

$$\Delta_{\beta\bar{\beta}} = I_{\beta}^* \begin{bmatrix} 1 & & \\ & 1 & \\ & & 1 \end{bmatrix}, \quad \Delta_{\beta\dot{\beta}} = I_{\beta}^* \begin{bmatrix} 0 & 0 & 0 \\ 0 & 0 & 2 \\ 0 & -2 & 0 \end{bmatrix}, \quad \Delta_{\beta\beta} = I_{\beta}^* \begin{bmatrix} \bar{\nu}_{\beta}^2 & & \\ & (\bar{\nu}_{\beta}^2 - 1) & \\ & & (\bar{\nu}_{\beta}^2 - 1) \end{bmatrix}.$$

Elastic Torsion Dynamics

$$\Delta_{\theta_k\bar{\theta}_k} = I_{\theta_k}^* \begin{bmatrix} 1 & & \\ & 1 & \\ & & 1 \end{bmatrix}, \quad \Delta_{\theta_k\dot{\theta}_k} = I_{\theta_k}^* \begin{bmatrix} 0 & 0 & 0 \\ 0 & 0 & 2 \\ 0 & -2 & 0 \end{bmatrix}, \quad \Delta_{\theta_k\theta_k} = I_{\theta_k}^* \begin{bmatrix} (\bar{\omega}_k^2 + 1) & & \\ & \bar{\omega}_k^2 & \\ & & \bar{\omega}_k^2 \end{bmatrix}.$$

C.G. Coupled Dynamics

$$\Delta_{\theta_k \tilde{\beta}} = -I_{\theta_k \tilde{\beta}}^* \begin{bmatrix} 1 & & \\ & 1 & \\ & & 1 \end{bmatrix}, \quad \Delta_{\theta_k \dot{\beta}} = I_{\theta_k \tilde{\beta}}^* \begin{bmatrix} 0 & 0 & 0 \\ 0 & 0 & -2 \\ 0 & 2 & 0 \end{bmatrix},$$

$$\Delta_{\theta_k \beta} = \begin{bmatrix} -I_{\theta_k \beta}^* & & \\ & (-I_{\theta_k \beta}^* + I_{\theta_k \tilde{\beta}}^*) & \\ & & (-I_{\theta_k \beta}^* + I_{\theta_k \tilde{\beta}}^*) \end{bmatrix}.$$

Root Pitch Actuation

$$\Psi_{\theta_k \theta_r} = -I_{\theta_k \theta_r}^* \begin{bmatrix} 1 & 0 & 0 \\ 0 & 0 & 0 \\ 0 & 0 & 0 \end{bmatrix}, \quad \Psi_{\theta_k \dot{\theta}_r} = -I_{\theta_k \theta_r}^* \begin{bmatrix} 0 & 0 & 0 \\ 0 & 0 & -2 \\ 0 & 2 & 0 \end{bmatrix}, \quad \Psi_{\theta_k \ddot{\theta}_r} = -I_{\theta_k \theta_r}^* \begin{bmatrix} 1 & & \\ & 1 & \\ & & 1 \end{bmatrix},$$

$$\Psi_{\beta \theta_r} = \begin{bmatrix} I_{\beta \theta_r}^* & & \\ & (I_{\beta \theta_r}^* - I_{\beta \tilde{\theta}_r}^*) & \\ & & (I_{\beta \theta_r}^* - I_{\beta \tilde{\theta}_r}^*) \end{bmatrix},$$

$$\Psi_{\beta \dot{\theta}_r} = I_{\beta \dot{\theta}_r}^* \begin{bmatrix} 0 & 0 & 0 \\ 0 & 0 & 2 \\ 0 & -2 & 0 \end{bmatrix}, \quad \Psi_{\beta \ddot{\theta}_r} = I_{\beta \ddot{\theta}_r}^* \begin{bmatrix} 1 & & \\ & 1 & \\ & & 1 \end{bmatrix}.$$

B.2 Aerodynamics, Λ Matrices

These matrices are used in Equation (2.87).

$$\boldsymbol{\Lambda}_{\theta_k \theta_k} = \gamma \begin{bmatrix} 0 & \frac{1}{32}\mu \bar{c}^2 H_k^0 & 0 \\ 0 & 0 & -\frac{1}{16}\bar{c}^2 H_k^1 \\ 0 & \frac{1}{16}\bar{c}^2 H_k^1 & 0 \end{bmatrix}, \quad \boldsymbol{\Lambda}_{\theta_k \dot{\theta}_k} = \gamma \begin{bmatrix} -\frac{1}{16}\bar{c}^2 H_k^1 & 0 & -\frac{1}{32}\mu \bar{c}^2 H_k^0 \\ 0 & -\frac{1}{16}\bar{c}^2 H_k^1 & 0 \\ -\frac{1}{16}\mu \bar{c}^2 H_k^0 & 0 & -\frac{1}{16}\bar{c}^2 H_k^1 \end{bmatrix},$$

$$\boldsymbol{\Lambda}_{\theta_k \eta} = \gamma \bar{p} \bar{c} \begin{bmatrix} (\frac{1}{4}\mu^2 C_k^0 + \frac{1}{2}C_k^2) & 0 & \frac{1}{2}\mu C_k^1 \\ 0 & (\frac{1}{8}\mu^2 C_k^0 + \frac{1}{2}C_k^2) & 0 \\ \mu C_k^1 & 0 & (\frac{3}{8}\mu^2 C_k^0 + \frac{1}{2}C_k^2) \end{bmatrix},$$

$$\boldsymbol{\Lambda}_{\beta \beta} = \gamma \begin{bmatrix} 0 & (\frac{1}{4}\mu K^0 - \frac{1}{4}\mu L^1) & 0 \\ -\frac{1}{2}\mu L^1 & 0 & (-\frac{1}{2}K^1 - \frac{1}{8}\mu^2 L^0) \\ 0 & (\frac{1}{2}K^1 - \frac{1}{8}\mu^2 L^0) & 0 \end{bmatrix},$$

$$\boldsymbol{\Lambda}_{\beta \theta_k} = \gamma \begin{bmatrix} (\frac{1}{4}\mu^2 M_k^0 + \frac{1}{2}M_k^2) & 0 & \frac{1}{2}\mu M_k^1 \\ 0 & (\frac{1}{8}\mu^2 M_k^0 + \frac{1}{2}M_k^2) & 0 \\ \mu M_k^1 & 0 & (\frac{3}{8}\mu^2 M_k^0 + \frac{1}{2}M_k^2) \end{bmatrix},$$

$$\boldsymbol{\Lambda}_{\beta \theta_r} = \gamma \begin{bmatrix} (\frac{1}{4}\mu^2 J^0 + \frac{1}{2}J^2) & 0 & \frac{1}{2}\mu J^1 \\ 0 & (\frac{1}{8}\mu^2 J^0 + \frac{1}{2}J^2) & 0 \\ \mu J^1 & 0 & (\frac{3}{8}\mu^2 J^0 + \frac{1}{2}J^2) \end{bmatrix},$$

$$\boldsymbol{\Lambda}_{\beta \dot{\beta}} = \gamma \begin{bmatrix} -\frac{1}{2}K^1 & 0 & -\frac{1}{4}\mu K^0 \\ 0 & -\frac{1}{2}K^1 & 0 \\ -\frac{1}{2}\mu K^0 & 0 & -\frac{1}{2}K^1 \end{bmatrix}, \quad \boldsymbol{\Lambda}_{\beta \lambda} = \gamma \begin{bmatrix} -\frac{1}{2}J^1 & 0 & -\frac{1}{4}\mu J^1 \\ 0 & -\frac{1}{2}J^2 & 0 \\ -\frac{1}{2}\mu J^0 & 0 & -\frac{1}{2}J^2 \end{bmatrix},$$

$$\boldsymbol{\Lambda}_{\beta \eta} = \gamma \bar{n} \begin{bmatrix} (\frac{1}{4}\mu^2 B^0 + \frac{1}{2}B^2) & 0 & \frac{1}{2}\mu B^1 \\ 0 & (\frac{1}{8}\mu^2 B^0 + \frac{1}{2}B^2) & 0 \\ \mu B^1 & 0 & (\frac{3}{8}\mu^2 B^0 + \frac{1}{2}B^2) \end{bmatrix}.$$

B.3 Hub Reactions, Γ and Φ Matrices

The hub reaction matrices are divided into aerodynamic and inertial terms. These matrices are used in Equations (2.108) and (2.109).

Aerodynamic Components Γ

$$\boldsymbol{\Gamma}_{\theta_k} = \sigma a \begin{bmatrix} \left(\frac{1}{4}\mu^2 G_k^0 + \frac{1}{2}G_k^2\right) & 0 & \frac{1}{2}\mu G_k^1 \\ 0 & \bar{e}\left(-\frac{1}{16}\mu^2 G_k^0 - \frac{1}{4}G_k^2\right) & 0 \\ \frac{1}{2}\bar{e}\mu G_k^1 & 0 & \bar{e}\left(\frac{3}{16}\mu^2 G_k^0 + \frac{1}{4}G_k^2\right) \end{bmatrix},$$

$$\boldsymbol{\Gamma}_{\theta_r} = \sigma a \begin{bmatrix} \left(\frac{1}{4}\mu^2 D^0 + \frac{1}{2}D^2\right) & 0 & \frac{1}{2}\mu D^1 \\ 0 & \bar{e}\left(-\frac{1}{16}\mu^2 D^0 - \frac{1}{4}D^2\right) & 0 \\ \frac{1}{2}\bar{e}\mu D^1 & 0 & \bar{e}\left(\frac{3}{16}\mu^2 D^0 + \frac{1}{4}D^2\right) \end{bmatrix},$$

$$\boldsymbol{\Gamma}_\beta = \sigma a \begin{bmatrix} 0 & \frac{1}{4}\mu(E^0 - F^0) & 0 \\ \frac{1}{4}\bar{e}\mu F^1 & 0 & \bar{e}\left(\frac{1}{4}E^1 + \frac{1}{16}\mu^2 F^0\right) \\ 0 & \bar{e}\left(\frac{1}{4}E^1 - \frac{1}{16}\mu^2 F^0\right) & 0 \end{bmatrix},$$

$$\boldsymbol{\Gamma}_{\dot{\beta}} = \sigma a \begin{bmatrix} -\frac{1}{2}E^1 & 0 & \frac{1}{8}\mu E^0 \\ 0 & \frac{1}{4}\bar{e}E^1 & 0 \\ -\frac{1}{4}\bar{e}\mu E^0 & 0 & -\frac{1}{4}\bar{e}E^1 \end{bmatrix}, \quad \boldsymbol{\Gamma}_\lambda = \sigma a \begin{bmatrix} -\frac{1}{2}D^1 & 0 & -\frac{1}{4}\mu D^1 \\ 0 & \frac{1}{4}\bar{e}D^2 & 0 \\ -\frac{1}{4}\bar{e}\mu D^0 & 0 & -\frac{1}{4}\bar{e}D^2 \end{bmatrix},$$

$$\boldsymbol{\Gamma}_\eta = \sigma n \begin{bmatrix} \frac{1}{4}\mu^2 A^0 + \frac{1}{2}A^2 & 0 & \frac{1}{4}\mu A^1 \\ 0 & \bar{e}\left(-\frac{1}{16}\mu^2 A^0 - \frac{1}{4}A^2\right) & 0 \\ \frac{1}{2}\bar{e}\mu A^1 & 0 & \bar{e}\left(\frac{3}{16}\mu^2 A^0 + \frac{1}{4}A^2\right) \end{bmatrix}.$$

Inertial Components Φ

$$\boldsymbol{\Phi}_{\theta_k} = \frac{\sigma a}{\gamma} \begin{bmatrix} 0 & 0 & 0 \\ 0 & \frac{1}{2}\bar{e}m_{\theta_k}^* & 0 \\ 0 & 0 & -\frac{1}{2}\bar{e}m_{\theta_k}^* \end{bmatrix}, \quad \boldsymbol{\Phi}_{\dot{\theta}_k} = \frac{\sigma a}{\gamma} \begin{bmatrix} 0 & 0 & 0 \\ 0 & 0 & \bar{e}m_{\theta_k}^* \\ 0 & -\bar{e}m_{\theta_k}^* & 0 \end{bmatrix},$$

$$\Phi_{\tilde{\theta}_k} = \frac{\sigma a}{\gamma} \begin{bmatrix} m_{\tilde{\theta}_k}^* & 0 & 0 \\ 0 & -\frac{1}{2}\bar{e}m_{\tilde{\theta}_k}^* & 0 \\ 0 & 0 & \frac{1}{2}\bar{e}m_{\tilde{\theta}_k}^* \end{bmatrix}, \quad \Phi_{\theta_r} = \frac{\sigma a}{\gamma} \begin{bmatrix} 0 & 0 & 0 \\ 0 & \frac{1}{2}\bar{e}m_{\tilde{\theta}_r}^* & 0 \\ 0 & 0 & -\frac{1}{2}\bar{e}m_{\tilde{\theta}_r}^* \end{bmatrix},$$

$$\Phi_{\dot{\theta}_r} = \frac{\sigma a}{\gamma} \begin{bmatrix} 0 & 0 & 0 \\ 0 & 0 & \bar{e}m_{\tilde{\theta}_r}^* \\ 0 & -\bar{e}m_{\tilde{\theta}_r}^* & 0 \end{bmatrix}, \quad \Phi_{\tilde{\theta}_r} = \frac{\sigma a}{\gamma} \begin{bmatrix} m_{\tilde{\theta}_r}^* & 0 & 0 \\ 0 & -\frac{1}{2}\bar{e}m_{\tilde{\theta}_r}^* & 0 \\ 0 & 0 & \frac{1}{2}\bar{e}m_{\tilde{\theta}_r}^* \end{bmatrix},$$

$$\Phi_{\beta} = \frac{\sigma a}{\gamma} \begin{bmatrix} 0 & 0 & 0 \\ 0 & -\frac{1}{2}\bar{\omega}_{\beta}^2 I_{\beta}^* - \frac{1}{2}\bar{e}m_{\tilde{\beta}}^* & 0 \\ 0 & 0 & \frac{1}{2}\bar{\omega}_{\beta}^2 I_{\beta}^* + \frac{1}{2}\bar{e}m_{\tilde{\beta}}^* \end{bmatrix},$$

$$\Phi_{\dot{\beta}} = \frac{\sigma a}{\gamma} \begin{bmatrix} 0 & 0 & 0 \\ 0 & 0 & \bar{e}m_{\tilde{\beta}}^* \\ 0 & \bar{e}m_{\tilde{\beta}}^* & 0 \end{bmatrix}, \quad \Phi_{\tilde{\beta}} = \frac{\sigma a}{\gamma} \begin{bmatrix} -m_{\tilde{\beta}}^* & 0 & 0 \\ 0 & \frac{1}{2}\bar{e}m_{\tilde{\beta}}^* & 0 \\ 0 & 0 & -\frac{1}{2}\bar{e}m_{\tilde{\beta}}^* \end{bmatrix}.$$

B.4 Coupled Dynamics Matrices

These matrices are defined for the coupled elastic pitch and rigid flapping dynamics. They are used to simplify the state space notation where

$$\mathbf{z} = \begin{Bmatrix} \boldsymbol{\theta}_k \\ \boldsymbol{\beta} \end{Bmatrix}.$$

These matrices appear in Tables 2.1 and 2.2.

$$\Delta_{z\ddot{z}} = \begin{bmatrix} \Delta_{\theta_k \ddot{\theta}_k} & \Delta_{\theta_k \ddot{\beta}} \\ \Delta_{\theta_k \ddot{\beta}} & \Delta_{\beta \ddot{\beta}} \end{bmatrix}, \quad \Delta_{z\dot{z}} = \begin{bmatrix} \Delta_{\theta_k \dot{\theta}_k} & \Delta_{\theta_k \dot{\beta}} \\ \Delta_{\theta_k \dot{\beta}} & \Delta_{\beta \dot{\beta}} \end{bmatrix}, \quad \Delta_{zz} = \begin{bmatrix} \Delta_{\theta_k \theta_k} & \Delta_{\theta_k \beta} \\ \Delta_{\theta_k \beta} & \Delta_{\beta \beta} \end{bmatrix},$$

$$\Psi_{z\theta_r} = \begin{bmatrix} \Psi_{\theta_k \theta_r} \\ \Psi_{\beta \theta_r} \end{bmatrix}, \quad \Psi_{z\dot{\theta}_r} = \begin{bmatrix} \Psi_{\theta_k \dot{\theta}_r} \\ \Psi_{\beta \dot{\theta}_r} \end{bmatrix}, \quad \Psi_{z\ddot{\theta}_r} = \begin{bmatrix} \Psi_{\theta_k \ddot{\theta}_r} \\ \Psi_{\beta \ddot{\theta}_r} \end{bmatrix}, \quad \Lambda_{zz} = \begin{bmatrix} \Lambda_{\theta_k \theta_k} & \mathbf{0} \\ \Lambda_{\beta \theta_k} & \Lambda_{\beta \beta} \end{bmatrix},$$

$$\Lambda_{z\dot{z}} = \begin{bmatrix} \Lambda_{\theta_k \dot{\theta}_k} & \mathbf{0} \\ \mathbf{0} & \Lambda_{\beta \dot{\beta}} \end{bmatrix}, \quad \Lambda_{z\theta_r} = \begin{bmatrix} \mathbf{0} \\ \Lambda_{\beta \theta_r} \end{bmatrix}, \quad \Lambda_{z\lambda} = \begin{bmatrix} \mathbf{0} \\ \Lambda_{\beta \lambda} \end{bmatrix}, \quad \Lambda_{z\eta} = \begin{bmatrix} \Lambda_{\theta_k \eta} \\ \Lambda_{\beta \eta} \end{bmatrix},$$

$$\Gamma_z = [\Gamma_{\theta_k} \ \Gamma_\beta], \quad \Gamma_{\dot{z}} = [\mathbf{0} \ \Gamma_{\dot{\beta}}],$$

$$\Phi_z = [\Phi_{\theta_k} \ \Phi_\beta], \quad \Phi_{\dot{z}} = [\Phi_{\dot{\theta}_k} \ \Phi_{\dot{\beta}}].$$

Appendix C

Inflow Dynamics

The inflow dynamics to be used in this model are based on that of Pitt and Peters [35]. The material in this appendix was previously presented in [12, Chapter 4]. It is a linear unsteady theory derived from actuator disk theory, that relates transient rotor loads to induced flow field response. The induced flow is expressed as

$$\lambda = \lambda_0 + \lambda_c \bar{r} \cos \psi + \lambda_s \bar{r} \sin \psi , \quad (\text{C.1})$$

where λ_0 , λ_c , and λ_s are the magnitudes of the uniform, fore-to-aft, and side-to-side variations in induced flow, respectively. The induced flow distributions are related to the perturbations in thrust, pitch moment, and roll moment by the linear first-order relation

$$[\mathbf{M}] \begin{Bmatrix} \dot{\lambda}_0 \\ \dot{\lambda}_c \\ \dot{\lambda}_s \end{Bmatrix} + [\mathbf{L}]^{-1} \begin{Bmatrix} \lambda_0 \\ \lambda_c \\ \lambda_s \end{Bmatrix} = \begin{Bmatrix} C_T \\ C_M \\ C_L \end{Bmatrix}_{\text{aero}} , \quad (\text{C.2})$$

where the x -axis is positive aft, the y -axis is positive starboard, and the z -axis is positive upward. (Note that the order and orientation of these loads differ slightly from that of Pitt and Peters.) The \mathbf{L} and \mathbf{M} matrices have been solved in closed form in Reference [35]. With appropriate modifications for the new orientation, the

\mathbf{L} and \mathbf{M} matrices are

$$\mathbf{L} = \frac{1}{v_P} \begin{bmatrix} \frac{1}{2} & \frac{15\pi}{64} \sqrt{\frac{1-\sin \alpha_d}{1+\sin \alpha_d}} & 0 \\ \frac{15\pi}{64} \sqrt{\frac{1-\sin \alpha_d}{1+\sin \alpha_d}} & \frac{-4 \sin \alpha_d}{1+\sin \alpha_d} & 0 \\ 0 & 0 & \frac{4}{1+\sin \alpha_d} \end{bmatrix}, \quad (\text{C.3})$$

$$\mathbf{M} = \begin{bmatrix} \frac{128}{75\pi} & 0 & 0 \\ 0 & \frac{-16}{45\pi} & 0 \\ 0 & 0 & \frac{16}{45\pi} \end{bmatrix}, \quad (\text{C.4})$$

respectively, where α_d is the angle of the rotor disk with respect to the free stream velocity. The mass flow parameter for the steady lift case is

$$v_P = \frac{\mu^2 + (\lambda_f + \lambda_i)(\lambda_f + 2\lambda_i)}{\sqrt{\mu^2 + (\lambda_f + \lambda_i)^2}}. \quad (\text{C.5})$$

If the helicopter is in axial flight, the induced inflow ratio may be approximated by momentum theory [19, pg. 52] as

$$\lambda_i = \frac{\lambda_c}{2} + \sqrt{\left(\frac{\lambda_c}{2}\right)^2 + \frac{C_T}{2}}, \quad (\text{C.6})$$

where λ_c is the vertical climb velocity. Note that in hover, $\lambda_c = 0$, and

$$\lambda_i = \sqrt{\frac{C_T}{2}}. \quad (\text{C.7})$$

If the helicopter is flying at some angle of incidence, then the induced inflow velocity is governed by the equations

$$\lambda_i = \frac{C_T}{2\sqrt{\mu^2 + \lambda^2}}, \quad (\text{C.8})$$

and

$$\lambda = \mu \tan \alpha_d + \lambda_i, \quad (\text{C.9})$$

which may be solved iteratively. If an initial inflow is assumed, so that

$$\lambda = \mu \tan \alpha_d + \frac{C_T}{2\sqrt{\mu^2 + \frac{C_T}{2}}} , \quad (\text{C.10})$$

the solution will converge after several iterations [19, pg. 61]. Pitt and Peters have shown that in axial flight, the inflow gains are identical to those obtained from simple momentum theory, and are independent of the radial lift distribution.

Appendix D

Listing of Matlab Code

The following is a listing of the Matlab *.m files which construct the State Space Rotor Model. These routines were originally written for Matlab Version 3.5. To create the state space matrices \mathbf{A} , \mathbf{B} , \mathbf{C} , and \mathbf{D} simply type `makemodel` at the Matlab prompt.

```

%=====
% makemodel.m
%=====

clear
clc

%===== Necessary model input files =====
generic      % Generic Rotor
%h34          % H-34 Rotor

%===== Main program =====
options       % Run Options

if lumpflag == 1,
twister      % Calculate Torsional Mode Shapes (lumped)
end

trapint      % Perform Blade Integrations (trapezoidal)
newmat       % Define Matrices
newstate     % Define State Matrices

```

```

%=====
% generic.m           input file for generic rotor model
%=====

%===== servoflap placement=====
r1bar = .65          % inboard servoflap location
r2bar = .85          % outboard servoflap location
%===== inputs =====
a = 5.73            % lift curve slope
alphad = 90          % rotor shaft angle (0 deg is edgewise flight)
                      % (90 deg is axial flight)
cbar = .08            % blade chord c/R
ebar = .05            % hinge offset
rcut = .05            % root cutout
Btip = 1.0            % tip loss factor
nbar=3.8388/a; % lift curve slope/a due to servoflap
pbar=-.6875/a; % moment curve slope/a due to servoflap
gamma = 8             % Lock number 8-10
mu = 0                % advance ratio
CTsig = .1             % blade loading
Q = 4                 % number of blades
wbeta = 0              % free blade flapping frequency
                      % sqrt(kbeta/(ibeta*Omega^2))

%===== other values calculated from inputs =====
alpha = alphad*pi/180;          % [radians]
mus= mu^2;                      % mu squared
cbars = cbar^2;                  % cbar squared
sigma = Q*cbar/pi               % solidity

```

```

Cthrust = sigma*CTsig % thrust coefficient

%===== velocity ratios =====
if (alphad==90) % Axial Flight
    vbar = mu; % free stream velocity ratio
    lamf = vbar; % free stream inflow ratio
    if (vbar==0) % Hover Case
        lami = sqrt(Cthrust/2); % induced velocity ratio
        lam = lamf + lami;
    else % Axial Vertical Flight
        lami = vbar/2 +sqrt((vbar/2)^2+Cthrust/2);
        lam = lamf + lami;
    end;
else % Forward Flight
    vbar = mu/cos(alpha); % free stream velocity ratio
    lamf = mu*tan(alpha); % free stream inflow ratio
    lamold = lamf + Cthrust/(2*sqrt(mus+Cthrust/2));
    error = 1;
% iterate to find inflow
    while abs(error) > .00001
        lami = Cthrust/(2*sqrt(mus+lamold^2));
        lam = lamf + lami;
        error = lam -lamold;
        lamold = lam;
    end
end

%=====
% specify DIMENSIONAL lumped parameters
% (same format as C60 input)

```

```

% UNITS: lumped pitch inertia = lumped mass*R^2
%=====
R = 12.5*12; % blade radius (inches)
omega_rpm = 476; % blade passage frequency (RPM)
omega = omega_rpm*2*pi/60; % blade passage frequency (radians)

%===== scale torsional stiffness =====
%GJ_scale = 0.3086; % place w_1 at 2.5/REV
%GJ_scale = 1.0000; % place w_1e at 4.5/REV
GJ_scale = 1.7778; % place w_1 at 6/REV
%GJ_scale = 2.0864; % place w_1 at 6.5/REV

%===== properties due to actuator=====
% These properties are incorporated at the actuator
% locations defined on the blade by the vector "act".
%
% 1 = actuator location
%
% 0 = no actuator
%=====

% cg is positive aft of 1/4 chord pitch axis
cg_scale = 1/12; % c.g./chord length
addmass = 0.0; % add mass at actuator locations
addIp = 0.0; % add pitch inertia at actuator locations

% rbounds mass_lump I_p_lump GJ act
% (N.D) (lb-sec^2/in) (lb-sec^2-in) (lb-in^2)
lumpy=...
[ 0.0500 3.0728e-03 1.5514e-02 8.5650e+05 0.0;
  0.1000 3.0728e-03 1.5514e-02 8.5650e+05 0.0;
  0.1500 3.0728e-03 1.5514e-02 8.5650e+05 0.0;
  0.2000 3.0728e-03 1.5514e-02 8.5650e+05 0.0;

```

0.2500	3.0728e-03	1.5514e-02	8.5650e+05	0.0;
0.3000	3.0728e-03	1.5514e-02	8.5650e+05	0.0;
0.3500	3.0728e-03	1.5514e-02	8.5650e+05	0.0;
0.4000	3.0728e-03	1.5514e-02	8.5650e+05	0.0;
0.4500	3.0728e-03	1.5514e-02	8.5650e+05	0.0;
0.5000	3.0728e-03	1.5514e-02	8.5650e+05	0.0;
0.5500	3.0728e-03	1.5514e-02	8.5650e+05	0.0;
0.6000	3.0728e-03	1.5514e-02	8.5650e+05	0.0;
0.6500	3.0728e-03	1.5514e-02	8.5650e+05	1.0;
0.7000	3.0728e-03	1.5514e-02	8.5650e+05	1.0;
0.7500	3.0728e-03	1.5514e-02	8.5650e+05	1.0;
0.8000	3.0728e-03	1.5514e-02	8.5650e+05	1.0;
0.8500	3.0728e-03	1.5514e-02	8.5650e+05	0.0;
0.9000	3.0728e-03	1.5514e-02	8.5650e+05	0.0;
0.9500	3.0728e-03	1.5514e-02	8.5650e+05	0.0;
1.0000	0.0	0.0	0.0	0.0];

```

[m,n] = size(lumpy);
N = m-1; %number of lumped masses
act = lumpy(1:N,5);
rbounds = lumpy(:,1);
mass_lump = lumpy(1:N,2) + addmass*act.*lumpy(1:N,2);
Ip_lump = lumpy(1:N,3) + addIp*act.*lumpy(1:N,3);
GJ = GJ_scale*lumpy(1:N,4);
cg = cg_scale*cbar*R*act;
% define positions of lumped masses (centered between boundaries)
rlump = (rbounds(2:m) + rbounds(1:m-1))/2;
nm = 3; % number of torsional modes
d3 = 0.0; % delta3 hinge angle (degrees)
Kp = tan(pi*d3/180); % delta3 coupling coefficient

```

```

%=====
% h34.m           input file for H-34 rotor model
%
%           based on C60 input deck 3/1/93
%=====

%===== servoflap placement=====
r1bar = 0.6000          % inboard servoflap location
r2bar = 0.8000          % outboard servoflap location
%===== inputs =====
a = 6.3025      % lift curve slope
alphad = 90.0    % rotor shaft angle (0 deg is edgewise flight)
%                               (90 deg is axial flight)
cbar = (16.4/12)/28    % blade chord c/R
ebar = .0357    % hinge offset
rcut = .2100    % root cutout
Btip = 1;        % tip loss factor
nbar = .5        % 20% flap values from X-foil; Re=4,080,000
pbar = -.082
gamma = 8.1125 % Locke number 8-10
mu = 0.0        % advance ratio
CTsig = .1      % blade loading
Q = 4           % number of blades
wbeta = 0       % free blade flapping frequency
%   sqrt(kbeta/(ibeta*Omega^2))

%===== other values calculated from inputs =====
alpha = alphad*pi/180;          % [radians]
mus= mu^2;                      % mu squared
cbars = cbar^2;                 % cbar squared
sigma = Q*cbar/pi               % solidity

```

```

Cthrust = sigma*CTsig           % thrust coefficient

%===== velocity ratios =====
if (alphad==90)                 % Axial Flight
vbar = mu;                      % free stream velocity ratio
lamf = vbar;                     % free stream inflow ratio
if (vbar==0)                     % Hover Case
lami = sqrt(Cthrust/2);         % induced velocity ratio
lam = lamf + lami;
else                            % Axial Vertical Flight
lami = vbar/2 +sqrt((vbar/2)^2+Cthrust/2);
lam = lamf + lami;
end;

else                            % Forward Flight
vbar = mu/cos(alpha);          % free stream velocity ratio
lamf = mu*tan(alpha);          % free stream inflow ratio
lamold = lamf + Cthrust/(2*sqrt(mus+Cthrust/2));
error = 1;

% iterate to find inflow
while abs(error) > .00001
lami = Cthrust/(2*sqrt(mus+lamold^2));
lam = lamf + lami;
error = lam -lamold;
lamold = lam;
end
end

%=====
% specify DIMENSIONAL lumped parameters
% (same format as C60 input)

```

```

% UNITS: lumped pitch inertia = lumped mass*R^2
%=====
R = 28*12;      %inches
omega_rpm = 222;
omega = omega_rpm*2*pi/60;
%GJ_scale = 0.1068 % place w_1 at 2.5/REV
GJ_scale = 0.3463; % place w_1 at 4.5/REV
%GJ_scale = 0.5
%GJ_scale = 1.0000; % place w_1 at 7.65/REV
%GJ_scale = (7.75/7.65)^2; %

%===== properties due to actuator=====
% These properties are incorporated at the actuator
% locations defined on the blade by the vector "act".
%     1 = actuator location
%     0 = no actuator
%=====
% cg is positive aft of 1/4 chord pitch axis
cg_scale = 0.0; % c.g./chord length
addmass = 0.0;   % additional mass due to actuator
addIp = 0.0;    % additional pitch inertia due to actuator

% rbounds mass_lump          Ip_lump        GJ           act
% (N.D)  (lb-sec^2/in)       (lb-sec^2-in)   (lb-in^2)
lumpy=
[ 0.0357  7.8258e-04      9.0132e-03      1.1900e+08      0.0;
  0.0358  3.0965e-01      1.9541          1.1900e+08      0.0;
  0.0900  3.5839e-02      2.3840e-01      5.8712e+07      0.0;
  0.1300  1.2319e-02      8.9600e-02      2.4891e+07      0.0;

```

0.1700	1.3913e-02	1.4784e-01	2.0566e+07	0.0;
0.2100	2.3644e-02	2.7254e-01	1.8960e+07	0.0;
0.2700	2.3913e-02	2.7720e-01	1.8000e+07	0.0;
0.3250	2.1739e-02	2.5200e-01	1.8000e+07	0.0;
0.3750	2.1739e-02	2.5200e-01	1.8000e+07	0.0;
0.4250	2.1739e-02	2.5200e-01	1.8000e+07	0.0;
0.4750	2.1739e-02	2.5200e-01	1.8000e+07	0.0;
0.5250	2.1739e-02	2.5200e-01	1.8000e+07	0.0;
0.5750	2.1739e-02	2.5200e-01	1.8000e+07	0.0;
0.6250	2.3913e-02	2.7720e-01	1.8000e+07	1.0;
0.6800	2.1739e-02	2.5200e-01	1.8000e+07	1.0;
0.7300	1.7391e-02	2.0160e-01	1.8000e+07	1.0;
0.7700	1.5217e-02	1.7640e-01	1.8000e+07	1.0;
0.8050	1.4130e-02	1.6380e-01	1.8000e+07	1.0;
0.8375	1.0869e-02	1.2600e-01	1.8000e+07	1.0;
0.8625	1.0870e-02	1.2600e-01	1.8000e+07	0.0;
0.8875	1.0869e-02	1.2600e-01	1.8000e+07	0.0;
0.9125	1.1956e-02	1.3860e-01	1.8000e+07	0.0;
0.9400	1.0683e-02	1.0080e-01	1.8000e+07	0.0;
0.9600	1.3913e-02	1.6416e-01	1.8000e+07	0.0;
0.9800	8.4269e-03	1.4545e-01	1.8000e+07	0.0;
1.0000	0.0	0.0	0.0	0.0];

```
[m,n] = size(lumpy);
N = m-1; %number of lumped masses
rbounds = lumpy(:,1);
act = lumpy(1:N,5);
mass_lump = lumpy(1:N,2) + addmass*act.*lumpy(1:N,2);
Ip_lump = lumpy(1:N,3) + addIp*act.*lumpy(1:N,3);
GJ = GJ_scale*lumpy(1:N,4);
```

```

cg = cg_scale*16.4*lumpy(1:N,5);
% define positions of lumped masses (centered between boundaries)
rlump = (rbounds(2:m) + rbounds(1:m-1))/2;
nm = 3; %number of modes = nm
nm = 3; % number of torsional modes
d3 = 0.0; % delta3 hinge angle (degrees)
Kp = tan(pi*d3/180); % delta3 coupling coefficient

% check Locke number
Ib = sum(mass_lump.*((R*rlump).^2)/12); %slug-ft^2
gamma = 0.002195*a*(cbar)*(R/12)^5/Ib

```

```
%=====
% options.m          set rotor model options
%=====

% set rotor model options

inflag = 1;           % 0 = no inflow,      1 = peters inflow
dampflag = 1;          % 0 = no damping,     1 = damping
flapflag = 1;          % 0 = no flapping,    1 = flapping
mode1flag = 1;          % 0 = no 1st torsion, 1 = 1st torsion
mode2flag = 1;          % 0 = no 2nd torsion, 1 = 2nd torsion
d3fflag = 0;           % 0 = no delta3 hinge, 1 = delta3 hinge
lumpflag = 1;           % 1 = use lumped parameters
```

```

%=====
% twister.m          calculate torsional modes
%=====

% calculate torsional modes of lumped parameter system
% required vectors: GJ,Ip_lump,rbounds,R,omega
% BEWARE OF UNITS! GJ, Ip, and R must be consistent
%=====

% define lumped stiffness vector from k(i) = GJ(i)/klength(i)
klength(1,1) = R*(rlump(1) - rbounds(1));
for i = 2:N;
klength(i,1) = R*(rlump(i)-rlump(i-1));
end
k = GJ./klength;

%define stiffness and mass matrices for torsional system
%           [K]           [M]
for i = 1:N,
M(i,i) = Ip_lump(i);
end

K(1,1) = k(1) + k(2);
K(1,2) = -1*k(2);

for i = 2:N-1,
K(i,i-1) = -1*k(i);
K(i,i) = k(i) + k(i+1);
K(i,i+1) = -1*k(i+1);

```

```

end

K(N,N-1) = -1*k(N-1);
K(N,N) = k(N);

% solve generalized eigenvalue problem
[V1,D1] = eig(K,M);

% sort modes and natural frequencies
for i = 1:N;
wks(1,i) = D1(i,i);
end

[wks,index] = sort(wks);
wk = (sqrt(wks)/omega)';
wk = wk(1:nm);
for k = 1:nm,
tmodes(:,k) = V1(:,index(k))/V1(N,index(k));
end

clear K M k m n  klength natfreq index V1 D1

```

```

%=====
% trapint.m      trapezoidal integration
%=====
% evaluate structural and aerodynamic rotor blade integrals
%=====

%=====
%   EVALUATE STRUCTURAL INTEGRALS
%=====

% non-dimensionalized by Ib

% define vectors:

% massvec: sectional mass

% Ipvec : sectional pitch inertia

% R      : blade radius

% cgvec : center of gravity offset

% units must be consistent: mass*R^2/Ip = non-dim.

%           cg/R = non-dim.

%=====

numpts=(1-ebar)*1000+1;          % ebar=.05 numpts=951
dr = (1-ebar)/(numpts-1);
sumvec = [.5 ones(1,(numpts-2)) .5];
rbar=ebar*ones(numpts,1)+(1-ebar)*(0:(numpts-1))/(numpts-1);
ebarvec = ebar*ones((rbar));
rme = rbar-ebarvec;
flap = rbar-ebarvec;
dflap = ones((rbar));

%=====

```

```

% CONVERT LUMPED PARAMETERS TO DISTRIBUTED VECTORS
%=====
%
% This routine is currently set up to take in
% lumped properties defined in the model input file
% and the lumped mode shapes defined by routine twister.m.
%
% To use distributed properties, simply define the
% the vectors Ipvec, massvec, cgvec and set option lumpflag = 0.
%
% To use different mode shapes, define matrix twist(i,j)
% and set option lumpflag = 0.
%
% where "i" corresponds to mode number,
%       "j" corresponds to radial station.
%=====

if lumpflag == 1,

    % convert lumped mode shapes to distributed vector
    for k = 1:nm,
        twist(:,k) = span(tmodes(:,k),rbounds(1:N),numpts,ebar);
    end

    % convert lumped input parameters to sectional values
    Ip_dist = lump2dist(Ip_lump,rbounds,R);
    mass_dist = lump2dist(mass_lump, rbounds,R);

    % convert properties to same size vector for sumvec
    % (properties assumed constant between rbounds)
    Ipvec = span(Ip_dist,rbounds(1:N),numpts,ebar);
    massvec = span(mass_dist,rbounds(1:N),numpts,ebar);
    cgvec = span(cg,rbounds(1:N),numpts,ebar);

```

```

end

ibee = R^3*dr*sumvec*(massvec.*rbar.*rbar);
ibets = R^3*dr*sumvec*(rme.*rme.*massvec)/ibee;

for k = 1:nm,
    itkrs(k) = R*dr*sumvec*(twist(:,k).*Ipvec)/ibee;
    itks(k) = R*dr*sumvec*(twist(:,k).*twist(:,k).*Ipvec)/ibee;
% C.G. offset coupling terms
    ibtks(k) = R^2*dr*sumvec*(rbar.*twist(:,k).*massvec.*cgvec)/ibee;
    ibddtks(k) = R^2*dr*sumvec*(cgvec.*rme.*twist(:,k).*massvec)/ibee;
% inertial forcing terms for Hub Reactions
    Mtks(k) = R^2*dr*sumvec*(twist(:,k).*cgvec.*massvec)/ibee;
end

% C.G. offset coupling terms
ibthrs = R^2*dr*sumvec*(cgvec.*rbar.*massvec)/ibee;
ibddthrs = R^2*dr*sumvec*(cgvec.*rme.*massvec)/ibee;

% inertial forcing terms for Hub Reactions
Mbs = R^3*dr*sumvec*(rme.*massvec)/ibee;
Mtrs = R^2*dr*sumvec*(cgvec.*massvec)/ibee;

% evaluate non-dimensional flapping frequency
nubeta = sqrt(1-wbeta^2+...
    ((R^3*dr*sumvec*(rme.*ebarvec.*massvec))/ibee)/ibets);

%=====
% EVALUATE AERODYNAMIC INTEGRALS
%=====

```

```

rcutind = (rcut - ebar)*numpts/(1-ebar) + 1;
Bind = (Btip - ebar)*numpts/(1-ebar);
sumveca = [.5 sumvec(rcutind+1:Bind-1) .5];
rbara=rbar(rcutind:Bind);
ebarveca = ebarvec(rcutind:Bind);
rmea = rme(rcutind:Bind);
flapa = flap(rcutind:Bind);
dflapa = dflap(rcutind:Bind);

for k = 1:nm,
%    twist(:,k) = (-1)^(k+1)*sin( ( (2*k-1)*pi/(2*(1-ebar)) ) *rme);
    atwist = twist(rcutind:Bind,k);
    G0(k) = dr*sumveca*(atwist);
    G1(k) = dr*sumveca*(atwist.*rbara);
    G2(k) = dr*sumveca*(atwist.*rbara.^2);
    G3(k) = dr*sumveca*(atwist.*rbara.^3);
    H0(k) = dr*sumveca*(atwist.*atwist);
    H1(k) = dr*sumveca*(atwist.*atwist.*rbara);
    M0(k) = dr*sumveca*(rmea.*atwist);
    M1(k) = dr*sumveca*(rmea.*atwist.*rbara);
    M2(k) = dr*sumveca*(rmea.*atwist.*rbara.^2);
end

%=====
D0 = dr*sumveca*(ones((rbara)));
D1 = dr*sumveca*(rbara);
D2 = dr*sumveca*(rbara.^2);
D3 = dr*sumveca*(rbara.^3);
%=====

```

```

E0 = dr*sumveca*(flapa);
E1 = dr*sumveca*(flapa.*rbara);
E2 = dr*sumveca*(flapa.*rbara.^2);
%=====
F0 = dr*sumveca*(dflapa);
F1 = dr*sumveca*(dflapa.*rbara);
F2 = dr*sumveca*(dflapa.*rbara.^2);
F3 = dr*sumveca*(dflapa.*rbara.^3);
%=====
J0 = dr*sumveca*(rmea);
J1 = dr*sumveca*(rmea.*rbara);
J2 = dr*sumveca*(rmea.*rbara.^2);
%=====
K0 = dr*sumveca*(rmea.*flapa);
K1 = dr*sumveca*(rmea.*flapa.*rbara);
%=====
L0 = dr*sumveca*(rmea.*dflapa);
L1 = dr*sumveca*(rmea.*dflapa.*rbara);
L2 = dr*sumveca*(rmea.*dflapa.*rbara.^2);

%=====
% EVALUATE SERVO-FLAP INTEGRALS
%=====

r1indx=round((r1bar-ebar)*1000+1);
r2indx=round((r2bar-ebar)*1000+1);

% check if outboard flap location is in tip loss region
if r2indx > Bind,
    r2indx = Bind;

```

```

end

sfrbar= rbar(r1indx:r2indx,1);
sfnumpts = r2indx-r1indx+1;
sfsumvec = [.5 ones(1,(sfnumpts-2)) .5];
sfebarvec= ebarvec(r1indx:r2indx,1);
sfrm= rme(r1indx:r2indx,1);
sfflap = flap(r1indx:r2indx,1);
sfdflap = dflap(r1indx:r2indx,1);

for k = 1:nm,
    sftwist(:,k) = twist(r1indx:r2indx,k);
    C0(k) = dr*sfsumvec*(sftwist(:,k));
    C1(k) = dr*sfsumvec*(sftwist(:,k).*sfrbar);
    C2(k) = dr*sfsumvec*(sftwist(:,k).*sfrbar.*sfrbar);
end

%=====
A0 = dr*sfsumvec*(ones((sfrbar)));
A1 = dr*sfsumvec*(sfrbar);
A2 = dr*sfsumvec*(sfrbar.*sfrbar);
A3 = dr*sfsumvec*(sfrbar.*sfrbar.*sfrbar);
%=====

B0 = dr*sfsumvec*(sfrm);
B1 = dr*sfsumvec*(sfrm.*sfrbar);
B2 = dr*sfsumvec*(sfrm.*sfrbar.*sfrbar);
B3 = dr*sfsumvec*(sfrm.*sfrbar.*sfrbar.*sfrbar);

clear numpts ebarvec rme flap dflap

```

```
clear r1indx r2indx sfrbar sfnumpts sfsumvec sfbarvec  
clear sfrmef sfflap sfdflap sftwist1 sftwist2  
clear massvec Ipvec N
```

```
%=====
% lump2dist.m
%=====
% this function converts a lumped property vector (lump) to
% a distributed property vector (dist) of the same size
% indexed from inboard out
%=====

function [dist] = lump2dist(lump,rbounds,R)

[m,n] = size(rbounds);

dr = R*(rbounds(2:m) - rbounds(1:m-1));
dist = lump./dr;
```

```

%=====
% span.m
%=====

% this function converts a spanwise distribution into a
% discretized vector for use with the numerical integration
% trapint.m properties are assumed to be constant between rbounds.

%=====

function [spanout] = span(spanin,rspan,numpts,ebar)

% spanin is the span varying property
% rspan is the radial station.
% radial station vector starts from inboard and goes out

[m,n] = size(spanin);

spanout = zeros(numpts,1);

k1 = round(((rspan(1)-ebar)/(1-ebar))*numpts)+1;
k2 = round(((rspan(2)-ebar)/(1-ebar))*numpts);

for j = k1:k2;
spanout(j) = spanin(1);
end

for i = 2:m-1;
k1 = k2+1;
k2 = round(((rspan(i+1)-ebar)/(1-ebar))*numpts);
for j = k1:k2;

```

```
spanout(j) = spanin(i);  
end  
end
```

```
for j = k2+1:numpts;  
spanout(j) = spanin(m);  
end
```

```

%=====
% newmat.m      define dynamics matrices
%=====

% define new matrices for rotor state space
%
% matrix names
%
%   D = Delta
%
%   P = Psi
%
%   L = Lambda
%
%   Ph = Phi

% subscript definitions
%
%   b = beta
%
%   tk = theta_k
%
%   l = lambda
%
%   e = eta
%
%   bd = beta dot
%
%   bdd = beta double dot
%
%   and so on...
%
%=====

%=====

%      Rigid Pitch Forcing (Psi) Matrices
%
% includes inertial forcing plus propeller moment
%=====

%    DEFINE TORSIONAL MODE FORCING

for k = 1:nm,
  P_ztr((3*k-2):3*k,1:3) = -itkrs(k)*[1 0 0;0 0 0;0 0 0];
  P_ztrd((3*k-2):3*k,1:3) = -itkrs(k)*[0 0 0;0 0 2;0 -2 0];

```

```

P_ztrdd((3*k-2):3*k,1:3) = -itkrs(k)*eye(3,3);

end

%   DEFINE RIGID FLAPPING FORCING (DUE TO C.G. OFFSET)
P_ztr((3*nm+1):(3*nm+3),1:3) = [ibthrs 0 0;
                                     0 ibthrs-ibddthrs 0;
                                     0 0 ibthrs-ibddthrs];
P_ztrd((3*nm+1):(3*nm+3),1:3) = ibddthrs*[0 0 0;0 0 2;0 -2 0];
P_ztrdd((3*nm+1):(3*nm+3),1:3) = ibddthrs*eye(3);

%=====
%           Dynamics (Delta) Matrices
%=====

%initialize matrices
D_zdd = zeros(3*(k+1));
D_zd = zeros(3*(k+1));
D_z = zeros(3*(k+1));

%   DEFINE TORSIONAL MODE DYNAMICS
for k = 1:nm,

% mass terms
D_zdd((3*k-2):(3*k),(3*k-2):(3*k)) = itks(k)*eye(3,3);
D_zdd((3*k-2):(3*k),(3*nm+1):(3*nm+3)) = -ibddtks(k)*eye(3);
D_zdd((3*nm+1):(3*nm+3),(3*k-2):(3*k)) = -ibddtks(k)*eye(3);

% damping terms
D_zd((3*k-2):(3*k),(3*k-2):(3*k)) = ...

```

```

itks(k)*[0 0 0;0 0 2;0 -2 0];
D_zd((3*k-2):(3*k),(3*nm+1):(3*nm+3)) = ...
ibddtks(k)*[0 0 0;0 0 -2;0 2 0];
D_zd((3*nm+1):(3*nm+3),(3*k-2):(3*k)) = ...
ibddtks(k)*[0 0 0;0 0 -2;0 2 0];

% stiffness terms

D_z((3*k-2):(3*k),(3*k-2):(3*k)) = ...
itks(k)*[(wk(k)^2+1) 0 0;
0 (wk(k)^2) 0;
0 0 (wk(k)^2)];
D_z((3*k-2):(3*k),(3*nm+1):(3*nm+3)) = ...
[-ibtks(k) 0 0;
0 -ibtks(k)+ibddtks(k) 0;
0 0 -ibtks(k)+ibddtks(k)];
D_z((3*nm+1):(3*nm+3),(3*k-2):(3*k)) = ...
[-ibtks(k) 0 0;
0 -ibtks(k)+ibddtks(k) 0;
0 0 -ibtks(k)+ibddtks(k)];

end

% DEFINE RIGID FLAPPING DYNAMICS

% mass terms
D_zdd((3*nm+1):(3*nm+3),(3*nm+1):(3*nm+3)) = ibets*eye(3,3);

%damping terms
D_zd((3*nm+1):(3*nm+3),(3*nm+1):(3*nm+3)) = ...
flapflag*ibets*[0 0 0;0 0 2;0 -2 0];

```

```

%stiffness terms

D_z((3*nm+1):(3*nm+3),(3*nm+1):(3*nm+3)) = ...
    flapflag*ibets*[nubeta^2 0 0;0 (nubeta^2-1) 0;0 0 (nubeta^2-1)];

% ADD DELTA3 TERMS

D_zdd(:,(3*nm+1):(3*nm+3)) = D_zdd(:,(3*nm+1):(3*nm+3)) ...
    + d3flag*Kp*P_ztrdd;
D_zd(:,(3*nm+1):(3*nm+3)) = D_zd(:,(3*nm+1):(3*nm+3)) ...
    + d3flag*Kp*P_ztrd;
D_z(:,(3*nm+1):(3*nm+3)) = D_z(:,(3*nm+1):(3*nm+3)) ...
    + d3flag*Kp*P_ztr;

Di_zdd = inv(D_zdd);

%=====
%          Aerodynamic Forcing (Lambda) Matrices
%=====

%initialize matrices

L_z = zeros(3*(k+1));
L_zd = zeros(3*(k+1));

% DEFINE TORSIONAL MODE FORCING

for k= 1:nm,
    L_z((3*k-2):3*k,(3*k-2):3*k) = ...
        dampflag*gamma*[0 (mu*cbars*H0(k)/32) 0;
                        0 0 (-cbars*H1(k)/16);
                        0 (cbars*H1(k)/16) 0];
    L_z((3*nm+1):(3*nm+3),(3*k-2):(3*k)) = ...
        gamma*[(.25*mus*M0(k)+.5*M2(k)) 0 (.5*mu*M1(k));

```

```

    0 (.125*mus*M0(k)+.5*M2(k)) 0;
    (mu*M1(k)) 0 (.375*mus*M0(k)+.5*M2(k))];

L_zd((3*k-2):3*k,(3*k-2):3*k) = ...
dampflag*gamma*[-(cbars*H1(k)/16) 0 (-mu*cbars*H0(k)/32);
    0 (-cbars*H1(k)/16) 0;
    (-mu*cbars*H0(k)/16) 0 (-cbars*H1(k)/16)];

L_ztr((3*k-2):3*k,1:3) = zeros(3);
L_zl((3*k-2):3*k,1:3) = zeros(3);
L_ze((3*k-2):3*k,1:3) = ...
gamma*pbar*cbar*[(.25*mus*C0(k)+.5*C2(k)) 0 (.5*mu*C1(k));
    0 (.125*mus*C0(k)+.5*C2(k)) 0;
    (mu*C1(k)) 0 (.375*mus*C0(k)+.5*C2(k))];


```

end

```
% add delta3 in terms of tr (rigid pitch) matrices
% L_z = L_z + Kp*L_ztr check
```

% DEFINE RIGID FLAPPING FORCING

```
% L_btr = DUE TO RIGID PITCH
L_ztr((3*nm+1):(3*nm+3),1:3)= ...
flapflag*gamma*[(.25*mus*J0+.5*J2) 0 (.5*mu*J1);
    0 (.125*mus*J0+.5*J2) 0;
    (mu*J1) 0 (.375*mus*J0+.5*J2)];
```

% L_b = DUE TO FLAP ANGLE

```
L_z((3*nm+1):(3*nm+3),(3*nm+1):(3*nm+3))= ...
flapflag*gamma*[0 (.25*mu*K0-.25*mu*L1) 0;
    (-.5*mu*L1) 0 (-.5*K1-.125*mus*L0);
    0 (.5*K1-.125*mus*L0) 0] ...
```

```

- d3flag*Kp*L_ztr((3*nm+1):(3*nm+3),1:3);

% L_bd = DUE TO FLAP VELOCITY
L_zd((3*nm+1):(3*nm+3),(3*nm+1):(3*nm+3)) = ...
    flapflag*gamma*[(-.5*K1) 0 (-.25*mu*K0);
                    0 (-.5*K1) 0;
                    (-.5*mu*K0) 0 (-.5*K1)];

% L_b1 = DUE TO INFLOW
L_zl((3*nm+1):(3*nm+3),1:3) = ...
    inflag*flapflag*gamma*[(-.5*J1) 0 (-.25*mu*J1);
                           0 (-.5*J2) 0;
                           (-.5*mu*J0) 0 (-.5*J2)];

% L_be = DUE TO SERVO-FLAP DEFLECTION
L_ze((3*nm+1):(3*nm+3),1:3) = ...
    flapflag*gamma*nbar*[(.25*mus*B0+.5*B2) 0 (.5*mu*B1);
                           0 (.125*mus*B0+.5*B2) 0;
                           (mu*B1) 0 (.375*mus*B0+.5*B2)];

% ===== Pitt and Peters Inflow Matrices =====
vpeters = mus+(lamf+lami)*(lamf+2*lami)/sqrt(mus+(lamf+lami)^2);
if(alphad == 90)
    L = [(.5/vpeters) 0 0;0 (-2/vpeters) 0;0 0 (2/vpeters)];
else
    L = ...
(1/vpeters)*[.5 ((15*pi/64)*sqrt((1-sin(alpha))/(1+sin(alpha)))) 0;
              ((15*pi/64)*sqrt((1-sin(alpha))/(1+sin(alpha))))...
              ((-4*sin(alpha))/(1+sin(alpha))) 0;

```

```

0 0 (4/(1+sin(alpha)))];

end

Linv = inv(L);

M = [(128/(75*pi)) 0 0; 0 (-16/(45*pi)) 0; 0 0 (16/(45*pi))];

Minv = inflag*inv(M);

%=====
%      Hub Reaction (Gamma & Phi) Matrices
%=====

% Inertial Terms

for k = 1:nm,
    Ph_z(1:3,(3*k-2):3*k) = ...
        sigma*a*[0 0 0;
                   0 (.5*ebar*Mtks(k)/gamma) 0;
                   0 0 -.5*ebar*Mtks(k)/gamma];
    Ph_zd(1:3,(3*k-2):3*k) = sigma*a*[ 0 0 0;
                                              0 0 -ebar*Mtks(k)/gamma;
                                              0 -ebar*Mtks(k)/gamma 0];
    Ph_zdd(1:3,(3*k-2):3*k) = sigma*a*[ Mtks(k)/gamma 0 0;
                                              0 -.5*ebar*Mtks(k)/gamma 0;
                                              0 0 .5*ebar*Mtks(k)/gamma];

% Aerodynamic Matrices (minus inertial terms)

G_z(1:3,(3*k-2):3*k) = ...
    sigma*a*[(.25*mus*G0(k)+.5*G2(k)) 0 (.5*mu*G1(k));
               0 (-.0625*ebar*mus*G0(k)-.25*ebar*G2(k)) 0;
               (.5*ebar*mu*G1(k)) 0 ...;
               (.1875*ebar*mus*G0(k)+.25*ebar*G2(k))];

```

```

G_zd(1:3,(3*k-2):3*k) = zeros(3,3);

end

Ph_tr = sigma*a*[0 0 0;
                   0 (.5*ebar*Mtrs/gamma) 0;
                   0 0 (-.5*ebar*Mtrs/gamma)];

Ph_trd = sigma*a*[ 0 0 0;
                     0 0 -ebar*Mtrs/gamma;
                     0 -ebar*Mtrs/gamma 0];

Ph_trdd = sigma*a*[ Mtrs/gamma 0 0;
                      0 -.5*ebar*Mtrs/gamma 0;
                      0 0 .5*ebar*Mtrs/gamma];

% Aerodynamic Matrices (minus inertial terms)

G_tr = sigma*a*[(.25*mus*D0+.5*D2) 0 (.5*mu*D1);
                  0 (-.0625*ebar*mus*D0-.25*ebar*D2) 0;
                  (.5*ebar*mu*D1) 0 (.1875*ebar*mus*D0+.25*ebar*D2)];

G_trd = zeros(3,3);

% Inertial terms
% add delta3 terms
% Ph_b =
Ph_z(1:3,(3*nm+1):(3*nm+3)) = ...
flapflag*sigma*a*[0 0 0;

```

```

0 (-wbeta^2*ibets/(2*gamma)-.5*ebar*Mbs/(gamma)) 0;
0 0 (wbeta^2*ibets/(2*gamma)+.5*ebar*Mbs/(gamma))] ...
- d3flag*Kp*Ph_tr;

%Ph_bd =
Ph_zd(1:3,(3*nm+1):(3*nm+3)) = ...
flapflag*sigma*a*[0 0 0;
0 0 (ebar*Mbs/(gamma));
0 (ebar*Mbs/(gamma)) 0] ...
- d3flag*Kp*Ph_trd;

% Ph_bdd =
Ph_zdd(1:3,(3*nm+1):(3*nm+3)) = ...
flapflag*sigma*a*[(-Mbs/(gamma)) 0 0;
0 (.5*ebar*Mbs/(gamma)) 0;
0 0 (-.5*ebar*Mbs/(gamma))] ...
- d3flag*Kp*Ph_trdd;

% Aerodynamic Matrices (minus inertial terms)
% G_b =
G_z(1:3,(3*nm+1):(3*nm+3)) = ...
flapflag*sigma*a*[0 (.25*mu*E0-.25*mu*F1) 0;
(.25*ebar*mu*F1) 0 ...
(.25*ebar*E1+.0625*ebar*mus*F0);
0 (.25*ebar*E1-.0625*ebar*mus*F0) 0] ...
- d3flag*Kp*G_tr;

%Ga_bd =
G_zd(1:3,(3*nm+1):(3*nm+3)) = ...

```

```

flapflag*sigma*a*[(-.5*E1) 0 (-.125*mu*E0);
                    0 (.25*ebar*E1) 0;
                    (-.25*ebar*mu*E0) 0 (-.25*ebar*E1)] ...
- d3flag*Kp*G_trd;

G_1 = inflag*sigma*a*[(-.5*D1) 0 (-.25*mu*D1);
                      0 (.25*ebar*D2) 0;
                      (-.25*ebar*mu*D0) 0 (-.25*ebar*D2)]; 

G_e = sigma*a*nbar*[(.25*mus*A0+.5*A2) 0 (.5*mu*A1);
                     0 (-.0625*ebar*mus*A0-.25*ebar*A2) 0;
                     (.5*ebar*mu*A1) 0 (.1875*ebar*mus*A0+.25*ebar*A2)];

```

```

%=====
% newstate.m      define rotor state space
%=====

% j. garcia 4/8/93

% define new state space with new notation
% generalize for nm torsional modes 4/16/93
%=====

A = [zeros(3) eye(3) zeros(3,(3*nm+3)) zeros(3,(3*nm+3)) ...
      zeros(3);
      zeros(3) zeros(3) zeros(3,(3*nm+3)) zeros(3,(3*nm+3)) ...
      zeros(3);
      zeros((3*nm+3),3) zeros((3*nm+3),3) zeros((3*nm+3)) ...
      eye((3*nm+3)) zeros((3*nm+3),3);
      Di_zdd*(P_ztr + L_ztr)...;
      Di_zdd*P_ztrd...
      Di_zdd*(L_z-D_z)...;
      Di_zdd*(L_zd-D_zd)...;
      Di_zdd*L_zl;
      zeros(3) zeros(3) zeros(3,(3*nm+3)) zeros(3,(3*nm+3)) ...
      -Minv*Linv];

B = [zeros(3) zeros(3);
      eye(3) zeros(3);
      zeros((3*nm+3),3) zeros((3*nm+3),3);
      Di_zdd*P_ztrdd Di_zdd*L_ze;
      zeros(3) zeros(3)];

C = [(G_tr+Ph_tr) (G_trd+Ph_trd) (G_z+Ph_z) (G_zd+Ph_zd) G_l] + ...
      Ph_zdd*[Di_zdd*(P_ztr +L_ztr), ...

```

```

Di_zdd*P_ztrd, ...
Di_zdd*(L_z-D_z), ...
Di_zdd*(L_zd-D_zd), ...
Di_zdd*L_zl];

D = [Ph_trdd G_e ] + ...
     Ph_zdd*[Di_zdd*P_ztrdd Di_zdd*L_ze];

% Modified Aerodynamic Matrices (minus inertial terms)
B1 = [zeros(3); ...
       zeros(3); ...
       zeros((3*nm+3),3); ...
       zeros((3*nm+3),3); ...
       Minv];
Ca = [G_tr G_trd G_z G_zd G_l];
Da = [zeros(3) G_e];

% Convert radians to degrees
rpd = pi/180;
dpr = 180/pi;

Ar2d = ones(6*nm+15,6*nm+15);
Br2d = ones(6*nm+15,6);
Blr2d = ones(6*nm+15,3);
Cr2d = ones(3,6*nm+15);
Dr2d = ones(3,6);

Ar2d(1:(6*nm+12),(6*nm+13):(6*nm+15)) = dpr*ones((6*nm+12),3);
Ar2d((6*nm+13):(6*nm+15),1:(6*nm+12)) = rpd*ones(3,(6*nm+12));

```

```

Br2d((6*nm+13):(6*nm+15),1:6) = rpd*ones(3,6);

Cr2d(1:3,1:(6*nm+12)) = rpd*ones(3,(6*nm+12));

Dr2d(1:3,1:6) = rpd*ones(3,6);

A = Ar2d.*A;
B = Br2d.*B;
C = Cr2d.*C;
D = Dr2d.*D;
Ca = Cr2d.*Ca;
Da = Dr2d.*Da;

%=====
% Include Options
% By zeroing out unwanted dynamics
%=====

% No Flapping
if(flapflag == 0);
    A(1:(6*nm+15),(3*nm+7):(3*nm+9)) = zeros((6*nm+15),3);
    A((3*nm+7):(3*nm+9),1:(6*nm+15)) = zeros(3,(6*nm+15));
    A(1:(6*nm+15),(6*nm+10):(6*nm+12)) = zeros((6*nm+15),3);
    A((6*nm+10):(6*nm+12),1:(6*nm+15)) = zeros(3,(6*nm+15));
    B((3*nm+7):(3*nm+9),1:9) = zeros(3,9);
    B((6*nm+10):(6*nm+12),1:9) = zeros(3,9);
    C(1:3,(3*nm+7):(3*nm+9)) = zeros(3,3);
    C(1:3,(6*nm+10):(6*nm+12)) = zeros(3,3);
end;

```

```
%=====
```

```

% No Mode1

if(mode1flag == 0);

A(1:27,7:9) = zeros(27,3);
A(7:9,1:27) = zeros(3,27);
A(1:27,16:18) = zeros(27,3);
A(16:18,1:27) = zeros(3,27);
B(7:9,1:9) = zeros(3,9);
B(16:18,1:9) = zeros(3,9);
C(1:3,7:9) = zeros(3,3);
C(1:3,16:18) = zeros(3,3);

end;

%=====
% No Mode2

if(mode2flag == 0);

A(1:27,10:12) = zeros(27,3);
A(10:12,1:27) = zeros(3,27);
A(1:27,19:21) = zeros(27,3);
A(19:21,1:27) = zeros(3,27);
B(10:12,1:9) = zeros(3,9);
B(19:21,1:9) = zeros(3,9);
C(1:3,10:12) = zeros(3,3);
C(1:3,19:21) = zeros(3,3);

end;

%=====
% No Inflow

if(inflag == 0);

A(1:(6*nm+15),(6*nm+13):(6*nm+15)) = zeros((6*nm+15),3);
A((6*nm+13):(6*nm+15),1:(6*nm+15)) = zeros(3,(6*nm+15));

```

```
B((6*nm+13):(6*nm+15),1:9) = zeros(3,9);  
C(1:3,(6*nm+13):(6*nm+15)) = zeros(3,3);  
else  
%=====  
% Close aerodynamic loop  
%=====  
A = A+B1*Ca;  
B = B + B1*Da;  
  
end  
%=====
```


References

- [1] J. Abramson and E.O. Rogers, "Optimization Theory Applied to Higher Harmonic Control of Circulation Controlled Rotors," *37th Annual Forum*, American Helicopter Society, New Orleans, LA, 1981.
- [2] Anonymous, "X-wing Full Scale Wind Tunnel Test Final Report," Lockheed Report SP-5190, October 1980.
- [3] J.C. Balcerak and J.C. Erickson, Jr., "Suppression of Transmitted Harmonic Vertical and In-plane Rotor Loads by Blade Pitch Control," U.S. Army Aviation Materiel Laboratories Technical Report 69-39, July 1969.
- [4] R. Barrett, "Intelligent Rotor Blade Actuation through Directionally Attached Piezoelectric Crystals," *46th Annual Forum*, American Helicopter Society, Washington, D.C., 1990.
- [5] R.L. Bielawa, "Analytical Investigation of Helicopter Rotor Blade Appended Aeroelastic Devices," NASA CR 166525, February 1984.
- [6] R.L. Blisplinghoff, H. Ashley, and R.L. Halfman, *Aeroelasticity*, Addison-Wesley, Cambridge, MA, 1955.
- [7] P.J. Carpenter and S. Paulnock, "Hovering and Low-Speed Performance and Control Characteristics of an Aerodynamic-Servocontrolled Helicopter Rotor System as Determined on the Langley Helicopter Tower," NACA TN-2086, May 1950.

- [8] E.F. Crawley and K.B. Lazarus, "Induced Strain Actuation of Isotropic and Anisotropic Plates," *30th Structures, Structural Dynamics and Materials Conference*, Mobile, AL, April 1989.
- [9] M. Drela, "XFOIL: An Analysis and Design System for Low Reynolds Number Airfoils," *Low Reynolds Number Aerodynamics*. Springer-Verlag Lecture Notes in Engineering, No. 54, 1989.
- [10] R.W. DuVal, C.Z. Gregory, and N.K. Gupta, "Design and Evaluation of a State-Feedback Vibration Controller," *Journal of the American Helicopter Society*, Vol. 29, No. 3, July 1984, pp. 30-37.
- [11] D.G. Ekquist, "Design and Wind Tunnel Test of a Model Helicopter Rotor Having an Independently Movable Inboard Blade Panel," U.S. Army Aviation Materiel Laboratories Technical Report 65-63, October 1965.
- [12] M.E. Fox, "Blade-Mounted Actuation for Helicopter Rotor Control," Master's thesis, Massachusetts Institute of Technology, Department of Aeronautics and Astronautics, Cambridge, MA, June 1993.
- [13] Glauert, H., "Theoretical Relationships for an Aerofoil with Hinged Flap," *Aeronautical Research Council Reports and Memoranda* 1095, April 1927.
- [14] N.K. Gupta and R.W. DuVal. "A New Approach for Active Control of Rotorcraft Vibration," *Journal of Guidance and Control*, Vol. 5, No. 2, April 1982, pp. 143-150.
- [15] S.R. Hall and N.M. Wereley, "Performance of Higher Harmonic Control Algorithms for Helicopter Vibration Reduction," *Journal of Guidance, Control, and Dynamics*, Vol. 16, No. 4, July-August 1993, pp. 793-797.
- [16] S.R. Hall, K.Y. Yang, and K.C. Hall, "Helicopter Rotor Lift Distributions for Minimum Induced Power Loss," *AHS International Technical Specialists' Meeting on Rotorcraft MultiDisciplinary Design Optimization*, Atlanta, GA, April 1993.

- [17] N.D. Ham, "Helicopter Individual-Blade-Control Research at M.I.T. 1977–1985," *Vertica*, Vol. 11, No. 1/2, 1987, pp. 109–122.
- [18] W.E. Hooper, "The Vibratory Airloading of Helicopter Rotors," *Ninth European Rotorcraft and Powered Lift Aircraft Forum*, Stresa, Italy, 1983.
- [19] W. Johnson, *Helicopter Theory*, Princeton University Press, Princeton, NJ, 1980.
- [20] D.G. Kirkpatrick and D.R. Barnes, "Development and Evolution of the Circulation Control Rotor," *36th Annual Forum*, American Helicopter Society, 1980.
- [21] M. Kretz, "Research in Multicyclic and Active Control of Rotary Wings," *Vertica*, Vol. 1, No. 2, 1976, pp. 95–105.
- [22] K.B. Lazarus. *Multivariable High-Authority Control of Plate-like Active Lifting Surfaces*, Ph.D. thesis, Massachusetts Institute of Technology, Department of Aeronautics and Astronautics, Cambridge, MA, June 1992.
- [23] A.Z. Lemnios and F.K. Dunn, "Theoretical Study of a Multicyclic Control of a Controllable Twist Rotor," NASA CR-151959, October 1978.
- [24] A.Z. Lemnios, A.F. Smith, and W.E. Nettles, "The Controllable Twist Rotor, Performance and Blade Dynamics," *28th Annual Forum*, American Helicopter Society, 1975.
- [25] R.G. Loewy, "Airstream Actuated Rotor Control," Presentation for U.S. Army Research Office, Industry Consortium Site Visit, Rensselaer Polytechnic Institute, Troy, NY, September 1993.
- [26] J.L. McCloud III, "An Analytical Study of a Multicyclic Controllable Twist Rotor," *31th Annual Forum*, American Helicopter Society, 1975.
- [27] J.L. McCloud III, "The Promise of Multicyclic Control," *Vertica*, Vol. 4, No. 1, 1980, pp. 29–41.

- [28] J.L. McCloud III and M. Kretz, "Multicyclic Jet-Flap Control for Alleviation of Helicopter Blade Stresses and Fuselage Vibration," *AHS/NASA-Ames Specialists' Meeting on Rotorcraft Dynamics*, NASA SP-352, February 1974.
- [29] J.L. McCloud III and A.L. Weisbirch, "Wind-Tunnel Results of a Full-Scale Multicyclic Controllable Twist Rotor," *34th Annual Forum*, American Helicopter Society, 1978.
- [30] W. Miao, S.B.R. Kottapalli, and H.M. Frye, "Flight Demonstation of Higher Harmonic Control (HHC) on the S-76," *42nd Annual Forum*, American Helicopter Society, Washington D.C., 1986.
- [31] F. Nitzsche, "Modal Sensors and Actuators for Individual Blade Control," *33rd Structures, Structural Dynamics, and Materials Conference*, La Jolla, CA, April 1993.
- [32] F. Nitzsche and E.J. Breitbach, "A Study on the Feasability of Using Adaptive Structures in the Attenuation of the Vibration Characteristics of Rotary Wings", *32nd Structures, Structural Dynamics, and Materials Conference*, Dallas, TX, April 1992.
- [33] P.R. Payne, "Dynamics of a Rotor Controlled by Aerodynamic Servo Flaps," *Aircraft Engineering*, Vol. 31, No. 369, November 1959 , pp.330–339.
- [34] D.A. Peters, "Hingeless Rotor Frequency Response with Unsteady Inflow," *AHS/NASA-Ames Specialists' Meeting on Rotorcraft Dynamics*, NASA SP-352, February 1974.
- [35] D.M. Pitt and D.A. Peters, "Theoretical Prediction of Dynamic-Inflow Derivatives," *Vertica*, Vol. 5, No. 1, 1981, pp. 21–34.
- [36] R.A. Piziali and A.R. Trenka, "A Theoretical Study of the Application of Jet-Flap Circulation Control for Reduction of Vibratory Forces," NASA CR-137515, May 1974.

- [37] K.R. Reader and W.J. Jr. Dixon, "Evaluation of a Ten-Foot Diameter X-Wing Rotor," *40th Annual Forum*, American Helicopter Society, Arlington, VA, 1984.
- [38] D.W. Robinson, W.E. Nettles, and H.E. Howes, "Design Variables for a Controllable Twist Rotor," *31st Annual Forum*, American Helicopter Society, May 1975.
- [39] J. Shaw and N. Albion, "Active Control of Rotor Blade Pitch for Vibration Reduction: A Wind Tunnel Demonstration," *Vertica*, Vol. 4, No. 1, 1980, pp.3–11.
- [40] J. Shaw, N. Albion, E.J. Hanker, and R.S. Teal, "Higher Harmonic Control: Wind Tunnel Demonstration of Fully Effective Vibratory Hub Force Suppression," *41st Annual Forum*, American Helicopter Society, Fort Worth, TX, 1985.
- [41] R.L. Spangler, "Piezoelectric Actuators for Helicopter Rotor Control," Master's thesis, Massachusetts Institute of Technology, Department of Aeronautics and Astronautics, Cambridge, MA, June 1989.
- [42] R.L. Spangler and S.R. Hall, "Piezoelectric Actuators for Helicopter Rotor Control," Space Systems Laboratory Report SSL #1-89, Massachusetts Institute of Technology, Cambridge, MA, January 1989.
- [43] R.L. Spangler and S.R. Hall, "Piezoelectric Actuators for Helicopter Rotor Control," *31st Structures, Structural Dynamics and Materials Conference*, Long Beach, CA, April 1990.
- [44] H. Strehlow and H. Rapp, "Smart Materials for Helicopter Rotor Control," *AGARD/SMP Specialists Meeting on Smart Structures for Aircraft and Spacecraft*, Lindau, Germany, October 1992.
- [45] R.H. Stroub, L. Young, M. Cawthorne, and C. Keys, "Helicopter Rotor Blade with Free Tip," *NASA Tech Briefs*, Vol. 16, No. 8, August 1992, p. 62.

- [46] A. Weisbrich, R. Perley, and H. Howes, "Design Study of a Feedback Control System for the Multicyclic Flap System Rotor," NASA CR-151960, January 1977.
- [47] W.A. Welsh and R.H. Jr. Blackwell, "Higher Harmonic and Trim Control of the X-Wing Circulation Control Wind Tunnel Model Rotor," *45th Annual Forum*, American Helicopter Society, Boston, MA, 1989.
- [48] E.R. Wood and A.C. Buffalano, "Parametric Investigation and Aeroelastic Characteristics of Articulated and Hingeless Helicopter Rotor Systems," U.S. Army Transportation Research Command Technical Report 64-15, April 1964.
- [49] E.R. Wood, R.W. Powers, J.H. Cline, and C.E. Hammond, "On Developing and Flight Testing a Higher Harmonic Control System," *39th Annual Forum*, American Helicopter Society, St. Louis, MO, 1983.
- [50] D.K. Young and F.J. Tarzanin, "Structural Optimization and Mach Scale Test Validation of a Low Vibration Rotor," *47th Annual Forum*, American Helicopter Society, Phoenix, AZ, 1991.
- [51] D.K. Young, F.J. Tarzanin, and D.L. Kunz, "Use of Blade Sweep to Reduce 4/Rev Hub Loads," *43rd Annual Forum*, American Helicopter Society, St. Louis, MO, 1987.

20 (9 - 11)